Technische Universität München
Physik Department
Theoretische Physik T37

Interfacial Polymer and Water Dynamics

Christian Sendner

Vollständiger Abdruck der von der Fakultät für Physik der Technischen Universität München zur Erlangung des akademischen Grades eines

Doktors der Naturwissenschaften (Dr. rer. nat.)

genehmigten Dissertation.

Vorsitzender:		Univ.-Prof. Dr. G. Abstreiter
Prüfer der Dissertation:	1.	Univ.-Prof. Dr. R. Netz
	2.	Univ.-Prof. Dr. R. Metzler

Die Dissertation wurde am 13.11.2008 bei der Technischen Universität München eingereicht und durch die Fakultät für Physik am 02.12.2008 angenommen.

Die vorliegende Arbeit mit dem Titel *Interfacial Polymer and Water Dynamics* ist unter der Betreuung von Herrn Prof. Dr. Roland R. Netz am Lehrstuhl T37 im Physik-Department der Technischen Universität München entstanden.

Meinen besonderen Dank möchte ich Herrn Prof. Dr. Roland Netz für die wissenschaftliche Anleitung zu dieser Arbeit aussprechen. In zahlreichen Diskussionen leistete er fundamentale Beiträge für die vorliegende Dissertation und verstand es, mich stets aufs Neue zu motivieren. Auch gab er mir die Möglichkeit für einen Auslandsaufenthalt im sonnigen Santa Barbara und sorgte für die Organisation von Winterschulen, Sommerfesten und Weihnachtsfeiern, die mir stets in guter Erinnerung bleiben werden.

Bei Herrn Prof. Dr. Ralf Metzler bedanke ich mich herzlichst für seine Bereitschaft, diese Arbeit zu prüfen. Herrn Dr. Ulrich Rant sowie den Mitgliedern seiner Arbeitsgruppe bin ich sehr dankbar für die erfolgreiche Zusammenarbeit und für viele Diskussionen und Erklärungen auf dem Gebiet der Biosensorik. Herrn Prof. Dr. Yong Woon Kim möchte ich für wesentliche Vorarbeiten zur theoretischen Modellierung und für die Interpretation der Ergebnisse auf diesem Gebiet danken. Herrn Dr. Dominik Horinek bin ich äusserst dankbar für seine wertvolle Hilfe bei den Molekulardynamik Simulationen und für seine Korrekturen des Manuskripts, sowie Herrn Felix Sedlmeier für seine Unterstützung bei der Bestimmung der Kontaktwinkel. Bei Herrn Prof. Dr. Lyderic Bocquet und Herrn Dr. David Huang bedanke ich mich herzlichst für die erfolgreiche Zusammenarbeit sowie für die theoretischen Ergebnisse zur hydrodynamischen Randbedingung an hydrophoben Oberflächen. Herrn Dipl. Phys. Sebastian Fischer bin ich sehr dankbar für zahlreiche Diskussionen auf dem Gebiet der Hydrodynamik und Brownschen Bewegung von Polymeren sowie für seine Bereitschaft, Teile des Manuskripts Korrektur zu lesen. Vielen Dank an Frau Sonja Ortner, die als Sekretärin der Arbeitsgruppe immer hilfsbereit und freundlich bei sämtlichen Problemen zur Verfügung stand. Danke auch an alle aktuellen und ehemaligen Mitglieder des Lehrstuhles, die stets für ein äusserst angenehmes Arbeitsklima sorgten und jederzeit für wissenschaftliche Diskussionen zur Verfügung standen.

Dem Graduiertenkolleg CompInt des Elitenetzwerks Bayern und meinem Co-Advisor Prof. Dr. Gerhard Abstreiter möchte ich für die Unterstützung in meiner Arbeit sowie für zahlreiche interessante Seminare und Workshops danken. Für die materielle Unterstützung meiner Lehr- und Forschungsaufgaben im Rahmen des Schwerpunktprogrammes 1164 möchte ich der Deutschen Forschungsgemeinschaft meinen Dank aussprechen. Beim Leibnitz-Rechenzentrum bedanke ich mich für die zur Verfügung gestellte Rechenzeit sowie für den Support durch dessen Mitarbeiter.

Contents

1. Introduction and outline

Polymers are long, chain-like molecules, formed by the sequential addition of chemical subunits. Their technological applications are wide spread. Plastic materials consist of entangled synthetic polymers and are omnipresent in our daily life. The physical properties of polymers are also used in less obvious technological applications. For example, their ability to stabilize colloidal solutions [1] is used in the food and cosmetic industry for the production of emulsions. Polymers serve as lubricants or even as adhesives in the automotive industry [2]. Apart from their industrial importance, many biomolecules belong to the class of polymers. One of the most prominent example certainly is the DNA molecule, which carries the genetic information of life. The mechanical properties of biopolymers like actin or microtubules determine the stability of biological cells and even their motility [3]. The dynamics of polymeric liquids leads to surprising effects, experienced in every day's life: the viscoelastic property of starch solution makes it possible to walk on it whereas one starts sinking as soon as one stops to move. Also, nearly everybody has experienced the shear thinning property of ketchup. Under the influence of shear stress by shaking the bottle, the liquid flows more easily.

To explain all these effect, a profound understanding of the static and dynamic properties of polymers is indispensable. Due to the large number of internal degrees of freedom, methods from statistical mechanics are applied to describe polymer conformations from a theoretical point of view [4–6]. The non-equilibrium polymer dynamics is of prime importance. In most technological applications, polymers are subject to external fields or flows, for example from stirring or pumping a polymer solution. As in silicon technology, miniaturization is a key concept for microfluidic devices with applications in biosensing or gene chips [7–9]. For these devices, surface effects are of increasing importance which makes a sound analysis of interfacial dynamics necessary.

The development of new experimental techniques in the last few decades shed new light on the dynamics of polymers. Classical techniques like light scattering or birefringence experiments [10–12] bear the disadvantage of averaging over a macroscopic number of molecules. Also the time resolution of such experiments is limited. Only recently, the observation of single molecule dynamics in external flow with a high temporal resolution has become possible with fluorescence microscopy [13, 14]. Some snapshots of the configurations of a single DNA molecule in steady shear flow are shown in Fig. 1.1. These observations can be directly compared to theoretical and numerical results. Despite the tremendous increase in computer power over the last years, all-atomistic simulations are still limited to short polymer chains. Therefore, coarse-grained methods, which describe the solvent molecules on a continuum level are widely used [15–17].

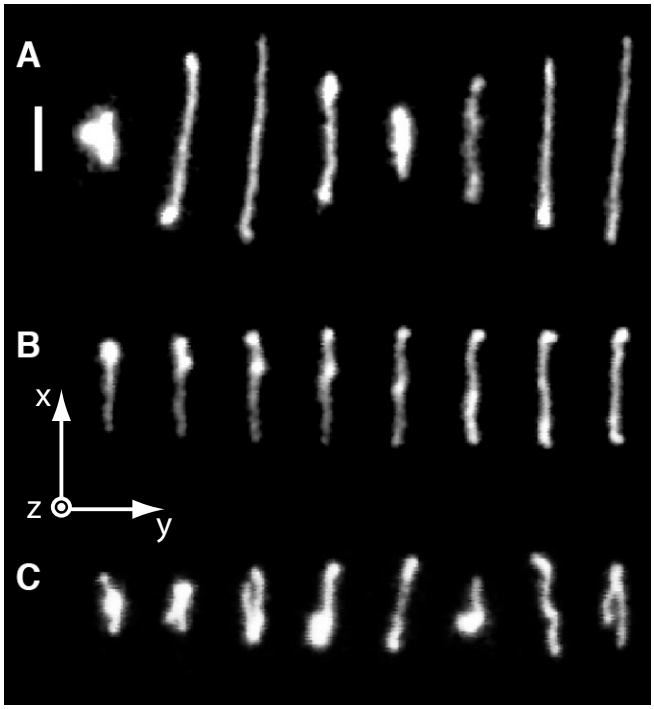

Figure 1.1.: Fluorescence microscopy pictures of a 22 μm long lambda bacteriophage DNA (λ-DNA) in steady shear flow $\mathbf{v}(z) = \dot{\gamma} z \hat{e}_x$ of viscous sugar solution [13]. The single pictures from left to right are time series of the polymer trajectory with time intervals of 6 s (A, C) and 0.84 s (B) between the images. The upper left vertical bar indicates 5 μm. Polymers in shear are repeatedly stretched and recoiled by the flow. Thus, large shape fluctuations are observed for the polymers. Repeatedly coil-stretch transitions (A) or folded and kinked polymer configurations (C) are observed. The timescale of the polymer motion is determined by its longest relaxation time τ. The Weissenberg number $Wi = \dot{\gamma}\tau$ is a measure of the flow strength relative to the polymer relaxation dynamics. Polymers are found to be distorted by the flow at $Wi \gtrsim 1$. The shear rate $\dot{\gamma} = 1\ \mathrm{s}^{-1}$, at which the above pictures are recorded, corresponds to a Weissenberg number of $Wi = 19$ for this kind of DNA.

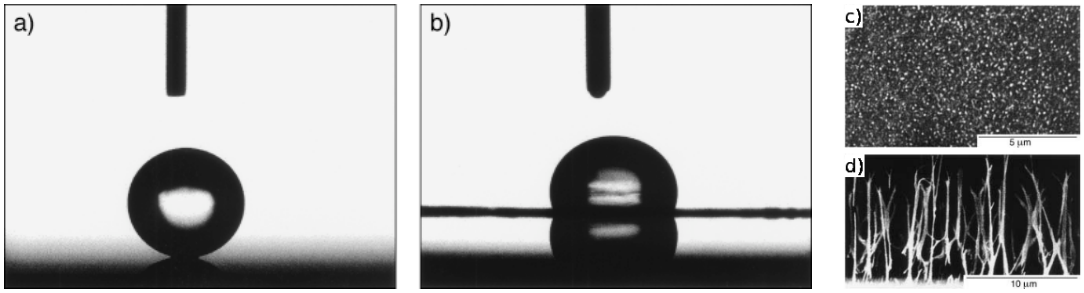

Figure 1.2.: Water droplets on a rough, superhydrophobic (a) and smooth hydrophobic surface (b). Fig. (c) shows a top view and (d) the cross section of the superhydrophobic surface [18]. The rough surface is constructed out of aligned polyacrylonitrile (PAN) nanofibers. Their tip diameter is roughly 100 nm with an average distance of 500 nm. The liquid stays on top of the fibers with air in between the fibers (Cassie state). This leads to a very high contact angle of 174°, Fig. (a). On the smooth surface where the nanofibers are not aligned parallel to the surface normal, the contact angle is 101°, significantly smaller compared to the rough surface.

Although these coarse graining techniques deliver valuable insights into the dynamics of polymers, they are limited due to the neglect of the microscopic solvent structure. Continuum theories are not able to capture effects arising from the discrete nature of the solvent constituents. Since most biological and technological processes take place in aqueous solution, water is one of the most important solvents. By itself, water has remarkable properties such as its potency as a solvent or its crystallization behavior. Water molecules are built out of two hydrogen and one oxygen atoms. Due to the high electronegativity of the oxygen atom, the water molecules are polar with the negative partial charge located on the position of the oxygen. The interaction between water molecules is governed by the formation of strong hydrogen bonds between single molecules. At room temperature, water molecules are in constant thermal motion which leads to a lifetime of a single H-bond in the picosecond range [19]. This hydrogen bonding network is destroyed at a free surface and therefore leads to a strong decrease in internal energy. This results in the high surface tension of liquid water which is only exceeded by liquid mercury [20].

The structural changes of water at liquid/solid interfaces are of particular interest. Surfaces can be classified according to the contact angle, the angle which is formed by a liquid droplet on the surface. This angle ranges from zero degrees at very hydrophilic surfaces which show complete wetting, to almost 180° on structured hydrophobic, so called superhydrophobic surfaces [21], see Fig. 1.2. The self-cleaning property of these surfaces, also known as the *Lotus effect* bears potential for various technological applications. On the other hand, droplet formation is inhibited on hydrophilic surfaces, which can be used for anti fogging coatings [22]. These hydrophobic and hydrophilic effects have also implications on the dynamics of biological systems, since life normally takes place in aqueous solution. For example, protein folding dynamics is influenced by those hydrophobic interactions [23].

In hydrodynamic theory, the no-slip boundary for flow at surfaces is widely used. This means that the relative fluid velocity at the liquid/solid interface is zero. From atomistic simulations as well as from experiments, it turns out, that this assumption is not valid in general [24]. The amount of slippage and its dependence on surface parameters is still under debate and has to be examined in more detailed. For microfluidic applications, the boundary condition for fluid flow on the nanoscale is important due to the increasing hydrodynamic resistance for small channel dimensions. In biology, boundary effects become crucial for the transport through biological membrane channels [25].

Due to the complexity of the water structure and the long ranged electrostatic interactions between single water molecules, analytical approaches are not able to fully explain the water properties. All-atomistic simulations can shed light on the dynamic and equilibrium water properties.

Outline of the Thesis

This thesis is divided in two parts, referring to the level of coarse-graining in the modeling of the considered systems. In the first part, non-equilibrium polymer dynamics is described within the framework of Brownian Dynamics. In this method, the effect of the solvent molecules is taken into account in an effective way, leading to stochastic forces on the polymer. This approach allows the simulation of sufficiently long trajectories for a statistical analysis. The general framework of Brownian Dynamics with included hydrodynamic interactions is explained in chapter 2. In chapter 3 we repeat classical simulations of coarse-grained DNA molecules in shear [17, 26] and find a novel regime where the chain diameter depends on the shear strength in a non-monotonic fashion. Experimentally, this regime is easily reachable with natural DNA at elevated shear strengths. After this, surface effects for non equilibrium polymer dynamics are discussed. The coupling of hydrodynamic interactions and thermal fluctuations leads to a repulsion of polymers from interfaces in external fields as well as in shear flow. On the basis of a Fokker-Planck analysis, orientation distribution functions for the polymers are calculated to quantify the strength of this repulsion. Scaling laws are derived analytically, which are favorably compared with extensive simulations. In the last chapter of the first part, the electrical manipulation of end grafted DNA molecules and their possible use for biosensing purposes are discussed. It is shown that the different bending stiffness of single and double stranded DNA as well as the adsorption of ligands lead to measurable effects on the DNA dynamics, which explains experiments on the electrical switching of end attached DNA [27, 28].

Whereas in the first part, the effect of the solvent molecules is incorporated within a continuum description, the second part of the thesis analyzes the structure of interfacial water on an atomistic level. Firstly, Molecular Dynamics (MD) simulation techniques are shortly explained and the equilibrium structure of water at different hydrophobic surfaces are analyzed in detail. From the microscopic simulations, macroscopic, experimentally measurable quantities like contact angles are determined. In the following chapter, we use non-equilibrium Molecular Dynamics (NEMD) simula-

tions to examine the hydrodynamic boundary condition at hydrophobic surfaces. This boundary condition can be characterized by the so called slip length, which quantifies the velocity difference between the solid and the fluid phase at the interface. We find a quasi universal relationship between this slip length and the contact angle. We also checked for the effect of dissolved gas on interfacial properties, as dissolved gas and surface-adsorbed nano-bubbles are often involved in explanations of strange surface effects such as giant-slip or large hydrophobic attraction [29–32]. However, we find only mild effects of surface-adsorbed gas on the slip length.

In chapter 9, the preceding examinations are extended to polar, hydrophilic surfaces. Especially, we focus on the shear viscosity in the interfacial layer and on the diffusive properties for water molecules close to the surface, obtained from NEMD. We do not find evidence for a layer of frozen water or for an increase in the interfacial viscosity of several orders of magnitude at hydrophilic surfaces, as was often reported in the literature [33–37].

The next logical step would be to simulate polymeric molecules using atomistic simulations and to check for effects that in principle can not be obtained with coarse-grained simulations. Some preliminary results of the non-equilibrium adsorption of carbon nanotubes on hydrophobic surfaces are presented in the outlook section. This is an open field for future investigations.

Part I.

Coarse-grained dynamics of polymers at interfaces

2. Coarse-grained polymer dynamics

The first part of this thesis discusses polymer dynamics with focus on hydrodynamic effects for polymer motion close to interfaces. This section introduces the theoretical concepts, namely Brownian Dynamics methods, used for the analysis. Polymers in solution randomly change their shape and position due to the thermal motion of the surrounding solvent particles. Since an explicit description of all solvent degrees of freedom is computationally very demanding, they are implemented in a coarse-grained fashion via a diffusion equation. The so called Smoluchowski or Fokker-Planck equation describes the motion of the solute by the time evolution of its probability distribution. The basic assumptions for this method are that the time and length scales for the polymer motion are much larger than those of the solvent molecules and that a linear relation between fluxes and forces holds. These assumptions are fulfilled for most polymer solutions. Subsequently, a short derivation of the Smoluchowski equation will be given.

Let $\Psi(\{x\},t)$ be the N dimensional density probability distribution of the spatial coordinates $\{x\} = x_1, ..., x_N$. From Fick's law, the probability current is given by the gradient of the probability distribution times a diffusion tensor $\mathbf{D}$ and by the deterministic velocities v_n,

$$j_n(\{x\},t) = -\sum_m D_{nm}\partial_m \Psi(\{x\},t) + v_n \Psi(\{x\},t) \tag{2.1}$$

where ∂_m is the short-hand notation for $\partial/\partial x_m$. The motion of a Brownian particle will drag the surrounding fluid along with it, which leads to a coupling between different particles. This coupling is implemented by a tensorial mobility, which in general depends on the configuration of all Brownian particles. Then, the deterministic velocities are given by the force on the particle, stemming from the potential energy U, times the mobility matrix μ_{mn},

$$v_n = \sum_m \mu_{nm} \left[-\partial_m U(\{x\})\right]. \tag{2.2}$$

The calculation of the mobility matrix will be explained in the following section 2.1. In equilibrium, the distribution function for a canonical ensemble with temperature T is given by the Boltzmann distribution, $\Psi(\{x\}) \propto \exp(-U/k_\mathrm{B}T)$. Since in equilibrium, the probability current vanishes, the diffusion constant reads $D_{nm}/k_\mathrm{B}T = \mu_{mn}$. With the continuity equation, div $\mathbf{j} = -\dot{\Psi}$, the time derivative of the probability distribution is given by the Smoluchowski or Fokker-Planck equation,

$$\dot{\Psi}(\{x\},t) = \sum_{n,m} \partial_n \mu_{nm} \left\{\left[\partial_m U(\{x\})\right] \Psi(\{x\},t) + k_\mathrm{B}T \left[\partial_m \Psi(\{x\},t)\right]\right\}. \tag{2.3}$$

The next two sections are concerned with the calculation of the mobility matrix and the implementation of the above equation in computer simulations.

2.1. Hydrodynamic interactions

For the investigated length scales in this study, the low Reynolds number regime applies [38]. This means that the system is over-damped and inertial effects are negligible. The Reynolds number for fluid density ρ, viscosity η, typical velocity v and length scale L,

$$Re = \frac{\rho v L}{\eta} \tag{2.4}$$

is the ratio between inertial and viscous effects. For the time and length scales in polymer dynamics, the Reynolds number is normally much smaller than unity. For example, consider a micrometer sized object, $L \sim 1$ μm, moving with a velocity of $v \sim 1$ μm/s in water, characterized by $\rho \sim 10^3$ kg/m^3 and $\eta \sim 10^{-3}$ Pas. Then, the Reynolds number is $Re \sim 10^{-6}$, thus much smaller than unity. Therefore, neglecting the inertia term in the Navier Stokes equation is a good approximation. With these approximations, the equations of motion for an incompressible fluid are given by the stationary Stokes equations

$$\nabla p(\mathbf{r}) - \eta \nabla^2 \mathbf{v}(\mathbf{r}) = \mathbf{f}(\mathbf{r}) \tag{2.5}$$

$$\nabla \cdot \mathbf{v}(\mathbf{r}) = 0 \tag{2.6}$$

for the fluid velocity field $\mathbf{v}(\mathbf{r})$ with pressure $p(\mathbf{r})$ and force density $\mathbf{f}(\mathbf{r})$.

For point-forces, so called Stokeslets, at positions $\mathbf{r}_j$, eqs. (2.5) and (2.6) can be solved by the appropriate Greensfunction $\mathbf{G}(\mathbf{r}, \mathbf{r}_j)$. Due to the linearity of the Stokes equation, the fluid field at position $\mathbf{r}$ is given by the superposition of the single solutions,

$$\mathbf{v}(\mathbf{r}) = \sum_j \mathbf{G}(\mathbf{r}, \mathbf{r}_j)\mathbf{f}(\mathbf{r}_j). \tag{2.7}$$

For bulk flow, i.e. $\mathbf{v}(|\mathbf{r} - \mathbf{r}_j| \to \infty) = \mathbf{0}$, the Greens function $\mathbf{G}$ of the Stokes equation is given by the Oseen tensor

$$G^0_{\alpha\beta}(\mathbf{r}_i, \mathbf{r}_j) \equiv G^0_{\alpha\beta}(\mathbf{r}) = \frac{1}{8\pi\eta r}\left(\delta_{\alpha\beta} + \frac{r_\alpha r_\beta}{r^2}\right) \tag{2.8}$$

with Cartesian components α, β and relative coordinate $\mathbf{r} \equiv \mathbf{r}_i - \mathbf{r}_j$. The hydrodynamic interactions are long ranged and decay linearly with the inverse distance $\sim 1/r$.

The Greens function $\mathbf{G}$ for fluid flow in the semi infinite space $z > 0$ with a no slip boundary at $z = 0$, i.e. $\mathbf{v}(\mathbf{r})|_{z=0} = \mathbf{0}$, was first derived by Blake [39]. It is constructed by a set of appropriate image sources at positions $\mathbf{R} = \mathbf{r}_i - \mathbf{r}'_j = (x_i - x_j, y_i - y_j, z_i + z_j)$ and reads

$$\mathbf{G}^W(\mathbf{r}_i, \mathbf{r}_j) = \mathbf{G}^0(\mathbf{r}) - \mathbf{G}^0(\mathbf{R}) + \mathbf{G}^D(\mathbf{R}) - \mathbf{G}^{SD}(\mathbf{R}). \tag{2.9}$$

The wall Greens function $\mathbf{G}^W$ contains the bulk Oseen tensor $\mathbf{G}^0$ from eq. (2.8), the Stokes doublet

$$G^D_{\alpha\beta}(\mathbf{r}) = \frac{1}{8\pi\eta} 2z_j^2(1-2\delta_{\beta z})\frac{\partial}{\partial r_\beta}\left(\frac{r_\alpha}{r^3}\right) \tag{2.10}$$

and the source doublet,

$$G^{SD}_{\alpha\beta}(\mathbf{r}) = 2z_j(1-2\delta_{\beta z})\frac{\partial}{\partial r_\beta} G^0_{\alpha z}(\mathbf{r}). \tag{2.11}$$

Given an ensemble of N particles with acting forces $\mathbf{F}_j$, the particles will move along with the generated fluid velocity field with

$$\mathbf{v}_i(\mathbf{r}_i) = \sum_{j=1}^{N} \boldsymbol{\mu}_{ij}(\mathbf{r}_i, \mathbf{r}_j)\mathbf{F}_j, \tag{2.12}$$

with the mobility matrix $\boldsymbol{\mu}_{ij}$. For finite size particles, the no-slip boundary condition on the particle surface is approximately taken into account via a multipole expansion to second order in terms of the particle radii a_i [40, 41],

$$\boldsymbol{\mu}_{ij}(\mathbf{r}_i, \mathbf{r}_j) = \left(1 + \frac{a_i^2}{6}\nabla^2_{\mathbf{r}_i}\right)\left(1 + \frac{a_j^2}{6}\nabla^2_{\mathbf{r}_j}\right)\mathbf{G}(\mathbf{r}_i, \mathbf{r}_j) \tag{2.13}$$

for $i \neq j$ and $r_{ij} > (a_i + a_j)$. For bulk flow, this leads to the Rotne-Prager tensor for the hydrodynamic interaction between spherical particles [42]. In unbounded flow, the self mobility tensor $\boldsymbol{\mu}_{ii}$ is diagonal and determined by the mobility of a single sphere with radius a, $\mu_{ii}^{\alpha\beta} = \mu_0\delta^{\alpha\beta}$ with $\mu_0 = 1/(6\pi\eta a)$.

Close to a no-slip boundary, the self mobility tensor is obtained from eqs. (2.9, 2.13) in the limit $\mathbf{r}_i \to \mathbf{r}_j$ and regularized far away from the surface by the bulk sphere mobility μ_0 [41]. This leads to different mobilities for perpendicular and lateral motion with respect to the interface,

$$\mu_\parallel(z) = \mu_0\left[1 - \frac{9}{16}\frac{a}{z} + \frac{1}{8}\left(\frac{a}{z}\right)^3\right] + O\left(\frac{a}{z}\right)^4 \tag{2.14}$$

$$\mu_\perp(z) = \mu_0\left[1 - \frac{9}{8}\frac{a}{z} + \frac{1}{2}\left(\frac{a}{z}\right)^3\right] + O\left(\frac{a}{z}\right)^4 \tag{2.15}$$

dependent on the distance z from the interface. The self mobility decreases near the boundary and its value for lateral motion is larger than for perpendicular motion with respect to the boundary [39].

To illustrate the hydrodynamic effects at a no-slip boundary, Fig. 2.1 shows the streamlines (solid lines) and lines of constant solvent velocity (broken lines) generated by a cylinder composed out of 10 beads that is moving perpendicular (a-d) and parallel (e-f) to the surface. The streamlines are given by the space curves which are always tangential to the fluid velocity field,

$$\frac{d\mathbf{r}(s)}{ds} = \mathbf{v}(\mathbf{r}(s)). \tag{2.16}$$

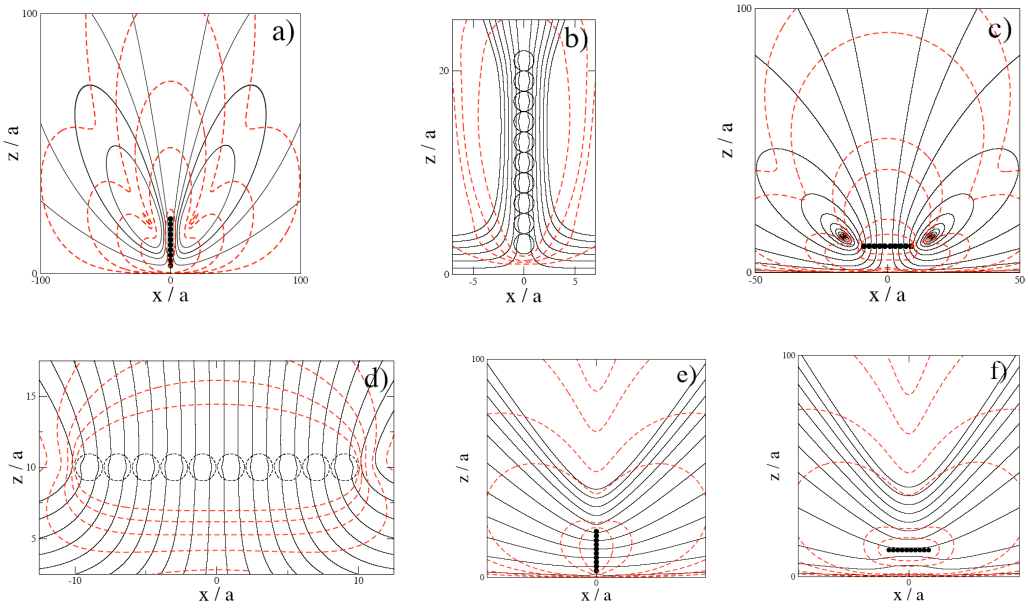

Figure 2.1.: Generated streamlines (solid black lines) for parallel (Fig. a) and b)) and for perpendicular (Fig. c) and d)) orientation, with respect to the surface normal, of a straight cylinder composed out of 10 beads that is moving vertically away from the surface. The plots show the far (Fig. a) and c)) and the near (Fig. b) and d)) field of the fluid velocity. Figs. e) and f) show the streamlines for a cylinder which is moving parallel to the surface in x-direction. The dashed red lines show the contour lines of the absolute value of the fluid velocity.

To second order in the multipole expansion, the fluid velocity field which is created by N spherical particles with acting forces $\mathbf{F}_j$ is obtained from eq. (2.7)

$$\mathbf{v}(\mathbf{r}) = \sum_{j=1}^{N} \left(1 + \frac{a^2}{6}\nabla^2_{\mathbf{r}_j}\right) \mathbf{G}^W(\mathbf{r}, \mathbf{r}_j)\mathbf{F}_j. \tag{2.17}$$

The streamlines shown in Fig. 2.1 are calculated by a numerical integration of eq. (2.16) with the velocity field given in eq. (2.17). The forces $\mathbf{F}_j$ on the beads of the cylinder are numerical adjusted such that each bead is moving with the same velocity. Two different orientations of the cylinder are displayed. It is interesting to observe that the presence of the wall leads to circulating flows in the far field (see e.g. a) and c)). For the lateral motion, an interesting symmetry-breaking occurs: In front of the cylinder the fluid is pushed away from the surface, behind the cylinder the fluid is moving towards the surface. This will be important for the calculation of the lift force of a cylinder in chapter 5.

2.2. Langevin equation

Since eq. (2.3) is a high dimensional partial differential equation, it is often more suitable to use the corresponding Langevin equation. The Langevin equation describes the stochastic time evolution of the coordinates of single particles instead of their probability distribution. Thermal fluctuations are incorporated via stochastic forces acting on the particles. For N particles with potential energy U in an external flow $\mathbf{v}_0(\mathbf{r})$, the Langevin equation is given by

$$\dot{\mathbf{r}}_i(t) = -\sum_{j=1}^{N} \boldsymbol{\mu}_{ij} \boldsymbol{\nabla}_{r_j} U(\{\mathbf{r}_N\}) + \sum_j \boldsymbol{\nabla}_{r_j} \mathbf{D}_{ij} + \mathbf{v}_0(\mathbf{r}_i) + \boldsymbol{\xi}_i(t), \tag{2.18}$$

which is equivalent to the Fokker-Planck diffusion equation in eq. (2.3) [5, 43, 44] for $\mathbf{v}_0 \equiv 0$. The random velocities ξ_i have zero mean and fulfill the fluctuation dissipation theorem,

$$\langle \xi_i^\alpha(t) \xi_j^\beta(t') \rangle = 2k_\mathrm{B}T\mu_{ij}^{\alpha\beta}\delta(t - t'). \tag{2.19}$$

This relation has to be satisfied in order to reproduce, in the stationary state, the appropriate equilibrium distribution which is given by the Boltzmann distribution $\propto \exp(-U(\{r_i\})/k_\mathrm{B}T)$. Therefore, N correlated random numbers have to be calculated at each timestep which is implemented via a Cholesky decomposition of the mobility matrix [15]. Since the diffusion tensor $\mathbf{D}_{ij} = k_\mathrm{B}T\boldsymbol{\mu}_{ij}$ is in general not only dependent on the relative coordinates of the beads but also on their absolute position in space, the divergence term in the Langevin equation has to be added [5]. Note, that the divergence term vanishes for unbounded flow, but has to be retained in the presence of a no-slip wall.

In the simulations, polymers are composed out of N connected beads with radii a. The linkage is assured by some connecting potential, chosen according to the desired

polymer model. For the Brownian dynamics simulations, we use a rescaled, discrete version [15–17, 43–45] of eq. (2.18),

$$\tilde{\mathbf{r}}_i(t+\Delta t) - \tilde{\mathbf{r}}_i(\Delta t) = -\sum_{j=1}^{N} \tilde{\boldsymbol{\mu}}_{ij} \boldsymbol{\nabla}_{\tilde{r}_j} u(\{\tilde{\mathbf{r}}_N\}) + \sum_j \boldsymbol{\nabla}_{\tilde{r}_j} \tilde{\boldsymbol{\mu}}_{ij} + \tilde{\mu}_0 \tilde{\mathbf{v}}_0(\mathbf{r}_i) + \tilde{\boldsymbol{\xi}}_i(t). \quad (2.20)$$

All lengths are scaled by the bead radius, $\tilde{\mathbf{r}} = \mathbf{r}/a$ and energies by thermal energy, $u(\{\tilde{\mathbf{r}}_N\})k_\mathrm{B}T = U(\{\mathbf{r}_N\})$ which leads to rescaled mobilities $\tilde{\boldsymbol{\mu}}_{ij} = \boldsymbol{\mu}_{ij}\Delta t k_\mathrm{B}T/a^2$ with time step Δt and solvent velocity $\tilde{v} = va/(\mu_0 k_\mathrm{B}T)$. If the external velocity field is given by simple shear flow, $\tilde{\mathbf{v}}_0(\tilde{\mathbf{r}}) = \dot{\tilde{\gamma}}\tilde{\mathbf{r}}_z\hat{e}_x$, this rescaling scheme leads to a rescaled shear rate,

$$\dot{\tilde{\gamma}} = \dot{\gamma}\frac{a^2}{\mu_0 k_\mathrm{B}T}. \quad (2.21)$$

The random velocities which couple the system to a heat bath are modeled with Gaussian white noise and fulfill the fluctuation dissipation theorem, $\langle\tilde{\boldsymbol{\xi}}_i(t)\tilde{\boldsymbol{\xi}}_j(t')\rangle = 2\tilde{\boldsymbol{\mu}}_{ij}\delta(t-t')$. Numerically, the Cholesky decomposition of the mobility matrix is implemented with a LAPACK [46] routine, which considerably speeds up the computer simulations compared to an implementation given in ref. [47]. The rescaled time step $\tilde{\mu}_0 = \mu_0\Delta t k_\mathrm{B}T/a^2$ is chosen small enough such that discretization effects are negligible. Mostly, a value $\tilde{\mu}_0 = 10^{-4}$ is used in the hydrodynamic simulations.

Since the mobility matrix is a slowly varying function of the bead separation, it is not updated at every single timestep for computer time reasons. The update frequency is chosen differently for different polymer lengths. It has been checked that this procedure is a good approximation for the desired accuracy, see appendix A.1.

3. Polymers in shear flow

Any fluid flow past a solid boundary gives rise to shear flow. Especially for microfluidic applications with their high surface to volume ratio, surfaces are omnipresent. Therefore, the dynamics of particles immersed in shear flow is of special importance. Polymer solutions in external flow exhibit interesting rheological phenomena like shear thinning or thickening [48]. To analyze these properties, a profound understanding of polymer dynamics in shear flow is necessary.

Whereas birefringence or light scattering techniques are able to deliver insight into the average deformation and orientation of polymers in flow [10, 12], no explicit information on the trajectories of single molecules with high temporal resolution was traditionally obtained. Only since the last 15 years, single molecule dynamics in shear flow can be directly observed via fluorescence microscopy [13], see also Fig. 1.1. Large fluctuations in the chain extension are observed, suggesting an end-over-end tumbling motion. This stems from the fact, that simple shear flow can be decomposed into equal amounts of rotational and elongational flow. The polymer is rotated by the flow, and therefore is in configurations where it is compressed or elongated by the flow, see Fig. 3.1. The velocity gradient of the flow gives rise to hydrodynamic drag forces on the molecule. If the drag force is larger than the entropic force, which keeps the polymer in a coiled configuration, the polymer chain is elongated. The effect of the shear flow on the polymer extension is often given in terms of the dimensionless Weissenberg number $Wi = \dot{\gamma}\tau$ which is the product of the shear rate $\dot{\gamma}$ and the longest relaxation time τ of the polymer. For $Wi > 1$, the hydrodynamic drag exceeds the entropic force and the polymer is elongated by the flow.

From the direct imaging of the polymer motion [13], it was confirmed, that the extension of polymers in shear does not reach a stationary state. Rather, the polymer is repeatedly stretched and compressed. More than 30 years ago, de Gennes [49] proposed a simple dumbbell model to describe polymer dynamics in shear flow. For simple shear flow, he showed, that there exists no sharp coil-stretch transition in contrast to flows with unequal amount of elongational and rotational components. Different dumbbell models have been used extensively to examine quantities like viscosity, average extension or tumbling frequencies [50–53]. Due to the enormous increase of computer power over the last decades, simulations of more realistic polymer models [54–56] give further insight in the polymer dynamics.

Most publications only report for an increase in polymer extension with increasing shear [10, 13, 57, 58]. However, there is some experimental evidence that polymers are compressed again at very high shear rates from birefringence experiments [59, 60] which has not yet been observed in single molecule experiments. A compression at high shear rates is also seen in simulations of bead-rod models, but only without excluded volume interactions [61, 62]. Although hydrodynamic interactions amplify

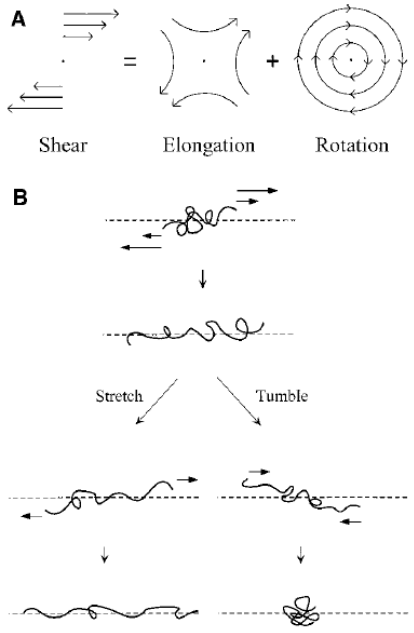

Figure 3.1.: Fig. A shows the decomposition of simple shear flow in elongational and rotational flow. Therefore, a polymer in shear flow will be either compressed or extended by the elongational flow component, dependent on its orientation. In Fig. B, the characteristics of the polymer motion are depicted. If the hydrodynamic drag on the polymer chain is large enough, the polymer is stretched by the shear flow and becomes aligned in the shear direction. Brownian motion can drive the polymer to a configuration in which the molecule is compressed by the shear flow, leading to a tumbling motion. Both figures are taken from Ref. [13].

this effect, the compression is also present for freedraining polymers. In the following sections, we want to identify the effects which lead to this compression at high shear rates. Starting from simple dumbbell calculations, a general introduction of polymer dynamics in shear flow is provided. Subsequently, we use various polymer models and analyze in detail the compression at high shear rates.

3.1. Simulations

In the simulations, the polymer dynamics in simple shear flow with shear rate $\dot{\gamma}$ is described by eq. (2.18) with $\mathbf{v}_0(\mathbf{r}_i) = \dot{\gamma} z_i \hat{e}_x$. A polymer is modeled by N connected beads with radii a and coordinates $\mathbf{r}_i$. The potential energy of the polymer $u(\{\mathbf{r}_N\}) = u_C(\{\mathbf{r}_N\}) + u_{LJ}(\{\mathbf{r}_N\})$ in eq. (2.20) consists of a potential $u_C(\{\mathbf{r}_N\})$, which acts on neighboring beads and assures the chain connectivity. Different functional forms for this potential are used to examine the dynamics and configurations of distinct polymer models. Also, the effect of excluded volume interactions are examined, which are implemented via a truncated, repulsive Lennard Jones potential

$$u_{LJ}(\{\mathbf{r}_N\}) = 4\varepsilon \sum_{\substack{i,j=1 \\ i \neq j}}^{N} \left[\left(\frac{2a}{r_{ij}} \right)^{12} - 2 \left(\frac{2a}{r_{ij}} \right)^{6} + 1 \right] \qquad \text{for } r_{ij} < 2a \tag{3.1}$$

with $r_{ij} = |\mathbf{r}_i - \mathbf{r}_j|$. This potential prevents sphere overlap and leads to a swelling of the chain in equilibrium. A value of $\varepsilon = 1.2$ is sufficient to keep overlapping of the

polymer beads at a negligible level in the simulations. For the simulations without excluded volume effects, the Lennard Jones potential is set to zero, $u_{LJ}(\{\mathbf{r}_N\}) \equiv 0$.

Special importance is put on the hydrodynamic interactions (HI). Since a polymer bead will drag the surrounding fluid along with it, this will influence also the other particles immersed in the fluid. The hydrodynamic interactions are incorporated via the mobility matrix defined in eq. (2.13). For unbounded flow, the mobility matrix is given by the Rotne-Prager Tensor [42],

$$\mu_{ij}^{\alpha\beta}(\mathbf{r}) = \frac{1}{8\pi\eta r}\left[\left(\delta^{\alpha\beta} + \frac{r^\alpha r^\beta}{r^2}\right) + \frac{2a^2}{r^2}\left(\frac{\delta^{\alpha\beta}}{3} - \frac{r^\alpha r^\beta}{r^2}\right)\right] \qquad \text{for} \quad r \geq 2a. \tag{3.2}$$

and[1]

$$\mu_{ij}^{\alpha\beta}(\mathbf{r}) \;=\; \frac{1}{6\pi\eta a}\left[\left(1 - \frac{9r}{32}\right)\delta_{\alpha\beta} + \frac{3r}{32a}\frac{r^\alpha r^\beta}{r^2}\right] \qquad \text{for} \quad r < 2a. \tag{3.3}$$

For the freedraining (FD) simulations, i.e. without hydrodynamic interactions, the mobility matrix is diagonal and independent of the polymer conformation,

$$\mu_{ij}^{\alpha\beta}(\mathbf{r}) = \delta_{ij}\delta^{\alpha\beta}\mu_0. \tag{3.4}$$

3.2. Dumbbell Model

A very crude, nevertheless helpful model for polymer dynamics is the dumbbell model, which consists of only two connected beads with radii a. The dynamics of this model in shear flow has been extensively studied before [50–53]. We use dumbbell models with three different connecting potentials ($\mathbf{r} = \mathbf{r}_1 - \mathbf{r}_2$):

$$u_c(r) = \begin{cases} \frac{\gamma}{2a^2} r^2 & \text{Harmonic dumbbell} \\ -\frac{\gamma R_0^2}{2a^2}\ln(1 - r^2/R_0^2) & \text{FENE dumbbell} \\ \frac{\gamma}{2a^2}(r - r_0)^2 & \text{Fraenkel dumbbell} \end{cases} \tag{3.5}$$

The Harmonic dumbbell is a good approximation for real polymers only for small distortions from their equilibrium configuration. In this regime, the free energy of a polymer is quadratically dependent on its extension, which leads to a restoring force which is linearly depending on the extension, just like a harmonic spring. Due to the finite contour length of real polymers, the restoring force diverges as the extension approaches the contour length L_0. The finite extensibility becomes apparent in non-linear force extension curves measured in polymer stretching experiments [63–65]. This finite extensibility is included in the FENE dumbbell by a divergence in the restoring force if the extension approaches the maximal extension R_0. For small extensions $r/R_0 \ll 1$, the FENE model is equal to the Harmonic dumbbell model. The Fraenkel dumbbell describes best the situation of stiff polymers, for which the end to end distance is always close to their contour length.

[1] In the simulations with excluded volume effects, sphere overlapping is negligible. Therefore, only the mobility matrix given in eq. (3.2) is used for the simulations with excluded volume effects.

In contrast to the FENE and Fraenkel dumbbell, an analytic solution can be given for the Harmonic dumbbell in shear flow. Neglecting hydrodynamic interactions and without excluded volume interactions, the Langevin equation eq. (2.18) for the bead connecting vector $\mathbf{r} = \mathbf{r}_1 - \mathbf{r}_2$ with the mobility matrix given in eq. (3.4) reads

$$\dot{\mathbf{r}}^x = -\frac{1}{\tau}\mathbf{r}^x + \dot{\gamma}\mathbf{r}^z + \boldsymbol{\xi}^x \tag{3.6}$$

$$\dot{\mathbf{r}}^y = -\frac{1}{\tau}\mathbf{r}^y + \boldsymbol{\xi}^y \tag{3.7}$$

$$\dot{\mathbf{r}}^z = -\frac{1}{\tau}\mathbf{r}^z + \boldsymbol{\xi}^z \tag{3.8}$$

with the inverse relaxation time $\tau^{-1} = 2\mu_0 k_\mathrm{B} T\gamma/a^2$ of the dumbbell and

$$\langle \xi^\alpha(t)\xi^\beta(t')\rangle = 4\mu_0 k_\mathrm{B} T\delta_{\alpha\beta}\delta(t-t'). \tag{3.9}$$

The analytic solution of the above equation reads [51]

$$\mathbf{r}^x(t) = e^{-t/\tau}\left[\mathbf{r}^x(0) + \dot{\gamma}t\mathbf{r}^z(0)\right] + \int_0^t dt'\, e^{-(t-t')/\tau}\left[\boldsymbol{\xi}^x(t') + \dot{\gamma}(t-t')\boldsymbol{\xi}^z(t')\right] \tag{3.10}$$

$$\mathbf{r}^z(t) = e^{-t/\tau}\mathbf{r}^z(0) + \int_0^t dt'\, e^{-(t-t')/\tau}\boldsymbol{\xi}^z(t'), \tag{3.11}$$

with the solution of the y-component analogous to the z-component. In the long time limit $t \to \infty$, where initial conditions are unimportant, the average distance of the two beads is calculated to be

$$R^2 \equiv \langle r^2\rangle = 6\mu_0 k_\mathrm{B} T\tau\left[1 + \frac{1}{6}\dot{\gamma}^2\tau^2\right]. \tag{3.12}$$

This implies, that the average extension of a Harmonic dumbbell is monotonically increasing with Weissenberg number $Wi = \dot{\gamma}\tau$.

In Fig. 3.2, simulation results are shown for the different dumbbell models. In Fig. 3.2a), the broken lines correspond to the prediction for the Harmonic dumbbell, eq. (3.12). Neither hydrodynamic interactions nor excluded volume effects, which are only important for small extensions of the dumbbell, lead to substantial changes in the dynamics. The data of the Harmonic dumbbell follow nicely the predicted scaling given in eq. (3.12), validating that the discretization scheme of the Langevin equation is a good approximation to the analytic solution. The extension of the Fraenkel dumbbell only follows this scaling at high shear rates. At low shear rates, the average extension is determined by the parameter r_0 in eq. (3.5). At high shear rates, the average extension is much larger than the equilibrium distance $R/r_0 \gg 1$. In this limit, the Fraenkel dumbbell is equal to the Harmonic dumbbell.

While the average extension for the Harmonic and Fraenkel dumbbells diverges for increasing shear rate, the FENE dumbbell captures the feature of finite extensibility of the polymer, Fig. 3.2b). Although there exists no analytic solution, this model is the most realistic one. For all three dumbbell models, the average extension is monotonically increasing with increasing shear rate.

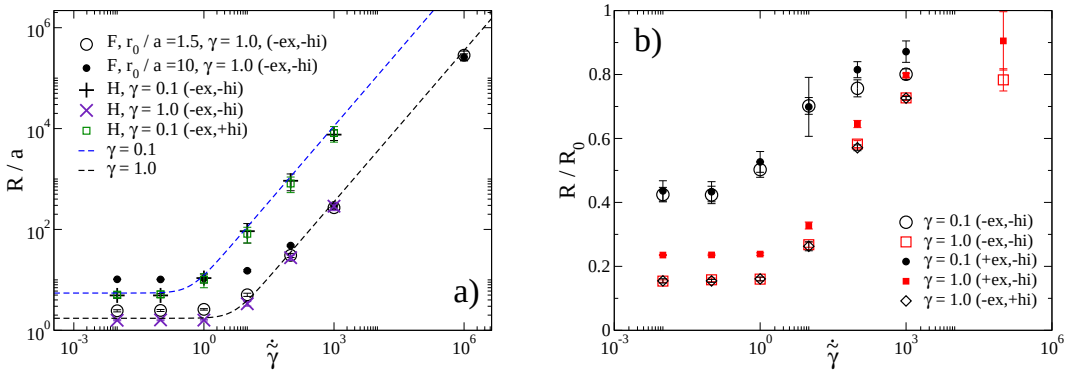

Figure 3.2.: Extension R, dependent on the shear rate $\dot{\tilde{\gamma}} = \dot{\gamma}a^2/(\mu_0 k_\mathrm{B}T)$ for the different dumbbell models with spring constants γ. The data show results with and without hydrodynamic interaction ($\pm$hi) and excluded volume effects ($\pm$ex). Fig. a) shows the extension scaled by the bead radius of Harmonic (H) and Fraenkel (F) dumbbells. The broken lines show the analytic result for the Harmonic dumbbell, eq. (3.12). In (b), the extension, scaled by the maximal distance $R_0/a = 10$ of FENE dumbbells is depicted.

3.3. Gaussian polymers

Since a simple dumbbell model is not able to capture effects of polymer dynamics that have to do with internal modes, more realistic polymer models are now considered. In the Gaussian model, the polymer consists of N harmonically connected beads, i.e. the connecting potential is given by

$$u_C(\{\mathbf{r}\}_N) = \sum_{i=1}^{N-1} \frac{\gamma}{2a^2} r_{ii+1}^2 \qquad \text{with} \quad \mathbf{r}_{ij} = \mathbf{r}_i - \mathbf{r}_j. \tag{3.13}$$

For an ideal polymer, the force constant $\gamma = 3(a/b)^2$ is given by the ratio between the Kuhn length b and the radius a of one polymer segment[2]. Without excluded volume interactions and without HI, this polymer model corresponds to the so called Rouse model. Its special importance stems from the fact that due to the linear force law between the beads, analytic solutions for quantities like the average extension or relaxation times can be derived via a normal mode analysis. The equation of motion for the ith bead within the Rouse model is obtained from eq. (2.18) with the diagonal

[2]The Kuhn length represents the stiffness of the polymer chain and is defined by the end to end distance L and the contour length L_0 of the polymer: $b = \langle L^2 \rangle / L_0$.

mobility matrix given in eq. (3.4),

$$\dot{\mathbf{r}}_1 = -\frac{1}{\tau}(\mathbf{r}_1 - \mathbf{r}_2) + \hat{\sigma}\mathbf{r}_1 + \boldsymbol{\xi}_1 \tag{3.14}$$

$$\dot{\mathbf{r}}_i = -\frac{1}{\tau}(2\mathbf{r}_i - \mathbf{r}_{i-1} - \mathbf{r}_{i+1}) + \hat{\sigma}\mathbf{r}_i + \boldsymbol{\xi}_i \tag{3.15}$$

$$\dot{\mathbf{r}}_N = -\frac{1}{\tau}(\mathbf{r}_N - \mathbf{r}_{N-1}) + \hat{\sigma}\mathbf{r}_n + \boldsymbol{\xi}_N \tag{3.16}$$

with the flow field $\hat{\sigma} = \delta_{xz}\dot{\gamma}$ and $\tau^{-1} = \mu_0 k_\mathrm{B} T\gamma/a^2$. In the continuum limit, in which the polymer is represented as a continuous space curve, a transformation to normal modes

$$\mathbf{X}_p = \frac{1}{N}\int_0^N dn\ \cos(p\pi n/N)\mathbf{r}_n(t) \qquad \text{with} \quad p = 0, 1, 2, ... \tag{3.17}$$

leads to a decoupling of different modes [5],

$$\dot{\mathbf{X}}_p = -\tau_p^{-1}\,\mathbf{X}_p + \hat{\sigma}\mathbf{X}_p + \mathbf{f}_p \tag{3.18}$$

with

$$\tau_p^{-1} = \frac{k_\mathrm{B} T\mu_0\gamma}{a^2}\left(\frac{p\pi}{N}\right)^2. \tag{3.19}$$

The random forces $\mathbf{f}_p$ are uncorrelated for different modes,

$$\langle f_p^\alpha(t) f_q^\beta(t')\rangle = \delta_{pq}\delta^{\alpha\beta}\delta(t-t')2k_\mathrm{B}T/\zeta_p \tag{3.20}$$

with $\zeta_0 = N/\mu_0$ and $\zeta_p = 2N/\mu_0$ for $p = 1, 2, ...$. Therefore, the equation of motion for the single modes are independent of each other and have the same form as the kinetic equation of the harmonic dumbbell. The solutions are similar to those given in eqs. (3.10, 3.11). In the long time limit, $t \to \infty$, the correlations between the single modes are given by [66]

$$\begin{aligned} \langle X_p^y(t)X_q^y(t)\rangle = \langle X_p^z(t)X_q^z(t)\rangle &= \delta_{pq}\, k_\mathrm{B}T\frac{\tau_p}{\zeta_p} \\ \langle X_p^x(t)X_q^x(t)\rangle &= \delta_{pq}\, k_\mathrm{B}T\frac{\tau_p}{\zeta_p}\left[1 + \frac{1}{2}\left(\dot{\gamma}\tau_p\right)^2\right]. \end{aligned} \tag{3.21}$$

The averages of the product between different Cartesian components yield zero, i.e. $\langle X_p^\alpha X_p^\beta\rangle \propto \delta_{\alpha\beta}$. The coordinates of the beads $\mathbf{r}_i$ are given by the backward transformation,

$$\mathbf{r}_i = \mathbf{X}_0 + 2\sum_{p=1}^{\infty}\mathbf{X}_p\cos\left(i\frac{p\pi}{N}\right). \tag{3.22}$$

In equilibrium, the polymer chain is in a coiled configuration. The components of the radius of gyration tensor $\mathbf{R}_g$ characterize the extension of the polymer coil in the Cartesian direction α,

$$(R_g^\alpha)^2 = \frac{1}{N}\sum_{i=1}^{N}(r_i^\alpha - R_G^\alpha)^2 \tag{3.23}$$

with the center of mass $\mathbf{R}_G$ of the polymer. Within the framework of the Rouse model, the radius of gyration can be calculated analytically. Noting that the center of mass is given by $\mathbf{R}_G = \mathbf{X}_0$,

$$\langle (R_g^\alpha)^2 \rangle = \frac{1}{N} \sum_{i=1}^{N} \left\langle \left[2 \sum_{p=1} X_p^\alpha \cos\left(i \frac{p\pi}{N} \right) \right]^2 \right\rangle \tag{3.24}$$

$$\approx \frac{4}{N} \int_0^N di \sum_{p,q=1} \langle X_p^\alpha X_q^\alpha \rangle \cos\left(i \frac{p\pi}{N} \right) \cos\left(i \frac{q\pi}{N} \right). \tag{3.25}$$

Using eq. (3.21) and integrating the above equation leads to the components of the gyration tensor [66],

$$(R_g^z)^2 = (R_g^y)^2 = \frac{Na^2}{\gamma} \sum_{p=1}^{\infty} \left(\frac{1}{p\pi} \right)^2 = \frac{Na^2}{6\gamma} \tag{3.26}$$

$$(R_g^x)^2 = \frac{Na^2}{6\gamma} \left[1 + \frac{\pi^4}{315} (\dot{\gamma}\tau_1)^2 \right]. \tag{3.27}$$

The radius of gyration is monotonically increasing with Weissenberg number $Wi = \dot{\gamma}\tau_1$. Fig. 3.3 shows the x–component of the radius of gyration for a $N = 100$ polymer together with the above prediction. Eq. (3.27) nicely fits to the simulation data. Including the repulsive Lennard Jones potential (+ex) leads to a swelling of the polymer chain at zero shear rate. At elevated shear rates, excluded volume interactions do not have a big effect on the results, since the polymer is greatly extended and sphere overlapping occurs very sparsely. Excluded volume effects also lead to a coupling between the different Cartesian components, thus there exists no simple analytic solution as for the Rouse model.

With included hydrodynamic interactions (+hi), the shear-extension curve does not change qualitatively. At low shear rates the polymer is less extended compared to the freedraining case. The hydrodynamic interactions screen the shear flow, therefore less drag is exerted on the polymer. At high shear rates, where the polymer is strongly elongated and the inter bead distances become large, hydrodynamic interactions become unimportant and the extension is equal to the freedraining situation.

3.4. Polymers with constant contour length

One major drawback of the Gaussian polymer model is the neglect of the finite extensibility. Within simulations, a more realistic model includes the constant contour length of the polymer by using Fraenkel springs between the polymer beads,

$$u_C(\{\mathbf{r}_N\}) = \sum_{i=1}^{N-1} \frac{\gamma}{4a^2} (|\mathbf{r}_i - \mathbf{r}_{i+1}| - 2a)^2. \tag{3.28}$$

For large enough values of γ, contour length fluctuations of the chain become negligible. A value of $\gamma = 10^4$ in the simulations is sufficient to keep the inter bead distance close to 2 at moderate shear rates. For very high shear rates, the spring constant is increased to keep the contour length constant.

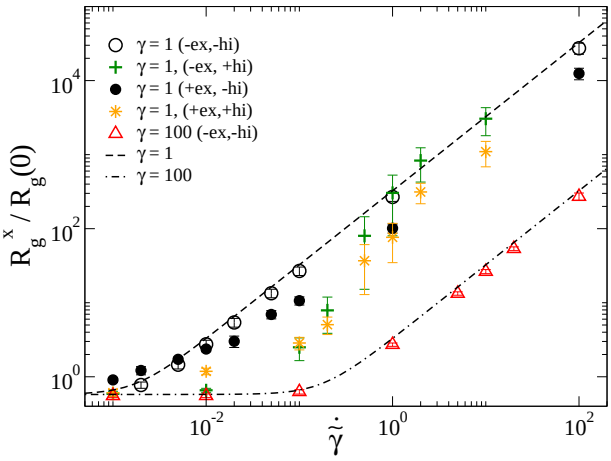

Figure 3.3.: x-component of the radius of gyration for a $N = 100$ Rouse polymer (symbols), dependent on the rescaled shear rate $\tilde{\dot{\gamma}} = \dot{\gamma}a^2/(\mu_0 k_B T)$. $R_g(0)$ denotes the absolute value of the gyration radius, $R_g = [(R_g^x)^2 + (R_g^y)^2 + (R_g^z)^2]^{1/2}$ at zero shear rate. The lines show the analytic result for the Rouse model, given in eq. (3.27).

3.4.1. Extension in shear flow

To characterize the extension of the polymer, the radius of gyration R_g and the end to end distance L in dependence of the shear rate is shown in Figs. 3.4 and 3.5. Initially, the polymer extension is increasing with increasing shear rate for all considered polymer models. With included hydrodynamic interactions, the polymers are stretched more slowly, Fig. 3.4a). This is due to the fact that the shear flow is screened inside the polymer coil, leading to less drag on the beads. The increase in relative extension with shear strength is larger for long polymers since the drag of the flow increases with the size of the polymer coil, Fig. 3.5. As can be seen in Fig. 3.4a), the normalized extension of chains without excluded volume effects is larger, consistent with other publications [61]. Nevertheless, this is due to the smaller size of a polymer coil in equilibrium when there is no repulsion between the beads. The absolute value of the polymer extension is similar at moderate shear rates.

A further increase in the shear rate leads to a noticeable effect: after the initial increase with shear rate, the extension of the polymers with HI starts to decrease for $\tilde{\dot{\gamma}} \gtrsim 1$. The freedraining polymers only show this compression at high shear rates if excluded volume interactions are absent. This effect is biggest for the polymers with hydrodynamic interactions where the beads can penetrate each other. There, the radius of gyration becomes even smaller than its equilibrium value, see Fig. 3.5. For longer polymers, this compression effect is more pronounced. A compactification of polymers in shear flow is only seen for polymers with $N \gtrsim 40$ (+ex,+hi). This is consistent with the dumbbell results, i.e. $N = 2$, in section 3.2, where no compression for dumbbells was observed.

At the shear rate with maximal extension, $\tilde{\dot{\gamma}} \sim 1(10)$ for the HI (FD) polymers,

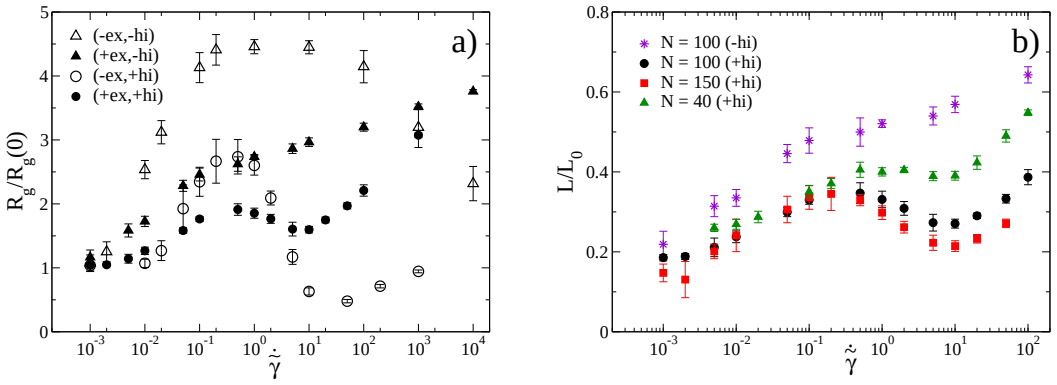

Figure 3.4.: a) Normalized radius of gyration versus rescaled shear rate for $N = 100$ polymer chains. The data show the dependence of R_g on excluded volume (±ex) and hydrodynamic (±hi) interactions. b) Average end to end distance $L = |\mathbf{r}_N - \mathbf{r}_1|$ of polymers with excluded volume interaction. The polymers are stronger stretched without hydrodynamic interaction (-hi). The FD polymer does not show the compression at high shear rates.

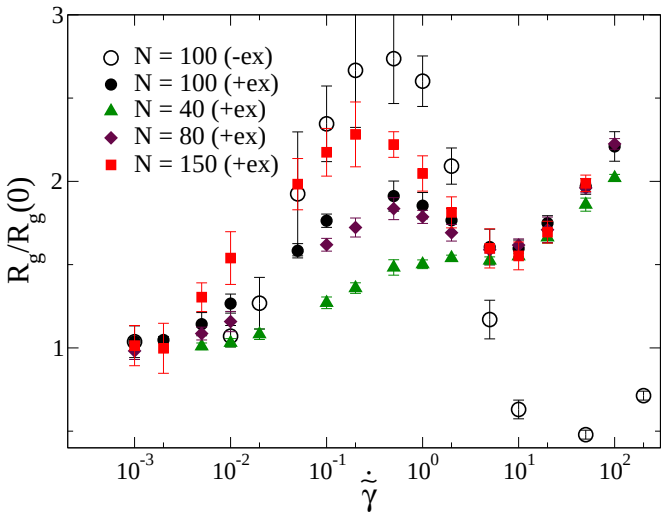

Figure 3.5.: Normalized radius of gyration versus rescaled shear rate for polymer chains of different lengths. Hydrodynamic interactions are included for all polymers. One can see the effect of excluded volume interactions.

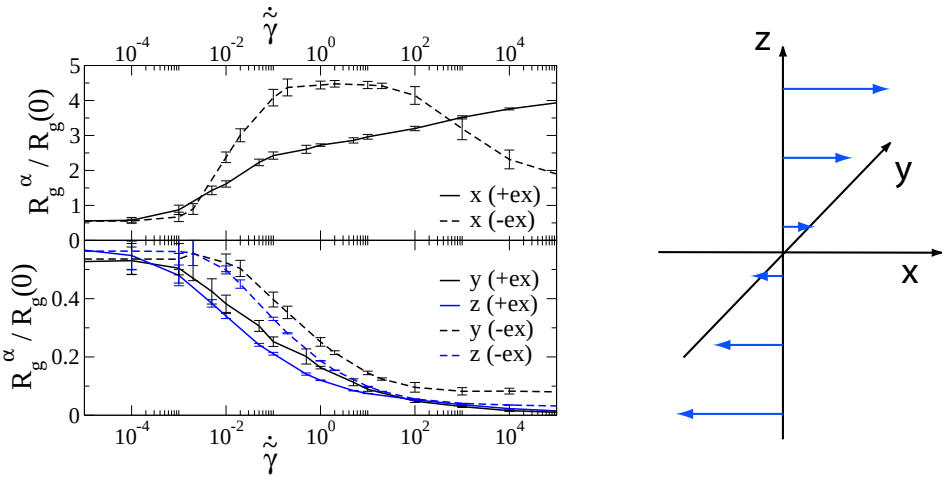

Figure 3.6.: Cartesian components of the radius of gyration for a $N = 100$ polymer without hydrodynamic interactions. On the right side, the coordinate system is shown. The blue arrows denote the direction of the shear flow.

the polymers are far from being fully extended most of the time. The average end to end distance is in the range between 30 % and 50 % of the polymer contour length, see Fig. 3.4b). The extension of polymers with different lengths in shear flow is found to be a universal function of the Weissenberg number Wi [17, 58], the product of the shear rate and the relaxation time of the polymer. From the simulations, the relaxation time of a $N = 100$ polymer (+ex,+hi) is $\tilde{\tau} = \tau a^2/(\mu_o k_B T) \approx 200$, see appendix A.2.2. With the shear rate at maximum extension $\dot{\tilde{\gamma}} \approx 0.5$, this corresponds to a Weissenberg number $Wi = \dot{\tilde{\gamma}}\tilde{\tau} \approx 100$. In experiments on 22 μm λ-DNA [13] a mean maximum fractional extension of roughly 40 % is observed at shear rates of 4 s^{-1} which corresponds to $Wi \simeq 80$ with the experimentally measured relaxation time $\tau = 19$ s. Hence, the simulation data of the polymer extension with HI and excluded volume interactions are in good agreement with these experiments.

As polymers in shear flow align in the direction of the shear, the x-component of the gyration tensor is largest. Fig. 3.6 shows the Cartesian components of the radius of gyration for freedraining polymers. The y- and z-components decrease monotonically with increasing shear rate, with the z component always smaller. The x-component is initially increasing with increasing shear rate. Without excluded volume interactions, it decreases at high shear rates. The x-component of the gyration radius is much larger than the other components. Thus, the polymer is strongly aligned with the x-axis, resembling a one dimensional object at high shear rates. In Fig. 3.7, snapshots of a FD polymer without excluded volume interactions at different shear rates are shown. From the histogram of R_g^x in Fig. 3.8 it is clearly seen that without excluded volume effects, a strong compression is present at high shear rates. At the lowest depicted shear rate $\dot{\tilde{\gamma}} = 1$, the polymer gets fully extended from time to time which is seen from the last peak in the graph. With increasing shear, the distribution becomes more narrow and fully extended polymer configurations have negligible statistical weight.

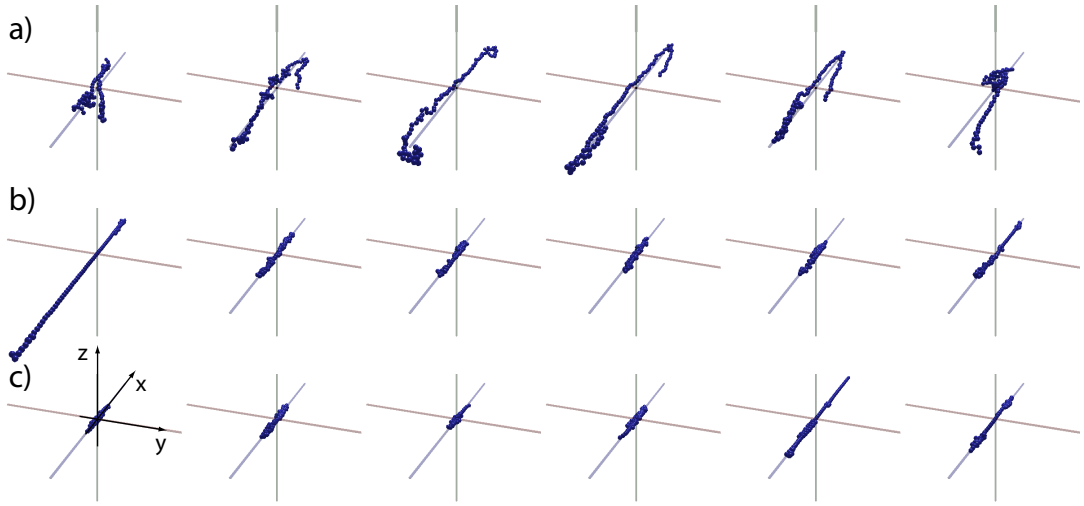

Figure 3.7.: Snapshots of a $N = 100$ freedraining polymer without excluded volume interactions at $\dot{\tilde{\gamma}} = 1$ (a), $\dot{\tilde{\gamma}} = 10^3$ (b) and $\dot{\tilde{\gamma}} = 10^6$ (c).

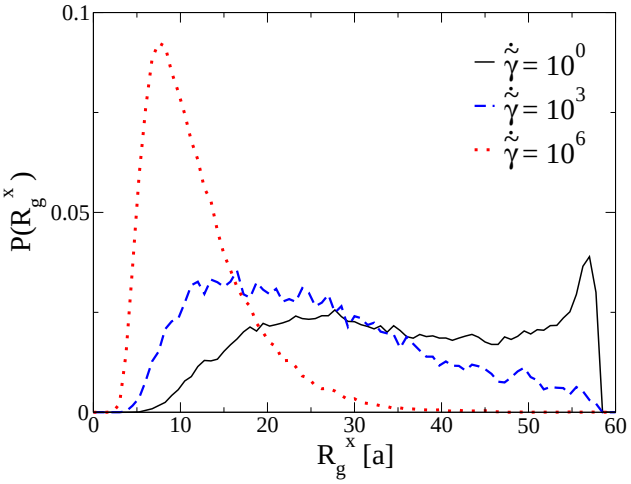

Figure 3.8.: Histogram of the x-component of the gyration radius of a $N = 100$ FD polymer without excluded volume interactions at different shear rates.

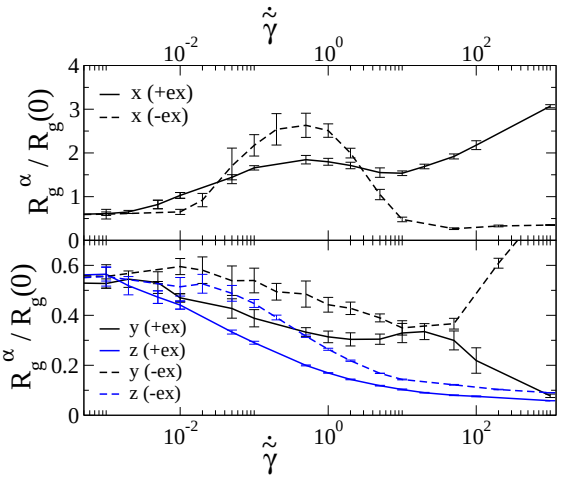

Figure 3.9.: Components of the radius of gyration for a $N = 100$ polymer with included hydrodynamic interactions.

Also with included hydrodynamic interactions, see Fig. 3.9, the x-component of the gyration radius is dominant. Compared to the freedraining results, the y- and z-components decay more slowly with increasing shear rate. The polymer is stronger compressed in the z-directions than in the y-direction, in agreement with simulations on long DNA molecules [58]. With excluded volume interactions, the y-component is slightly increasing for $\dot{\tilde{\gamma}} \gtrsim 10$, the shear rate at which the x-component has its minimum. Since the polymer is compressed in the x-direction, the polymer beads have to evade in the other directions. At very high shear rates, the polymer is elongated again in the x-direction.

Without excluded volume interactions, the configuration is even more different compared to the freedraining case. After the shear rate of minimum extension, the y-component becomes even larger than the x-component. At these shear rates, the polymer resembles an ellipsoid with its long axis aligned along the direction perpendicular to the shear plane. This alignment of polymer chains is also observed in experiments [59, 60]. This is in striking difference to the polymer alignment at moderate shear rates where the polymer is aligned with its longest axis along the x-direction. Configurations at different shear rates are shown in the snapshots taken from the simulation trajectories in Fig. 3.10.

Histograms of the different components of the gyration radius for a polymer with HI and without excluded volume interactions are shown in Fig. 3.11, together with parts of the trajectories. The depicted shear rates correspond to the maximum and minimum extension of the polymer. At $\dot{\tilde{\gamma}} = 0.5$, the trajectory of the x-component exhibits big fluctuations which lead to the broad probability distribution. This broad distribution is due to the tumbling motion of the polymer. At $\dot{\tilde{\gamma}} = 10$, single, very narrow peaks in the trajectory of the x-component are present. They have negligible statistical weight since the histogram for the x-component does not show a broad

distribution. If a protrusion of the compressed polymer in the x-direction occurs, it is rapidly pulled back inside the polymer coil. The distributions of the y- and z-component are narrow and do not change qualitatively with shear rate. Their trajectories do not show the peak like structure of the x-component.

3.4.2. Shear rates at maximum / minimum extension

From Fig. 3.5 it is seen, that the shears rate at minimum and maximum extension depend on the polymer length. To determine the position of the extrema, the radius of gyration versus the logarithm of the shear rate was fitted in an appropriate region to a parabolic function. Fig. 3.12 shows the results of the fitting procedure for all considered polymers with included hydrodynamic interactions. From the double logarithmic scale in Fig. 3.12, the position of the extrema seems to be a power law of the polymer length. With excluded volume interactions, the position of the minimal polymer extension is increasing with increasing polymer length with $\dot{\tilde{\gamma}}^{-} \sim (L/a)^{0.7}$. If the beads are free to penetrate each other, the position of minimum extension is decreasing with shear rate. The shear rate at maximum extension of the polymer chains is decaying for longer polymers, $\dot{\tilde{\gamma}}^{*} \sim (L/a)^{-1.4}$. For the position of the maximum, excluded volume effects only lead to minor changes as expected: the structure of the polymer at maximum extension is quite open and overlaps between the polymer beads occur sparsely.

Within the Zimm-Model and excluded volume interactions, the relaxation time of a polymer is increasing with polymer length, $\tau \sim N^{3\nu} a^3 \eta / k_{\mathrm{B}} T$ with $\nu = 0.6$ [5]. This implies, that the Weissenberg number at which the polymer extension starts to decrease with increasing shear is only weakly dependent on the polymer length, $Wi^{*} = \dot{\tilde{\gamma}}^{*} \tilde{\tau} \sim (L/a)^{0.4}$. Indeed, it was found before that the extension of polymers with different length in shear flow have the same form, if the extension as a function of the Weissenberg number is plotted [17, 58].

3.4.3. Rotation frequency

Further insight can be achieved by analyzing the rotational frequency ω_L of the polymers in shear flow. The rotation frequency is determined via the calculation of the angular momentum $\mathbf{L} = \hat{\mathbf{I}} \cdot \boldsymbol{\omega}_L$ with the inertia tensor $\hat{\mathbf{I}}$. The angular momentum and the inertia tensor are calculated for each configuration in the trajectories. Details of the computation of the angular velocity are given in appendix A.3. This definition of the rotational frequency has the advantage that ω_L also includes internal rotation of the polymer: ω_L can also be finite for constant external shape of the polymer. Such an internal rotation, also called tank treading, is often observed for the dynamics of vesicles in shear flow [67, 68]. From symmetry arguments, the only component which has a finite average is ω_L^y.

Whereas the rotational component of the shear flow is linearly increasing with shear rate, the rotation frequency of polymers does not. A polymer is distorted in the flow and thermal fluctuations lead to a sub-linear scaling of the tumbling frequency with shear rate. The tumbling frequency of a polymer in shear flow can be calculated

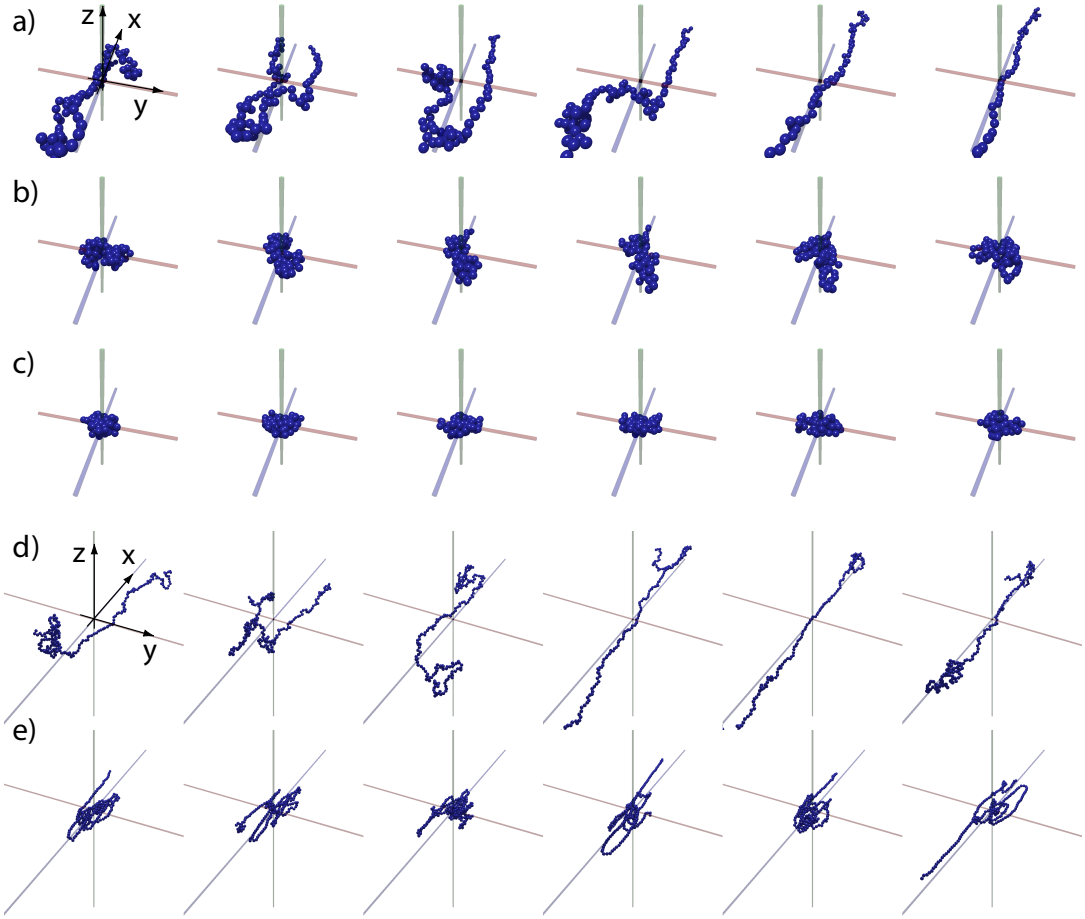

Figure 3.10.: Snapshots of polymers with included hydrodynamic interactions. Figs. (a-c) show a $N = 100$ polymer without excluded volume interactions at $\dot{\tilde{\gamma}} = 0.5$ (a), $\dot{\tilde{\gamma}} = 10.0$ (b) and $\dot{\tilde{\gamma}} = 50.0$ (c). In Figs. (d,e), configurations of a $N = 200$ polymer with excluded volume interactions at $\dot{\tilde{\gamma}} = 0.1$ (d) and $\dot{\tilde{\gamma}} = 10$ (e) are depicted.

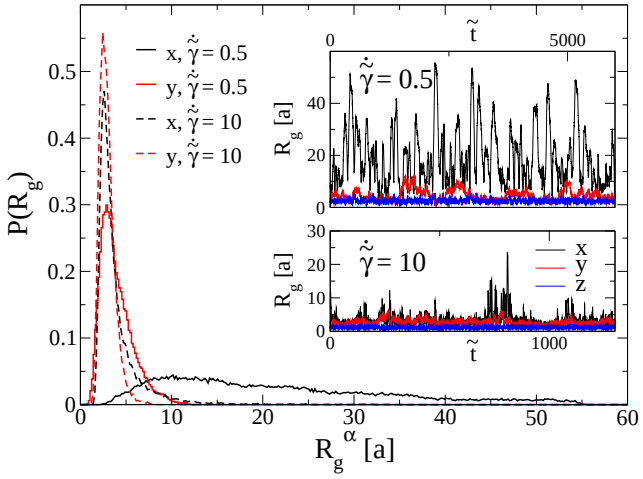

Figure 3.11.: Histograms for the components of the radius of gyration for a $N = 100$ polymer (-ex,+hi). The insets show parts of the simulation trajectory of the gyration tensor at $\tilde{\dot{\gamma}} = 0.5$ (upper inset) and $\tilde{\dot{\gamma}} = 10$ (lower inset).

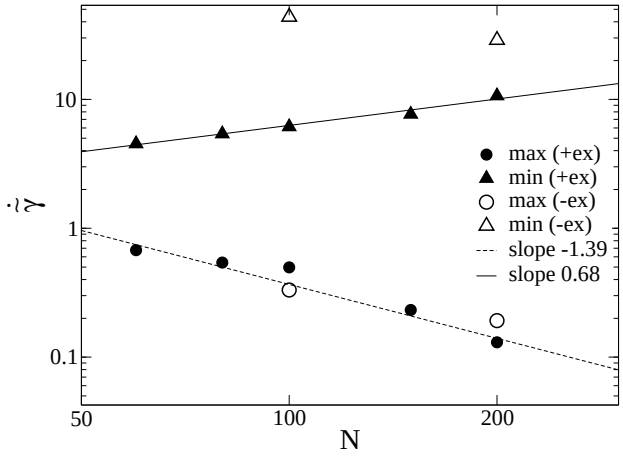

Figure 3.12.: Position of the extrema of the radius of gyration for polymer with and without excluded volume interaction but with included hydrodynamic interactions. The positions are obtained by fitting the data in an appropriate region to a parabolic function.

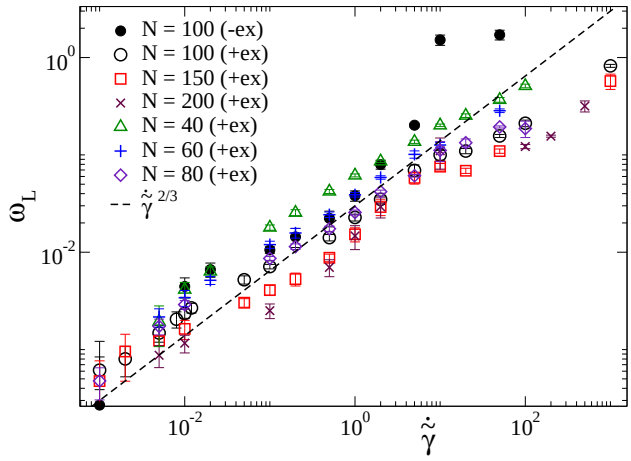

Figure 3.13.: Rotational frequency $\tilde{\omega}_L^y = \omega_L^y \; a^2/(\mu_0 k_B T)$ for polymers of different length. Hydrodynamic interactions are included for all polymers. The broken line is a guide to the eye with $\propto \tilde{\dot{\gamma}}^{2/3}$.

using a dumbbell model. It is found, that the mean tumbling frequency can be expressed by $\omega_L \propto \tau^{-1} Wi^{2/3} (R_g/R)^{2/3}$ for $Wi \gg 1$ [69]. R_g is the equilibrium gyration radius, R the polymer extension in shear and τ denotes the relaxation time of the polymer. For small extensions $R \ll L_0$, the extension is linearly dependent on the Weissenberg number, $R/R_g \propto Wi$. Then, the tumbling frequency is independent of the Weissenberg number and given by the inverse relaxation time of the polymer, $\omega_L \propto \tau^{-1}$. In the non-linear extension limit, $R \sim L_0$, the polymer is substantially stretched and therefore has the configuration of a rigid rod. This leads to a tumbling frequency $\omega_L \propto \tau^{-1} Wi^{2/3}$. In experiments with 22 and 84 μm long DNA, tumbling frequencies are found to scale with $Wi^{2/3}$ [55, 69]. This scaling is also observed in numerical simulations at high shear rates [70].

In Fig. 3.13, the mean rotation frequencies $\langle \omega_L^y \rangle$ for polymers of different length are shown. The data are consistent with the expected $\tilde{\dot{\gamma}}^{2/3}$ scaling. Also, the rotation frequency increases with decreasing polymer length since the relaxation time increases for longer polymers. Without excluded volume interactions, the rotation frequency strongly increases in the shear rate region where the compression takes place. This is due to the fact that at these shear rates, the polymer is very compact and therefore rotates faster.

3.5. Semiflexible polymers

Until now, results for flexible polymers in shear flow were shown. Many flow experiments use DNA molecules which exhibit a bending stiffness. Therefore, simulations for semiflexible polymers are performed. In addition to the connecting potential in

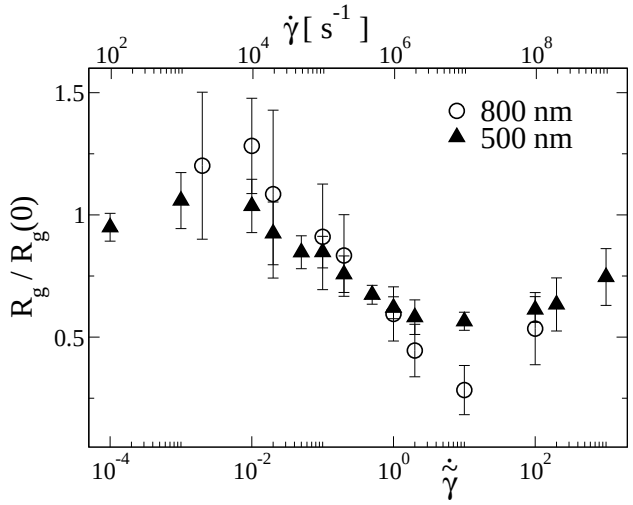

Figure 3.14.: Normalized gyration radius for polymers with the parameters of 500 nm and 800 nm long DNA with hydrodynamic and excluded volume interactions. The upper x-axis shows the unscaled shear rate $\dot{\gamma} = \tilde{\dot{\gamma}}\ \mu_0 k_\mathrm{B}T/a^2 = \tilde{\dot{\gamma}}\ k_\mathrm{B}T/(6\pi\eta a^3)$ for $\eta = 0.22$ Pas, $a = 1$ nm and $k_\mathrm{B}T = 4 \times 10^{-21}$ J at $T = 300$ K, the parameters of the single molecule experiments in [13]. η here corresponds to a highly viscous liquid compared to the viscosity of water, $\eta_{\mathrm{H_2O}} = 10^{-3}$ Pas.

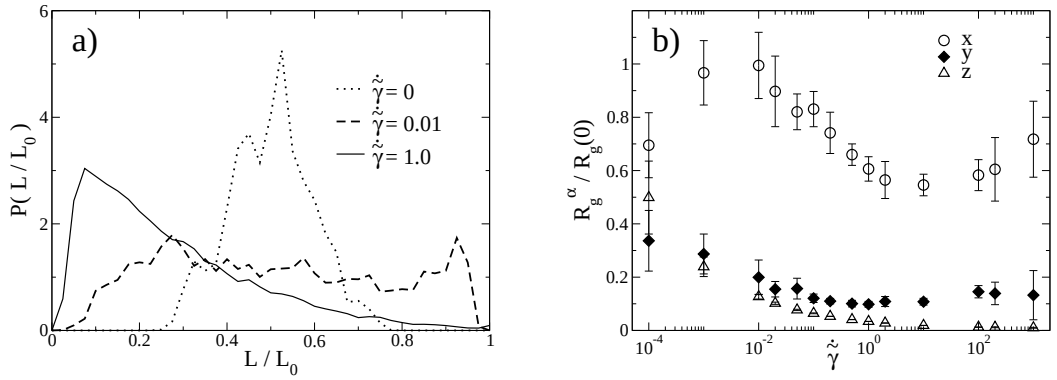

Figure 3.15.: a) Histograms of the end to end distance for the 500 nm long DNA model at different shear rates. b) Cartesian components of the radius of gyration for the 500 nm long DNA model.

eq. (3.28), a bending potential between the polymer beads is introduced,

$$u_C(\{\mathbf{r}_N\}) = \sum_{i=1}^{N-1} \frac{\gamma}{4a^2}(|\mathbf{r}_i - \mathbf{r}_{i+1}| - 2a)^2 + \sum_{i=2}^{N-1} \frac{l_p}{2a}(1 - \cos\vartheta_i). \tag{3.29}$$

ϑ_i denotes the bond angle at bead i, l_p is the so called persistence length which provides a measure of the polymer chain stiffness. For $L/l_p \ll 1$ the polymer resembles a rigid rod whereas for $L/l_p \gg 1$, the limit of a flexible chain is reached. A value of $l_p = 50$ nm is used, which corresponds to the persistence length of DNA at high salt solution [71].

Fig. 3.14 shows simulation data for polymer chains with included bending rigidity, hydrodynamic interactions and excluded volume effects. The parameters are chosen to render 500 nm and 800 nm long DNA. The diameter of a DNA chain is only 2 nm which leads to bead numbers of $N = 250$ and $N = 400$. In this regime, the polymers can not be considered as flexible since the contour length is at most 16 times the persistence length. The simulation of even longer DNA molecules within this model is not possible due to the enormous computational costs. Even for the used chain length, error bars are considerable due to the limited length of the trajectories.

Only a minor initial increase in polymer extension with increasing shear is observed. Due to the bending stiffness, the end to end distance at equilibrium already is 50% of the contour length, see Fig. 3.15a), thus even higher than the maximal extension of flexible polymers in shear flow. At zero shear rate, the end to end distance shows a relatively sharp distribution, Fig. 3.15a). At higher shear rates, the distribution becomes wider due to the tumbling motion of the polymer chain. Also for this polymer model, a compression at shear rates $\dot{\tilde{\gamma}} \gtrsim 0.01$ is observed. The Cartesian components of the radius of gyration show similar behavior as those for the flexible polymers. In Fig. 3.15b), the x-component of the gyration tensor is largest, which means that the polymer is aligned in the direction of the shear flow. The polymer is compressed along the other directions. This compression is strongest along the z-direction. At high shear rates, the conformation of the semiflexible polymer chain is very similar to the flexible chains. With increasing shear rate, the strain on the polymer becomes larger. Thus, the polymer is easily deformed at high shear strengths, just like flexible polymers. Therefore, the same scaling relations for the shear rates at maximum and minimum extension with polymer length found for flexible polymers in section 3.4.2 are expected to also hold for semiflexible polymers.

3.6. Scaling explanations

To summarize, nearly every considered polymer model with constant contour length is subject to a compression at high shear rates. In contrast, no dumbbell model captures this effect nor is it observed for short polymers or for the Rouse model. Hydrodynamic interactions and the neglect of excluded volume interactions amplify this effect, as there is no compression seen for freedraining polymers with excluded volume interactions. With included hydrodynamic interactions, the drag on the polymer is smaller since the shear flow is screened by the other polymer beads. If the beads are

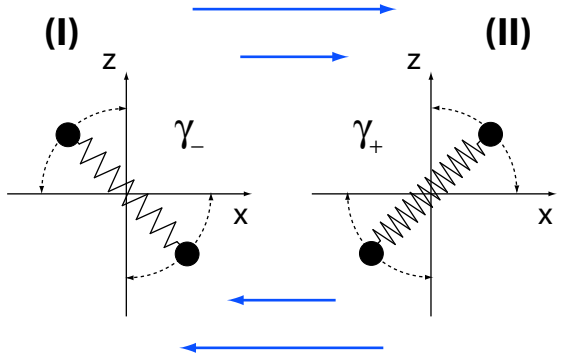

Figure 3.16.: Dumbbell model with two different spring constants, dependent on the dumbbell orientation. The blue arrows denote the direction of the shear flow. For configurations in which the dumbbell is compressed, a soft spring constant γ_- is used (I). If the dumbbell is stretched by the shear flow, a stiffer spring constant γ_+ is used (II).

free to penetrate each other, the polymer size shrinks which also leads to decreasing drag on the polymer. Consequently, the polymer coil is less extended by the flow.

The compression at high shear rates stems from the fact that polymer coils with constant contour length are more easily compressed than expanded. For example, a single hairpin is easily compressed in one direction since the polymer chain can evade in the other directions. In contrast, such a hairpin is only slowly extended, like a rope traveling over a pulley. With increasing shear rates, these folded polymer configurations are more abundant as can be seen in the snapshots, Fig. 3.10e). At low shear rates, the polymer structure is quite open and easily extended by the flow. At higher shear rates, the polymer is in a compact configuration and the constraining effect of the constant contour length is clearly visible: the shear flow mainly pulls on single hairpins which are only slowly unfolded by the flow. On the other hand, the polymer is easily compressed by the flow since it can evade in the $\hat{e}_y$ direction.

A further increase in the shear rate leads to an extension of the compact polymer. The polymer will be stretched if the strain ϵ during one half of the tumbling period overcomes some critical value. The length of this period is given by the inverse tumbling frequency $\omega_L^{-1} \sim \dot{\gamma}^{-2/3}\tau^{1/3}$. The stretching (and also compressive) force on the polymer is linear in shear rate which leads to

$$\epsilon \sim F_{\text{shear}}\omega_L^{-1} \sim \dot{\gamma}^{1/3}\tau^{1/3}R_g/\mu_0. \tag{3.30}$$

Therefore, the strain increases with increasing shear rate. At very high shear rates, the strain is large enough to unfold the polymer and the polymer is stretched again. Another argument for the final stretching can be given by considering the zero temperature limit which is reached in the limit $\dot{\tilde{\gamma}} \to \infty$. Almost all polymer configurations (except high symmetry configurations) lead to a completely stretched chain, aligned with the x–axis.

3.7. Anisotropic dumbbell

To validate these considerations, a dumbbell toy-model can be constructed which captures the above mentioned effects. Firstly, the dumbbell has to be more easily

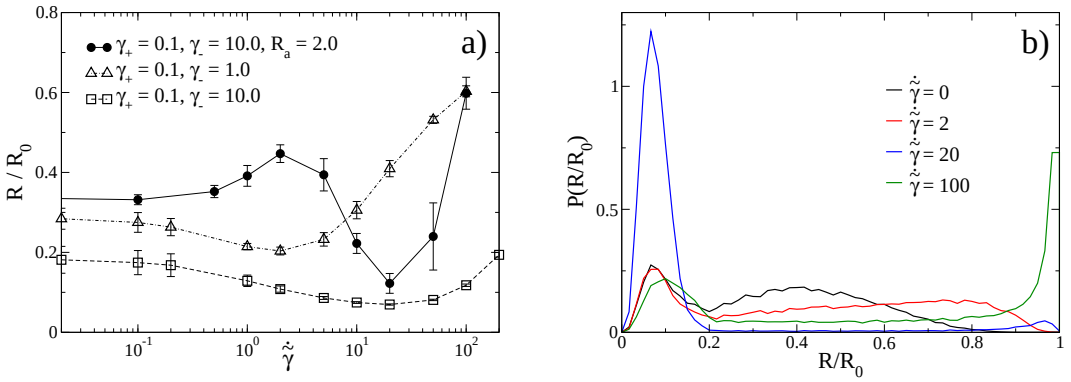

Figure 3.17.: a) Simulation results for a FENE dumbbell (-ex,-hi) with different spring constants for extension (γ_+) and compression (γ_-) and $R_0 = 10$. The solid circles show data of an anisotropic dumbbell where the different spring constants are only used if $R < R_a$. b) Normalized probability distribution of the extension of an anisotropic FENE dumbbell with $\gamma_- = 0.1$, $\gamma_+ = 10.0$, $R_0 = 10$ and $R_a = 2$ at different shear rates.

stretched than compressed by the shear flow. Using a FENE dumbbell, the force extension curve could be modeled with two different spring constants: for configurations where the shear flow compresses the dumbbell, (I) in Fig. 3.16, a softer spring (γ_-) is used. For configurations in which the dumbbell is stretched by the shear (II), a stiffer spring constant (γ_+) is assumed. This model shows an decreasing extension with increasing shear, see the open symbols in Fig. 3.17a).

To account for the initial extension at moderate shear rates, the model has to be modified. Only compact polymer configurations are more easily compressed than extended. Therefore, the two different spring constants are only used if the extension is below some threshold, $R < R_a$, otherwise the spring constant $\gamma = \gamma_-$ is independent of the dumbbell orientation. The simulations of such a dumbbell, full circles in Fig. 3.17a), show indeed the same behavior as observed in the polymer simulations. Although the parameters of the models have to be adjusted for the compression effect to occur, the non monotonous shear extension curves from section 3.4.1 are qualitatively reproduced.

However, this phenomenological dumbbell model does not yield the correct equilibrium distribution, which is a Gaussian for flexible polymers. In the histograms shown in Fig. 3.17b), the feature of two different spring constants is clearly visible, as there are two different peaks present in the equilibrium case. This is due to the very artificial force extension curve. However, even if this simple dumbbell model is not possible to account for the much richer configuration space of real polymers, the compression effect can be explained at least qualitatively.

3.8. Comparison to experiments

Although there exist some experimental indications for the polymer compression at high shear rates [59], it was not yet observed in single molecule experiments. The compression of the polymers in shear flow only occurs at high shear rates. In the following, we give precise predictions for the shear rates at which this compression starts, using realistic polymer models for flexible as well as for semiflexible polymers.

From light scattering experiments on a polymer solution, a decrease in polymer extension for 800 nm long, flexible polymer chains was observed at shear rates of 500 s^{-1} [59]. The monomer radius of the used polymer is 2 nm, thus corresponding to a polymer chain with 200 beads. From the simulations described in section 3.4.1, a $N = 200$ flexible polymer is compressed by the shear flow for shear rates higher than $\dot{\tilde{\gamma}}^* \approx 0.13$. With the experimental viscosity of 0.1 Pas of the polymer solution, this yields an unscaled shear rate of 3×10^4 s^{-1}, thus much larger than the shear rate in the experiments. However, a semidilute polymer solution was used in the experiments in contrast to our single molecule simulations. Interactions between different polymer chains could explain this discrepancy.

Since many flow experiments use DNA molecules, we want to estimate the shear rate which is necessary to observe the compression for DNA. Because we are not able to simulate micrometer sized DNA chains with our polymer model, we will extrapolate the results obtained for shorter chains. Polymer chains with the parameters of 500 nm long DNA are found to be compressed at shear rates larger than $\dot{\tilde{\gamma}}^* \approx 0.01$ in section 3.5. With increasing length, the shear rate at the maximum polymer extension was found in section 3.4.2 to decay with increasing polymer length, $\dot{\tilde{\gamma}}^* \sim (L/a)^{-1.4}$. Thus, an unscaled shear rate $\dot{\gamma}^* \approx 50$ s^{-1} is obtained for 22 μm long DNA and a solvent viscosity of $\eta = 0.22$ Pas, the parameters of the experiments in Ref. [13]. This shear rate is roughly ten times larger than the shear rate used in these experiments. However, these flow strengths are easily achievable in shear flow experiments.

4. Shear-induced repulsion of a semiflexible polymer from a wall

In the previous chapter, polymer dynamics in unbounded shear flow is studied. This chapter studies the hydrodynamic effect of a no slip boundary on the polymer motion in shear flow. Due to the interplay of the flow field at the surface and the orientation induced by the shear flow, polymers are repelled from the interface.

For soft matter in external flows, hydrodynamic boundaries are of prime importance, partly because they are abundant in nano-fluidic devices, but also since surface effects hold potential for intelligent particle manipulation, segregation and modification. For a spherical particle in shear at a no–slip boundary, cross streamline migration occurs only for nonzero Reynolds numbers [72]. In contrast, repulsion from surfaces is possible even at zero Reynolds numbers for non-spherical or deformable particles, such as flexible polymers [73–76], fluid vesicles [68, 77, 78] or droplets [79]. For pressure-driven Poiseuille flow between two walls a diffusion-based mechanism gives rise to a force component towards the walls [73, 74], which however is irrelevant for the single-wall scenario studied in this chapter. Previous analytic studies were confined to simple dumbbell models or zero temperature, neglecting the coupling between conformational and hydrodynamic degrees of freedom, but numerical simulations provided ample evidence that hydrodynamic repulsion for deformable polymers persists even in the presence of thermal fluctuations.

In this chapter we extend an analytic theory for a simplified dumbbell model at a single no-slip surface [76, 79] to a stiff rod of finite length L. The dynamics of dumbbells and polymers in steady unbounded shear flow has been the subject of numerous analytical and numerical studies [50, 52, 55, 69, 80, 81]. It turns out that polymers preferentially align along the shear direction, but, due to Brownian motion, the orientation distribution function is asymmetric with respect to the direction of shear. Close to a no slip boundary the orientation distribution function is only slightly modified as long as steric effects are absent. In our approach, the hydrodynamic torques and lift forces are used on the Fokker-Planck level to calculate stationary and temperature dependent orientation distribution functions. We show that the asymmetric orientation distribution together with the hydrodynamic flow field leads to a non vanishing average lift force acting on the polymer. The generated lift force scales asymptotically as $L^{8/3}\dot{\gamma}^{2/3}T^{1/3}$ with shear rate $\dot{\gamma}$ and temperature T, thus demonstrating the importance of length effects, as confirmed by extensive hydrodynamic simulations for stiff rods. The lift force is long-ranged and decays inversely proportional with the square of the surface separation. Numerically, similar scaling is obtained for semiflexible polymers and even for flexible polymers at high enough shear rates.

4.1. Methods

In the hydrodynamic simulations, a polymer is composed of N spherical beads with radii a. In the zero Reynolds number limit and neglecting particle inertia, the time evolution of the coordinate of sphere i is given by the Langevin equation, eq. (2.18). The unperturbed fluid flow is a linear shear flow, $\mathbf{v}_0(\mathbf{r}) = \dot{\gamma}\mathbf{r}_z\hat{e}_x$.

Hydrodynamic effects are incorporated via the mobility matrix $\boldsymbol{\mu}_{ij}$ which is obtained from the Green's function of the Stokes equation that satisfies the no-slip condition on a planar boundary, eq. (2.9). The finite sphere radii are approximately taken into account via a multipole expansion to second order in terms of the bead radius a, eq. (2.13).

The potential between the beads

$$u(\{\mathbf{r}_N\}) = \frac{k_L}{2}\left[\left(\sum_{i=1}^{N}\frac{z_i}{N}\right) - Z\right]^2 + u_{LJ}(\{\mathbf{r}_N\}) + \sum_{i=1}^{N-1}\frac{\gamma}{4a^2}(|\mathbf{r}_i - \mathbf{r}_{i+1}| - 2a)^2 + \sum_{i=2}^{N-1}\frac{l_p}{2a}(1-\cos\vartheta_i) \quad (4.1)$$

renders an elastic polymer with the rescaled stretching modulus γ and a bending stiffness given by the persistence length l_p, where ϑ_i denotes the bending angle at sphere i. The bead connectivity is achieved by connecting subsequent beads with Fraenkel springs. A truncated repulsive Lennard Jones potential, eq. (3.1) with $\varepsilon = 1.2$ prevents sphere overlap. The harmonic potential of strength k_L constrains the center of mass of the polymer to a fixed distance from the wall close to Z and at the same time allows to determine the average lift force according to $\langle F_L\rangle = k_L\langle\sum_{i=1}^{N}(z_i/N) - Z\rangle/N$, very similar to a laser trap. We choose $k_L = 20/a^2$ for $N = 2$ and $k_L = 10/a^2$ otherwise. The planar boundary is impenetrable, i.e. sphere coordinates are restricted to $z_i > a$.

4.2. Dumbbell calculations

We first reconsider a dumbbell consisting of only two spheres at separation L. Its orientation is characterized by the angle θ with the surface normal and the in-plane angle ϕ, while Z denotes the distance of the center of mass from the surface, as depicted in Fig. 4.1a). The present formulation differs fundamentally from previous approaches [76, 79]; it brings out the intricate coupling between particle orientation and lift force in a clear fashion and allows for generalization to a finite-length rod. The deterministic sphere velocities of the dumbbell in shear flow follow from eq. (2.18) as

$$\mathbf{v}_1 = \boldsymbol{\mu}_{11}(\mathbf{F}_L + \mathbf{F}_s) + \boldsymbol{\mu}_{12}(\mathbf{F}_L - \mathbf{F}_s) + \dot{\gamma}z_1\hat{\boldsymbol{e}}_x \quad (4.2)$$

$$\mathbf{v}_2 = \boldsymbol{\mu}_{22}(\mathbf{F}_L - \mathbf{F}_s) + \boldsymbol{\mu}_{21}(\mathbf{F}_L + \mathbf{F}_s) + \dot{\gamma}z_2\hat{\boldsymbol{e}}_x \quad (4.3)$$

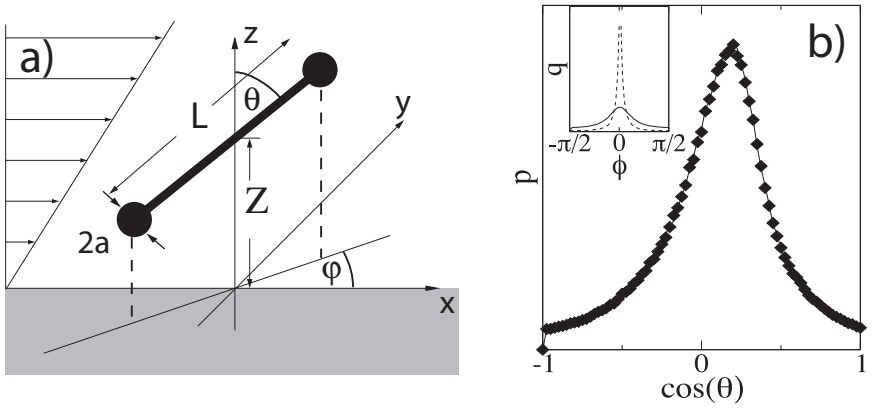

Figure 4.1.: a) Definition of the coordinate system and angles used for the dumbbell model. b) Angular distribution function $p(\theta)$ for a flexible polymer with $L/a = 20$ at shear rate $\dot{\tilde{\gamma}} = 1$ in bulk (symbols) and at surface separation $L/Z = 1$ (line). The inset shows the distribution $q(\phi)$ of the lateral angle ϕ in bulk for $\dot{\tilde{\gamma}} = 1$ (solid line) and $\dot{\tilde{\gamma}} = 100$ (dashed line).

The force $\mathbf{F}_s = F_s \hat{\boldsymbol{r}}$ acts along the connecting vector $\hat{\mathbf{r}}$ and keeps the sphere distance fixed. F_s is determined via the constraint $(\mathbf{v}_1 - \mathbf{v}_2) \cdot \hat{\mathbf{r}} = 0$ and reads to leading order

$$\frac{aF_s}{k_\mathrm{B}T} = -\frac{\dot{\tilde{\gamma}}}{2}\frac{L}{a}\cos\phi\cos\theta\sin\theta\left(1 + O\left[\left(\frac{L}{Z}\right)^3, \left(\frac{a}{L}\right)\right]\right), \tag{4.4}$$

with the rescaled shear rate, $\dot{\tilde{\gamma}} = \dot{\gamma}a^2/(k_\mathrm{B}T\mu_0)$.

The constraint force $\mathbf{F}_s$ leads to a disturbance of the linear shear profile and due to the no-slip boundary, flow field components in the direction of the shear gradient are generated. The lift force $\mathbf{F}_L = -F_L\hat{\mathbf{e}}_z$ acts equally on both beads and is determined by the requirement of fixed center-of-mass distance from the boundary, i.e. $(\mathbf{v}_1 + \mathbf{v}_2)\cdot\hat{\boldsymbol{e}}_z = 0$. From eqs. (4.2, 4.3) we obtain up to $\mathcal{O}\left[(L/Z)^3, (a/L)\right]$

$$\frac{aF_L(\phi,\theta)}{k_\mathrm{B}T} = \dot{\tilde{\gamma}}\frac{9L^2}{64Z^2}\cos\phi\sin\theta\cos\theta[1 - 3\cos^2\theta], \tag{4.5}$$

which corresponds to the lift of a stresslet at a distance Z above the surface [79]. Obviously, for isotropic dumbbell orientations, the average lift is zero. The lift force decays with the inverse square of the separation from the surface, as confirmed by experiments with deformable droplets [79]. From eqs. (4.2, 4.3), the hydrodynamic torques $M_\alpha = 6\pi\eta a(L/2)(\mathbf{v_1} - \mathbf{v_2}) \cdot \hat{\mathbf{e}}_\alpha$ with $\alpha = \phi, \theta$ and unit vectors $\hat{\mathbf{e}}_\theta = (\cos\phi\cos\theta,\ \sin\phi\cos\theta,\ -\sin\theta)$ and $\hat{\mathbf{e}}_\phi = (-\sin\phi,\ \cos\phi,\ 0)$, follow up to $O\left[(L/Z)^3\right]$ as

$$M_\theta(\phi,\theta)/(k_\mathrm{B}T) = (1/2)\dot{\tilde{\gamma}}\,(L/a)^2\cos\phi\cos^2\theta \tag{4.6}$$

$$M_\phi(\phi,\theta)/(k_\mathrm{B}T) = -(1/2)\dot{\tilde{\gamma}}\,(L/a)^2\sin\phi\cos\theta. \tag{4.7}$$

The torque M_θ is strictly positive, reflecting the shear-induced dumbbell rotation, while M_ϕ drives the lateral angle ϕ towards zero. To leading order, the hydrodynamic

torques do not depend on the wall distance Z. This insensitivity is confirmed by simulation data in Fig. 4.1b) by comparing the angular distribution function $p(\theta)$ in bulk and close to the surface (for $Z/L = 1$) for a flexible polymer with $N = 10$ and $l_p = 0$. In the inset we demonstrate that the angular distribution $q(\phi)$ is symmetric and peaked around $\phi = 0$ with a decreasing width for increasing shear rate $\dot{\tilde{\gamma}}$. To analytically calculate the azimuthal angle distribution $p(\theta)$, the full probability distribution function (PDF) is factorized as $\mathcal{P}(\theta, \phi) \approx p(\theta)q(\phi)$ and the lateral distribution function is approximated by a delta function, $q(\phi) = \delta(\phi)$. Separating rotational and translational motion, the distribution function $p(\theta)$ obeys the Fokker Planck equation

$$\partial_t p(\theta, t) = \mu_r \partial_\theta \left[-M_\theta(\theta) p(\theta, t) + k_\mathrm{B}T \, \partial_\theta p(\theta, t) \right]. \tag{4.8}$$

where μ_r denotes the rotational mobility. Defining the unit-less angular potential of mean force

$$\tilde{E}_\theta(\theta) = -\int_0^\theta d\theta' \frac{M_\theta(\phi = 0, \theta')}{k_\mathrm{B}T} = -(\dot{\tilde{\gamma}}/4)(L/a)^2(\theta + \cos\theta \sin\theta), \tag{4.9}$$

the stationary solution can be written as [82]

$$p(\theta) \propto \exp(-\tilde{E}_\theta(\theta)) \left(C - \int_0^\theta d\theta' \, \exp(\tilde{E}_\theta(\theta')) \right). \tag{4.10}$$

The constant C is chosen to fulfill the correct boundary condition $p(\theta) = p(\theta \pm \pi)$. In the limit of zero temperature, $p(\theta)$ is a delta function peaked at the marginally stable point $\theta = \pi/2$ where the acting torque is zero. With increasing temperature, the peak broadens and shifts. The position of the maximum θ^* follows from eq. (4.10) via $\partial_\theta p(\theta^*) = 0$ and for large $\dot{\tilde{\gamma}}$ reads [52, 69]

$$\Delta^* \propto \left[\dot{\tilde{\gamma}} (L/a)^2 \right]^{-1/3}, \tag{4.11}$$

with $\Delta = \pi/2 - \theta$. A Taylor expansion of eq. (4.10) around θ^* yields the inverse width $\left[\partial_\theta^2 p(\theta)\right]_{\theta=\theta^*} / p(\theta^*) \sim (\Delta^*)^{-2}$ [52, 69]. For increasing shear strength, the peak of the distribution function θ^* shifts closer to $\pi/2$ while the width decreases. The average lift follows by weighting the lift force eq. (4.5) with the normalized probability distribution $p(\theta)$ and integrating over dumbbell orientations

$$\frac{a\langle F_L \rangle}{k_\mathrm{B}T} = \int_0^\pi d\theta \, \sin(\theta) p(\theta) a F_L(\theta)/(k_\mathrm{B}T) \simeq (L/Z)^2 \, \dot{\tilde{\gamma}}^{2/3} \, (L/a)^{-2/3} \left[1 + O(\Delta^*) \right]. \tag{4.12}$$

The leading term is the lift force eq. (4.5) evaluated at the optimal angle $\theta^* = \pi/2 - \Delta^*$. To estimate the correction term, we used that the normalized probability distribution function $p(\theta)$ can be expressed in terms of a scaling function normalized as $\int dx g(x) = 1$ and satisfying $g(0) = -g''(0) = 1$ and $g'(0) = 0$. Using the scaling form $p(\Delta) = g(\Delta/\Delta^* - 1)/\Delta^*$, and assuming the second moment of $g(x)$ to exist, the integrand in eq. (4.12) can be straightforwardly expanded in powers of Δ^*. Remarkably,

the average lift force is long-ranged and decreases quadratically with inverse separation from the wall, similar to the zero-temperature result for vesicles in shear flow [68, 77]. Restoring unrescaled parameters, the scaling $\langle F_L \rangle \sim \dot{\gamma}^{2/3} a^{5/3} L^{4/3} T^{1/3} / Z^2$ is identical to the case of a FENE dumbbell at high shear rates [76], which clearly demonstrates the nontrivial coupling of temperature and hydrodynamic shear: at zero temperature the mean lift force vanishes.

4.3. Lift force for a rigid rod

Using our approach based on the angular potential of mean force $\tilde{E}_\theta$, these results for the dumbbell model can be straightforwardly generalized to a stiff cylinder of length L that is composed of $N = L/(2a)$ beads. Summing over all bead pairs with distance $L_{ij} = 2a(i-j)$ yields to leading order in a/L and L/Z the lift force per bead

$$F_L^{rod}(\phi, \theta) = \sum_{i,j;\, i<j} F_L(\theta, \phi, L_{ij})/N \simeq F_L(\theta, \phi)(L/a) \tag{4.13}$$

and the torque generating angular potential

$$\tilde{E}_\theta^{rod}(\theta) = \sum_{i,j;\, i<j} \tilde{E}_\theta(\theta, L_{ij}) \simeq (L/a)^2 \tilde{E}_\theta(\theta). \tag{4.14}$$

Applying the same asymptotic analysis of the Fokker-Planck equation that leads to eqs.(4.11) and (4.12), we obtain

$$\Delta_{rod}^* \propto [\dot{\tilde{\gamma}}(L/a)^4]^{-1/3} \tag{4.15}$$

in agreement with recent results for a semiflexible chain in bulk [81]. The average lift acting on the whole rod is up to corrections of order $\mathcal{O}(\Delta^*)$

$$\frac{L\langle F_L^{rod} \rangle}{k_B T} \simeq c_L \left(\frac{L}{Z}\right)^2 \left(\frac{L}{a}\right)^{2/3} \dot{\tilde{\gamma}}^{2/3} \tag{4.16}$$

with a numerically determined prefactor $c_L \simeq 10^{-2}$. In unrescaled units the lift force on the rod reads $L\langle F_L^{rod} \rangle \sim \dot{\gamma}^{2/3} a^{4/3} L^{8/3} T^{1/3} / Z^2$ and thus exhibits a distinctively different dependence on the length L when compared to the dumbbell results.

4.4. Simulation results

To test the predictions eqs. (4.12, 4.16), hydrodynamic simulations are performed for dumbbells as well as for polymers of varying stiffness in linear shear flow at a no-slip surface. For the dumbbell, two beads with radii a at an equilibrium distance L are used, polymers are modeled by N connected beads giving a length of $L = 2aN$. The rescaled stretching modulus, if not explicitly given, is $\gamma = 8000$ and keeps contour length fluctuations at a negligible level. The inverse quadratic decay of the average lift force with increasing separation Z from the wall is confirmed by the simulations

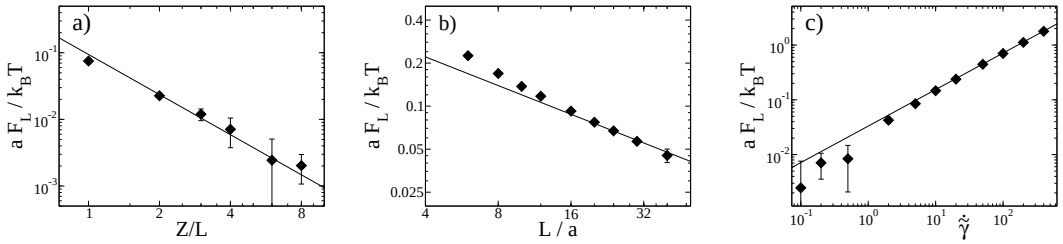

Figure 4.2.: Average lift for a dumbbell in linear shear flow. The symbols correspond to the simulation data, the solid lines show the predicted scaling from eq. (4.12) with adjusted prefactor. a) shows the dependence on surface separation Z (for fixed $L/a = 6$, $\tilde{\dot{\gamma}} = 10$, $\gamma = 1.6 \cdot 10^3$), (b) the dependence on the dumbbell length L (for fixed $L/Z = 1$, $\tilde{\dot{\gamma}} = 50$, $\gamma = 1.6 \cdot 10^4$) and (c) the dependence on shear strength $\tilde{\dot{\gamma}}$ (fixed $Z/L = 1$, $L/a = 6$, $\gamma/\tilde{\dot{\gamma}} = 1.6 \cdot 10^3$).

for dumbbells and for finite-length polymers in Figs. 4.2a) and 4.3a), respectively. The Z-scaling is identical for stiff rods, semiflexible as well as flexible polymers. This can be traced back to the fact that the orientation distribution function is to a very good approximation independent of Z and thus the prefactor of the lift force eq. (4.5) is the only place where the surface separation Z enters.

For dumbbells, the lift force decreases at constant L/Z and constant shear rate $\tilde{\dot{\gamma}}$ for varying bead separation L with the predicted $L^{-2/3}$ power law, as shown in Fig. 4.2b). For finite-length stiff rods, in contrast, the lift force increases with increasing length and confirms the scaling eq. (4.16) with $L^{2/3}$ at constant L/Z , see Fig. 4.3b) (filled squares). To prevent rod bending in the simulations, the persistence length has been chosen proportional to the monomer number, $l_p/L \sim N$. Since flexible polymers become less extended with increasing monomer number N at constant shear rate, the scaling prediction in eq. (4.16) is not expected to be valid. Indeed, the lift force for flexible polymers, open circles in Fig. 4.3b), does not increase significantly with monomer number N. Semiflexible polymers with $l_p/L = 1$ show a somewhat intermediate behavior (filled triangles in Fig. 4.3b).

With increasing shear rate $\dot{\gamma}$ the predicted behavior $\langle F_L \rangle \sim \dot{\gamma}^{2/3}$ is confirmed in fig 4.2c) for a dumbbell and in fig 4.3c) for a polymer consisting of $N = 10$ beads. To suppress chain stretching and bending at high shear rates $\dot{\gamma}$, the stretching and bending moduli constants are for the data in Figs. 4.2c) and 4.3c) chosen as $\gamma \sim \tilde{\dot{\gamma}}$ and $l_p/L \sim \tilde{\dot{\gamma}}$. Although the scaling dependence of the lift force on $\tilde{\dot{\gamma}}$ is derived for stiff rods, it is also obeyed quite accurately by semiflexible ($l_p/L = 1$) and even flexible ($l_p = 0$) polymers, see Fig. 4.3c). This can be traced back to an unfolding of flexible chains at elevated shear flows, rendering similar configurations for flexible and stiff polymers. To back up this idea, Fig. 4.4 shows the distribution of the normalized end to end distance R/L for flexible and semiflexible polymers with different lengths. For flexible chains, the fully stretched state is highly probable, but the population of the highly stretched state becomes less significant as the length increases at constant shear rate (see inset). This explains deviations from the rod scaling for very long flexible

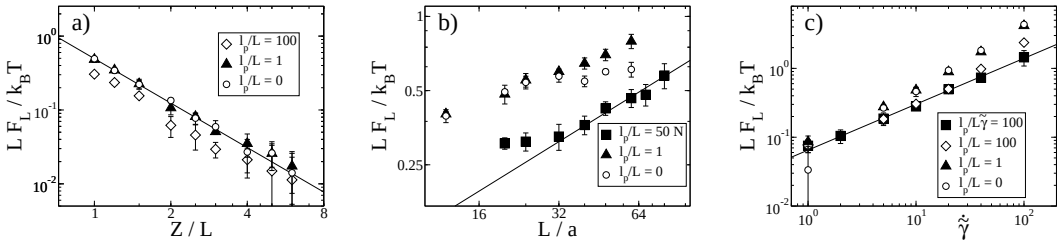

Figure 4.3.: Average lift force for polymers obtained from simulations (symbols), compared with the scaling predictions from eq. (4.16) denoted by solid lines. (a) shows the dependence on the surface separation Z for polymers of different bending stiffness (for fixed $\dot{\tilde{\gamma}} = 10$, $L/(2a) = N = 10$, $\gamma = 8000$), (b) shows the length dependence of the lift at $Z/L = 1$ and $\dot{\tilde{\gamma}} = 10$. For the simulation of stiff rods, the persistence length was adjusted like $l_p/L = 50N$ to prevent chain bending for longer rods. (c) shows the lift force for increasing shear strength $\dot{\tilde{\gamma}}$ (for fixed $L/(2a) = N = 10$, $\gamma = 8000$, $L/Z = 1$). The squares show data where bending and stretching is prevented by choosing a persistence length $l_p/(\dot{L\tilde{\gamma}}) = 100$ and stretching modulus $\gamma/(\dot{\tilde{\gamma}}) = 8000$, and follow the predicted scaling $\propto \dot{\tilde{\gamma}}^{2/3}$ most accurately.

chains observed in Fig. 4.3b). Semiflexible chains with $l_p/L = 1$ are predominantly in a stretched configuration but also show increased bending with increasing chain length, see Fig. 4.4. Due to the predominance of stretched configurations for semiflexibe and flexible polymers, the angular distribution functions, Fig. 4.5 are quite similar to those of rigid polymers.

Our analysis of the lift force, leading to eq. (4.16), does not include conformational changes of the polymer. Since semiflexible and flexible polymers undergo large shape variations during the flipping process, deviations from eq. (4.16) are expected. Nevertheless, some general conclusions can be drawn from the simulations results. As seen in Figs. 4.3b) and c), more flexible polymers exhibit consistently higher repulsions. At these high shear rates, flexible polymers are predominantly in a fully extended configuration at orientation $\theta^* = \pi/2 - \Delta^*$, similar to rigid polymers. During a chain flip, the chain is compressed at orientations $\theta \gtrsim \pi/2$ for which the lift force is attractive, and fully stretched for orientations $\theta \lesssim \pi/2$ for which the lift force is repulsive. Since the lift force increases with extension, see eq. (4.13), the net effect will be an enhancement of repulsion for flexible polymers. Along the same lines, our simulations suggest that flexible chains show higher flipping frequency compared to stiff polymers.

4.5. Discussion and conclusion

The hydrodynamic repulsion of polymers in shear flow at low Reynolds number considered here leads to a drift away from the wall and thus to the formation of a depletion layer close to the wall, in agreement with previous simulations [73, 75, 76]. This hydrodynamic repulsion of polymers thus competes with bare surface-polymer

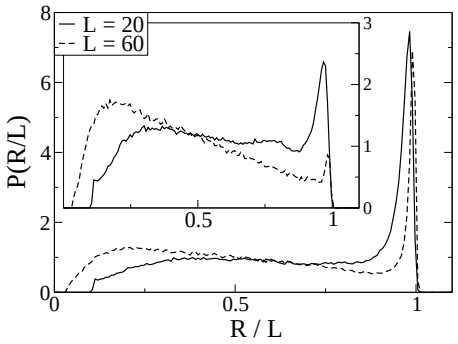

Figure 4.4.: Normalized histogram of the length of the end to end vector for semiflexible ($l_p/L = 1$) and flexible polymers (inset) with different contour lengths $L = 2Na$ at $\dot{\tilde{\gamma}} = 10$ and $L/Z = 1$.

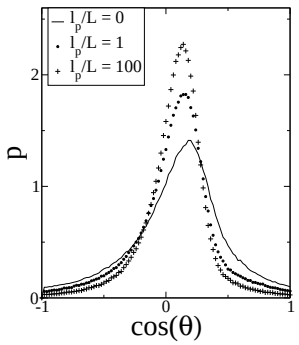

Figure 4.5.: Normalized orientation distribution function $p(\theta)$ for polymers of length $L/(2a) = N = 10$ in bulk for different persistence lengths at fixed shear rate $\dot{\tilde{\gamma}} = 1$.

interactions and in principle can trigger a shear-induced desorption transition. Since the lift force decays inverse quadratically with distance, the corresponding potential of mean force decays inversely with separation and thus like unscreened electrostatic interactions. According to the theory of polymer adsorption [83], such a long-ranged repulsive potential will turn any adsorption transition into a discontinuous one.

Let us finally estimate the shear strength needed to achieve a noticeable polymer depletion. The repulsive potential of mean force E_{des} for the entire rod is obtained from the hydrodynamic force by integration from bulk to a distance $Z = L/2$ where steric wall-rod interactions come into play,

$$E_{des} \approx -\int_{\infty}^{L/2} dZ \, \langle F_L^{rod}(Z)\rangle (L/2a), \tag{4.17}$$

and is in the following compared to thermal energy, $k_{\mathrm{B}}T$. Using eq. (4.16), the critical shear rate at which $E_{des} \simeq k_{\mathrm{B}}T$ turns out to be

$$\dot{\gamma}^*_{des} = k_{\mathrm{B}}T/(6\pi\eta) c_L^{-3/2} (L/a)^{1/2} L^{-3}. \tag{4.18}$$

A typical example for a nanorod is the tobacco mosaic virus with length $L = 300$ nm and radius $a = 9$ nm. Inserting the viscosity of water at room temperature, $\eta = 10^{-3}$ Pas, and the prefactor $c_L \simeq 10^{-2}$ as extracted from simulations in Fig. 4.3b), we find $\dot{\gamma}^*_{des} \simeq 5 \cdot 10^4$ s^{-1} which corresponds to a high but not unreachable shear rate. For longer polymers the critical shear rate will be further reduced. The corresponding Reynolds number is $Re = L^2 \rho \dot{\gamma}/\eta \simeq 5 \cdot 10^{-3}$, where the water density is $\rho \simeq 10^3$ kg/m^3, and thus turns out to be still small, justifying our use of the Stokes equation.

For flexible polymers the Weissenberg number Wi, which is the product of the shear rate and the relaxation time, $Wi \sim \dot{\gamma}\tau$, is given by $Wi \sim \dot{\gamma}\eta R^3/(k_{\mathrm{B}}T)$, where $R \sim l_p (L/l_p)^{\nu}$ is the scaling prediction for the radius of a polymer chain satisfying

$L \gg l_p$[84]. Chain stretching sets in when $Wi \sim 1$ [49], giving a critical shear rate for chain stretching of

$$\dot{\gamma}^*_{stretch} \sim \frac{k_\mathrm{B}T}{\eta R^3} \sim \frac{k_\mathrm{B}T}{\eta l_p^3 (L/l_p)^{3\nu}}. \tag{4.19}$$

Above that shear rate, the chain exhibits stretched configurations. In the case $\dot{\gamma}^*_{stretch} > \dot{\gamma}^*_{des}$ the desorption criterion $E_{des} > k_\mathrm{B}T$ should be satisfied at the stretching threshold $\dot{\gamma}^*_{stretch}$. With eqs. (4.18, 4.19), this leads to the condition

$$l_p/a \lesssim (L/l_p)^{5-6\nu}. \tag{4.20}$$

Since $\nu \approx 3/5$ this expression is always fulfilled for polymers much longer than their persistence length, $L \gg l_p$, i.e. in the flexible limit. The inequality $\dot{\gamma}^*_{stretch} > \dot{\gamma}^*_{des}$ implies that as soon as flexible polymers are stretched by the shear flow, the lift force will lead to a depletion layer at the boundary, in good agreement with numerical observations [73–76].

5. Hydrodynamic lift of a moving nano-rod at a wall

The situation where a body is pulled laterally over a substrate by an external force is experimentally relevant for sedimentation and surface-based electrophoresis [85]. Similarly to the shear-flow case, a lift force is obtained for a sphere only if one includes inertia or non-Newtonian effects [86]. In this chapter we consider a cylinder or rod-like object that is pulled by an external force parallel to a wall and subject to thermal noise at zero Reynolds number. As was shown long time ago, the no-slip wall induces a torque [87–89], which in conjunction with the known anisotropic hydrodynamic mobility tensor of a cylinder [38] leads to a repulsion away from the wall. We extend these results to the finite-temperature case by constructing from the hydrodynamic torque the orientational distribution function from which thermally averaged lift forces are derived. Our analytical results (confirmed by extensive hydrodynamic simulations for dumbbells as well as bead-spring-like stiff polymers) show that in the high-temperature limit the lift force is i) long-ranged and decays as the inverse square of the wall-cylinder distance and ii) proportional to the square of the driving force. Our high-temperature lift-mechanism is relevant for stiff polymers close to surfaces that are subject to gravitational forces or electric fields at low enough salt concentrations so that screening can be neglected [85]; in fact, for weakly adsorbed rods a hydrodynamically driven desorption transition is predicted.

In our hydrodynamic simulation, the rod is composed of N spherical beads of radii a. The velocity of the i th bead is determined by the position Langevin equation in eq. (2.18) with zero external flow $\mathbf{v}_0 \equiv 0$

$$\dot{\mathbf{r}}_i(t) = \sum_{j=1}^{N} \boldsymbol{\mu}_{ij} \left[-\boldsymbol{\nabla}_{r_j} U(\{\mathbf{r}_k\}) + F\hat{\mathbf{e}}_x \right] + \sum_j \boldsymbol{\nabla}_{r_j} \boldsymbol{\mu}_{ij} k_\mathrm{B} T + \boldsymbol{\xi}_i(t). \tag{5.1}$$

Hydrodynamic interactions between beads and the no-slip boundary condition on the surface are taken into account on the Stokes-level (i.e. for zero-Reynolds number) via the mobility tensor $\boldsymbol{\mu}_{ij}$ in the same way as in the preceding chapter. The interaction between beads is determined by the potential U in eq. (4.1). For the dumbbell simulations ($N = 2$) we choose $\gamma = 1600$, otherwise $\gamma = 8000$, which keeps contour-length fluctuations at a negligible level of less than 5 %. A harmonic spring with stiffness k_L constrains the rod center of mass to an average distance close to Z from the surface. This allows us to extract the distant-dependent average of the lift-force per monomer, F_L, in a numerically simple and efficient way. We choose $k_L = 20/a^2$ for $N = 2$ and $k_L = 10/a^2$ otherwise. The no-slip surface is modeled as infinitely repulsive for the bead centers, i.e. $z_i > a$ is enforced by bead reflection. The external force F acts parallel to the surface on all beads and represents the dissipative action of a gravitational

or electric field. The simulation time of up to $3 \cdot 10^9$ iteration steps was always much longer than the rod orientational relaxation time. We explicitly checked for sufficient equilibration by starting simulations with different initial conditions. Error bars were determined by block averaging.

An intuitive explanation for the wall-induced rod orientation follows from inspection of Blake's Green's function $\mathbf{G}^W$. Fig. 5.1a) shows fluid streamlines for a point force acting parallel to the no-slip surface. As can be seen, the normal component of the fluid velocity points *away from the wall* in front of the force locus, behind the point force the fluid is moving *towards the wall*, which follows from the necessity to have flow stagnation at the surface. Since the Stokes equation is linear, the fluid flow profile around a cylindrical object can be constructed by adding several so-called Stokeslets as shown in Fig. 5.1a). The net effect is a torque, acting to move the leading front of the cylinder away and the trailing part towards the surface [87–89], see also Fig. 2.1f). As shown below, in the stable configuration the moving rod makes a finite angle with the surface, and due to the pronounced mobility anisotropy of any elongated object a finite lift force perpendicular to the surface (and thus to the pulling direction) results.

5.1. Scaling theory for dumbbell

We first consider a simplified dumbbell geometry consisting of 2 beads that are subject to an external lateral force $\mathbf{F} = F\hat{\mathbf{e}}_x$ each, see Fig. 5.1b). The beads are fixed at a mutual distance L, which is enforced by a spring force $\mathbf{F}_s$ that acts along the connecting vector $\hat{\boldsymbol{r}}$. The lift force $\mathbf{F_L} = -F_L\hat{\boldsymbol{e}}_z$ holds the center of mass fixed at height Z above the interface located in the $x-y$-plane at $z = 0$, in the same way as described in the previous chapter. The velocities of the two beads are calculated from the product of the mobility matrix $\boldsymbol{\mu}_{ij}$ as defined in eq. (2.13) and all forces,

$$\mathbf{v}_1 = \boldsymbol{\mu}_{11}(\mathbf{F} + \mathbf{F}_s + \mathbf{F}_L) + \boldsymbol{\mu}_{12}(\mathbf{F} - \mathbf{F}_s + \mathbf{F}_L) \tag{5.2}$$

$$\mathbf{v}_2 = \boldsymbol{\mu}_{22}(\mathbf{F} - \mathbf{F}_s + \mathbf{F}_L) + \boldsymbol{\mu}_{21}(\mathbf{F} + \mathbf{F}_s + \mathbf{F}_L) \tag{5.3}$$

where $i, j = 1, 2$ and $i \neq j$. The equations that fix the constraining force magnitudes F_s and F_L are given by

$$(\mathbf{v}_1 - \mathbf{v}_2)\hat{\boldsymbol{r}} = 0 \tag{5.4}$$

$$(\mathbf{v}_1 + \mathbf{v}_2)\hat{\boldsymbol{e}}_z = 0. \tag{5.5}$$

By perturbatively solving these equations, the lift force follows for arbitrary dumbbell orientation for large separation, $Z \gg L$, and slender rods, $a \ll L$,

$$\frac{F_L}{F} = \frac{3a}{8L}\cos(\phi)\sin(2\theta) + \mathcal{O}\left(\left(\frac{a}{L}\right)^2, \frac{L}{Z}\right), \tag{5.6}$$

where θ denotes the angle of $\hat{\boldsymbol{r}}$ with the surface normal, ϕ the angle of $\hat{\boldsymbol{r}}$ in the $x-y$ – plane with the external force direction and Z the distance of the center of mass from the surface, see Fig. 5.1b. Eq. (5.6) corresponds to the lift on a

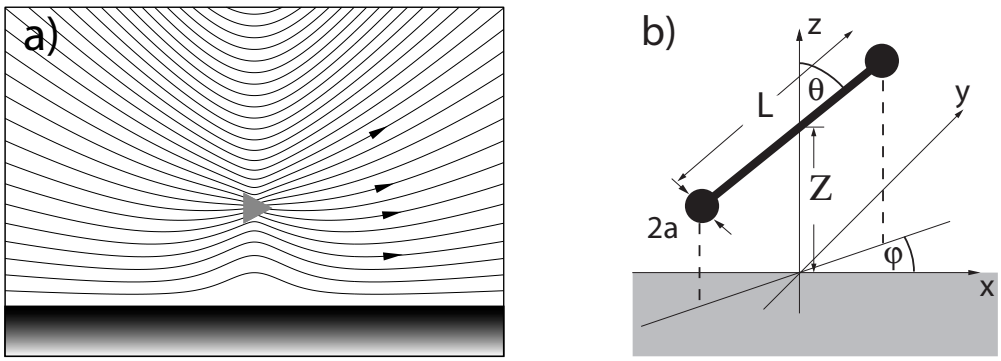

Figure 5.1.: a) Streamlines for a point force (Stokeslet) in the $x-z$ plane. The position of the point force, pointing to the right, is indicated by the triangle. The arrows denote the direction of the flow. b) Sketch of the coordinate system and of the dumbbell model.

slanted dumbbell in bulk, effects due to the no-slip surface only contribute in next-leading order and are neglected in our scaling considerations. The angular velocities perpendicular to $\hat{\boldsymbol{r}}$ are defined as $v_\theta = (\mathbf{v}_1 - \mathbf{v}_2)\hat{\boldsymbol{e}}_\theta$ and $v_\phi = (\mathbf{v}_1 - \mathbf{v}_2)\hat{\boldsymbol{e}}_\phi$ with $\hat{\boldsymbol{e}}_\theta = (\cos(\phi)\cos(\theta), \sin(\phi)\cos(\theta), -\sin(\theta))$ and $\hat{\boldsymbol{e}}_\phi = (-\sin(\phi), \cos(\phi), 0)$. The torques are defined as $M_{\alpha\,(\alpha=\phi,\theta)} = L/2 \cdot 6\pi\eta a v_\alpha$ and follow for $a/L \ll 1$ and $L/Z \ll 1$ to leading order as [87]

$$\frac{M_\theta}{aF} = \frac{9}{32}\left(\frac{L}{Z}\right)^2 \cos(\phi)\cos(2\theta) \tag{5.7}$$

$$\frac{M_\phi}{aF} = -\frac{9}{32}\left(\frac{L}{Z}\right)^2 \sin(\phi)\cos(\theta). \tag{5.8}$$

At the equilibrium orientation, defined by vanishing torques $M_\theta = M_\phi = 0$, the rod makes an angle of $\pi/4$ with the surface, i.e. $\theta^* = \pi/4$ and $\phi^* = 0$ (valid for large separation from the surface). For the treatment of thermal effects, we define a generating functional E via the relations $\mathbf{M}(\phi,\theta) = -\mathbf{r} \times \boldsymbol{\nabla} E(\phi,\theta)$, or, explicitly $\mathbf{M}_\theta = -\hat{\boldsymbol{e}}_\phi\, \partial_\theta E(\phi,\theta)$ and $\mathbf{M}_\phi = -\hat{\boldsymbol{e}}_\theta (1/\sin(\theta))\, \partial_\phi E(\phi,\theta)$. This functional, which can be interpreted as a non-equilibrium version of the orientation free energy, can be written in closed-form as

$$\frac{E(\theta,\phi)}{aF} = -\frac{9}{32}\left(\frac{L}{Z}\right)^2 \cos(\phi)\cos(\theta)\sin(\theta). \tag{5.9}$$

Factorizing the Langevin equation into the dissipative translational motion along the external force direction and the slaved orientational relaxation, the dumbbell orientation probability $P(\phi,\theta)$ can be shown to obey a Boltzmann distribution at finite temperature, i.e. $P(\phi,\theta) = \mathcal{Z}^{-1}\exp(-E(\phi,\theta)/k_\mathrm{B}T)$, where the partition function $\mathcal{Z}$ ensures correct normalization [90]. In the asymptotic zero-temperature limit, i.e. at strong torques, $aF(L/Z)^2 \gg k_\mathrm{B}T$, the probability distribution approaches a delta distribution centered at the stable rod orientation; the average lift force scales linearly

with the pulling field F, is independent of temperature, and reads for $a/L \ll 1$ and $L/Z \ll 1$,

$$\langle F_L \rangle = \int_{-\pi/2}^{\pi/2} d\phi \int_0^{\pi} d\theta \sin(\theta)\ F_L P(\phi,\theta) \simeq F_L(\phi = 0, \theta = \theta^*) \simeq \frac{3aF}{8L}, \tag{5.10}$$

where eq. (5.6) was used. In the high temperature limit, i.e. $aF(L/Z)^2 \ll k_\mathrm{B}T$, we approximate $P(\phi,\theta) \simeq \frac{1}{2\pi}(1 - \beta E(\phi,\theta))$. Using eq. (5.9) and eq. (5.6), the resulting lift now is second order in F and decays inversely with the square of the distance from the surface,

$$\begin{aligned} \langle F_L \rangle &\simeq \frac{1}{2\pi} \int_{-\pi/2}^{\pi/2} d\phi \int_0^{\pi} d\theta \sin(\theta)\ F_L(1 - \beta E(\phi,\theta)) \\ &\simeq \frac{9}{640} \frac{a}{L} \left(\frac{L}{Z}\right)^2 \frac{aF^2}{k_\mathrm{B}T}. \end{aligned} \tag{5.11}$$

5.2. Simulation of dumbbell model

To directly check eq. (5.11) for a numerically inexpensive case, we perform hydrodynamic simulations of a dumbbell consisting of two beads ($N = 2$) connected by a spring. In Figs. 5.2a) - c) we separately compare the dependence of the lift force $\langle F_L \rangle$ on the separation between the beads, L, the mean height from the surface Z, and the pulling force F in the high-T limit. The predictions of eq. (5.11) are shown as a solid line and the simulation results as points, and the excellent agreement demonstrates the accuracy of the scaling theory including the numerical prefactor.

Although the Stokes equation is linear, the mean lift force $\langle F_L \rangle$ shows a quadratic dependence on the pulling force F in the high-T limit, see Fig. 5.2c); this is due to the interplay of hydrodynamic and thermal orientation effects. At high fields, on the other hand, the lift force is expected to scale linearly with F, see eq. (5.10). Equating eqs. (5.10) and (5.11) suggests the crossover to occur at $aF/k_\mathrm{B}T \simeq 27(Z/L)^2$. Fully consistent with this estimate, Fig. 5.2c) indicates that the high-T result breaks down for pulling forces $aF/k_\mathrm{B}T > 25$ for a distance $Z/L = 1$.

5.3. Finite-length rod

We now consider a cylinder composed of N beads and length $L = 2Na$. Due to different mobilities $\mu_\parallel$ and $\mu_\perp$ for cylinder motion parallel and perpendicular to its axis, respectively, the cylinder velocity is not parallel to the pulling force unless the force acts perpendicular or parallel to the cylinder axis. In bulk and thus neglecting effects due to the wall (which contribute only to next-leading order in L/Z), the lift force F_L is obtained by decomposing the pulling force F into contributions parallel and perpendicular to the cylinder axis [5],

$$\frac{F_L}{F} = \frac{\sin(2\theta)\cos(\phi)\left(\mu_\parallel/\mu_\perp - 1\right)}{2\left[1 + \cos^2(\theta)\left(\mu_\parallel/\mu_\perp - 1\right)\right]}, \tag{5.12}$$

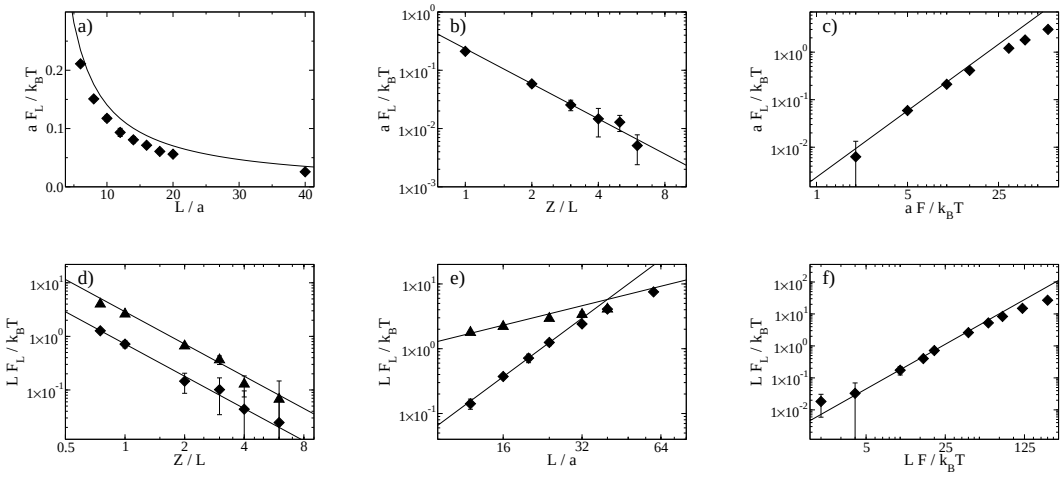

Figure 5.2.: High-temperature simulation results (data points) for (a-c) the average lift force F_L for a dumbbell compared with the scaling prediction eq. (5.11) (lines), and (d-f) the average total lift LF_L for a cylinder with $l_p/L = 100$ compared to eq. (5.14) with an adjusted prefactor $c_L = 0.9 \cdot 10^{-4}$ (lines). a) Dependence on the dumbbell length L at a pulling force of $aF = 10\ k_\mathrm{B}T$ and $Z/L = 1$. b) Dependence on the wall distance Z at $aF = 10\ k_\mathrm{B}T$ and $L/a = 6$. c) Dependence on the pulling force F at fixed $L/a = 6$ and $Z/L = 1$. d) Data for a cylinder with $L/a = 20$ at $aF = 1\ k_\mathrm{B}T$ (♦) and $aF = 2\ k_\mathrm{B}T$ (▲) at varying distances Z from the wall. e) Data for different length L (with $N = L/(2a)$) for fixed total force $LF = 40\ k_\mathrm{B}T$ (▲) and for a constant pulling force per bead, $aF = 1\ k_\mathrm{B}T$ (♦), $Z/L = 1$. f) Data for $L/a = 20$ at $Z/L = 1$ for varying pulling force F.

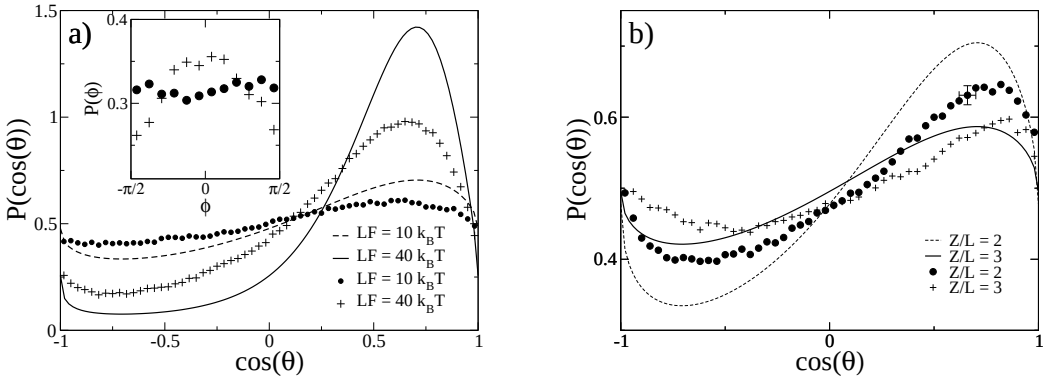

Figure 5.3.: Angular probability distribution functions for a rod with $L/a = 20$ and persistence length $l_p/L = 100$ from simulations (symbols) compared to the theoretical prediction $P(\cos(\theta), \phi) = \mathcal{Z}^{-1} \exp[-E(\cos(\theta), \phi)/(k_\mathrm{B}T)]$ (lines) with the orientation generating functional from eq. (5.13). Fig. a) shows the PDFs for external fields $LF = 10\ k_\mathrm{B}T$ and $LF = 40\ k_\mathrm{B}T$ at $Z/L = 1$. In Fig. b) the PDF for $\cos(\theta)$ is plotted for an external field of $LF = 40\ k_\mathrm{B}T$ at $Z/L = 2$ and $Z/L = 3$. The numerical error is shown for one data point in b).

and vanishes for an isotropic object with $\mu_\parallel/\mu_\perp = 1$. Eq. (5.12) is the continuum version for a finite-length cylinder of the dumbbell result in eq. (5.6). We calculate the torque acting on the cylinder by factorization into N beads. Each pair of beads makes a contribution E_{ij} to the total orientation generating functional, which follows from eq. (5.9) by inserting the bead separation $L_{ij} = |\mathbf{r}_i - \mathbf{r}_j|$ for the length of the dumbbell. The total torque generating functional E follows by summing over all pairs (i, j) in the limit $L/Z \ll 1$ and $N \gg 1$ as

$$E = \sum_{i=1}^{N} \sum_{j<i}^{N} E_{ij} = -\frac{3}{512} \cos(\phi) \cos(\theta) \sin(\theta) \left(\frac{L}{Z}\right)^2 \frac{L}{a} LF \left[1 + \mathcal{O}\left(\frac{a}{L}, \frac{L}{Z}\right)\right] \quad (5.13)$$

where Z denotes the center of mass distance of the rod from the surface. Applying the high temperature approximation as in eq. (5.11) and using $\mu_\parallel/\mu_\perp = 2$ [5] in eq. (5.12), the lift force per monomer follows as

$$\langle F_L \rangle \simeq c_L (L/Z)^2 L^2 F^2/(a k_\mathrm{B}T) \quad (5.14)$$

with the prefactor $c_L = (10 - 3\pi)/2048 \simeq 2.8 \cdot 10^{-4}$. The low-T result, valid for $L^2(L/Z)^2 F/a \gg k_\mathrm{B}T$, is simply $\langle F_L \rangle \simeq F/3$. In the hydrodynamic simulations the rod is modeled as N connected spheres with a persistence length l_p that is 100 times larger than the contour length L. The simulation data are compared in Figs. 5.2d)-f) with the scaling prediction eq. (5.14) shown as solid lines, where the numerical prefactor of the scaling law is determined to be $c_L = 0.9 \cdot 10^{-4}$ and thus differs by a factor of about 3 from the analytic result. The deviation can be attributed to the neglect of the no-slip boundary condition on the rod in the scaling argument, which

is approximatively taken into account in the numerics via self-consistent solution of the force-velocity matrix using a multipole expansion, and to higher-order corrections for finite L/Z, N and a/L. Fig. 5.2d) shows the Z-dependence of the lift force for a cylinder with $N = 10$ beads, confirming the quadratic decay with the inverse distance from the interface, consistent with eq. (5.14). According to eq. (5.14), the total lift force LF_L for constant total pulling force LF and fixed L/Z should increase linearly with the cylinder length L, as indeed seen in 5.2e). As a consequence, if the pulling force per monomer, F, is independent of the cylinder length L, corresponding to a gravitational or electric force, the total lift force LF_L scales as L^5 at fixed wall separation Z. Fig. 5.2f) confirms the quadratic dependence of the lift force F_L on the pulling force F for constant length L and wall separation Z. For higher pulling forces F or longer rods, the average lift deviates from the scaling result because i) the high temperature approximation breaks down and ii) the rod becomes bent which invalidates the dumbbell model, as will be explained below.

At the heart of the mechanism for the hydrodynamic lift lies the partial cylinder orientation. In Fig. 5.3 we show the angular probability distribution function (PDF) as a function of the angle θ and (in the inset) ϕ. For increasing pulling force F or decreasing distance from the surface Z, the PDF becomes more anisotropic and a maximum around $\theta = \theta^* \simeq \pi/4$ and $\phi = \phi^* = 0$ builds up. The lines show the PDF as calculated from eq. (5.13) using the definition $P(\cos(\theta), \phi) = \mathcal{Z}^{-1} \exp[-E(\cos(\theta), \phi)/(k_\mathrm{B}T)]$ and predict the shape of the PDFs in a qualitative manner. Compared to $P(\theta)$, the PDF for ϕ is much closer to the isotropic case. This is due to the fact that the first correction in the high temperature limit to $P(\phi) = \mathcal{Z}^{-1} \int d\cos(\theta)\ \exp[-E(\cos(\theta), \phi)/(k_\mathrm{B}T)]$ from the isotropic case is only second order in $E/(k_\mathrm{B}T)$. Deviations of the simulation data from the predictions occur because the orientation generating functional E is only asymptotically exact in the limits $L/Z \to 0$ and $N \to \infty$, and the no-slip condition on the bead surface is omitted in the scaling arguments.

A different hydrodynamic orientation mechanism that does not depend on the presence of a no-slip wall and that competes with the scenario discussed up to now is obtained for flexible rods, which are bent into a horse-shoe shape and orient perpendicularly to the applied force [91]. For a perpendicular configuration, the lift force is drastically reduced. If rod bending with increasing external fields is prevented by increasing stiffness, the angular PDFs approach a delta function peaked at ϕ^*, θ^* in the limit of zero temperature. According to eq. (5.10), in this limit the lift force scales linearly with the external force, which is demonstrated in Fig. 5.4. For increasing driving field F, the PDFs indeed become more sharply peaked. In the simulations, the ratio l_p/F is held constant so that the rod bending is comparable for all field strengths.

5.4. Conclusion

In this chapter it is shown that a rod which is subject to thermal noise and driven by an external force laterally to a hydrodynamic no-slip boundary, experiences a repulsive lift away from the wall in the zero-Reynolds-number limit. The lift is caused by a

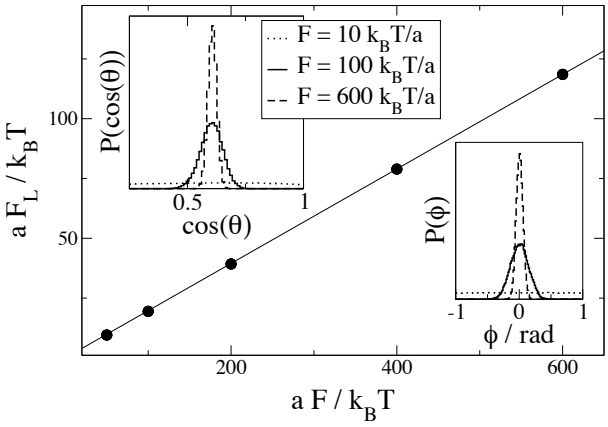

Figure 5.4.: Simulation results for a cylinder with $L/a = 20$ at fixed height $Z/L = 1$ in the low temperature limit. The average lift force scales linearly with the lateral pulling force, in qualitative accord with eq. (5.10). The insets show the angular PDFs at different field strengths. The persistence length of the rod is adjusted as $l_p/F = 50\ La/(k_\mathrm{B}T)$ to prevent bending.

hydrodynamic orientation of the rod. Scaling relations for the repulsion are derived in the high and low temperature limits, and are tested with extensive hydrodynamic simulations both for a simplified dumbbell model as well as for finite-length rods. In the low-T limit, valid for strong driving fields F or small separations Z from the surface, the repulsive force is constant. In the high-T limit, the repulsion is still long-ranged but decays quadratically with the distance from the surface. Therefore, the corresponding interaction potential decays inversely with the wall-separation like $1/Z$ as the Coulomb potential. Since Coulomb interactions are screened in aqueous solution, we conclude that the hydrodynamic lift is more long-ranged than any other direct interaction observable in nature. One consequence is that adsorption transitions are turned discontinuous even in the presence of minute lateral driving forces [83], as confirmed by recent hydrodynamic simulations of laterally driven polymers close to an adsorption transition [90]. Note that the resulting lift force F_L is independent of the solvent viscosity since the driving force F is used as the independent parameter.

In the following, we briefly compare the magnitude of the hydrodynamic repulsion with the typical adsorption strength of polymers at solid surfaces. The force needed to desorb a single polymer from a substrate can be conveniently measured by the atomic-force-microscope (AFM); for a surprisingly wide class of polymers and substrates, encompassing polycations and polyanions for varying salt concentrations and at charged, hydrophobic, or metallic substrates, the plateau force for desorption is found to be of the order of 50 pN [92, 93]. Assuming a monomer length of about 0.25 nm, this corresponds to an adsorption free energy of the order of 3 $k_\mathrm{B}T$ per monomer. We compare with the free energy obtained by an integral over the lift force in the high-T limit, eq. (5.14), with a prefactor of $c_L \approx 1 \times 10^{-4}$ obtained from the simulation

data, $E_{des} \approx -\int_{\infty}^{L/2} dZ \ \left[c_L (L/Z)^2 L^2 F^2/(a k_{\mathrm{B}} T)\right] \simeq 2 c_L (L/a)^3 k_{\mathrm{B}} T (Fa/k_{\mathrm{B}} T)^2$. The lower integration boundary $L/2$ reflects the minimal separation at which the rod is able to rotate without steric interactions with the wall, and the consistency of the high-T assumption will be checked below. Assuming a Kuhn polymer segment to consist of 5 monomers, realistic for typical synthetic polymers, we expect rod-like behavior up to a length of $L/a \simeq 10$. Furthermore assuming that each monomer bears one elementary charge and $a \simeq 0.25$ nm, the lift energy per monomer becomes of the order of thermal energy, $E_{des} \simeq k_{\mathrm{B}} T \simeq 25$ meV, for a lateral electric field of $F \simeq k_{\mathrm{B}} T/a \simeq 2 \cdot 10^8$ eV/m. Such large forces can be experimentally realized with electrodes at micrometer separations. Due to the cubic dependence of the lift-free energy E_{des} on the rod length L/a, the electric field needed for desorption drastically goes down with increasing L. For DNA with $L/a \simeq 100$ the electric field that gives $E_{des} \simeq k_{\mathrm{B}} T$ is only $F \simeq k_{\mathrm{B}} T/a \simeq 7 \cdot 10^6$ eV/m, and for more elongated rods even smaller driving fields are sufficient. Note that these simple estimates are strictly valid only for rods shorter than the ionic screening length, a complication that is absent for gravitational forces. Our usage of the high-T result for the calculation of the threshold $E_{des} \simeq k_{\mathrm{B}} T$ turns out to be valid for short enough rods as long as $L/a \lesssim 2000$ [90]. These findings indicate that the repulsive hydrodynamic lift can be used in nano-chip applications for inducing the desorption of for example DNA segments by applying lateral electric fields.

An interesting question concerns the crossover between the surface-induced rod orientation discussed in this chapter and the afore-mentioned rod-bending-induced hydrodynamic orientation which is operative already in the bulk and leads to a perpendicular orientation to the driving field [91] and thus weakens the lift force drastically. For quantitative comparison of the two competing effects, we derive the scaling form of the wall induced orientational order in the high temperature limit. The orientational order parameter Ψ_{wall} is defined with respect to the zero-temperature orientation of a driven rod, $\hat{\mathbf{r}}_0 = (\cos(\phi^*)\sin(\theta^*),\ \sin(\phi^*)\sin(\theta^*)\ ,\cos(\theta^*))$ with $(\phi^*, \theta^*) = (0, \pi/4)$ and reads

$$\Psi_{wall} = \frac{3}{2}\langle(\hat{\mathbf{r}}\hat{\mathbf{r}}_0)^2\rangle - \frac{1}{2} \tag{5.15}$$

where $\hat{\mathbf{r}}$ denotes the orientation unit vector of the rod. At infinitely high temperature or in the absence of a pulling force, one expects isotropic orientation with $\Psi_{wall} = 0$, while $\Psi_{wall} = 1$ is expected at zero temperature in the fully aligned state. Using a Boltzmann distribution with the orientational energy eq. (5.13), the high temperature scaling is to leading order

$$\Psi_{wall} = \frac{3}{5120}\left(\frac{L}{Z}\right)^2\left(\frac{L}{a}\right)^2\frac{aF}{k_{\mathrm{B}}T} + \mathcal{O}\left(\left(\frac{aF}{k_{\mathrm{B}}T}\right)^2\right) \tag{5.16}$$

and depends quadratically on the rod length at constant L/Z. In contrast, the orientational order parameter due to rod bending, denoted as Ψ_{bend} and defined with respect to the direction parallel to the pulling force, is $\Psi_{bend} \sim -(L/a)^4 (L/l_p)(aF/k_{\mathrm{B}}T)^2$ [91] and scales quartic with the rod length L at constant rescaled persistence length l_p/L.

Note also that the wall-induced orientation Ψ_{wall} is linear in the applied force F (while the resulting lift is quadratic), whereas the bending-induced orientation Ψ_{bend} is quadratic in F as it depends on hydrodynamic rod bending in the first place [91]. In conclusion, only for stiff filaments or short enough filaments is the lift scenario discussed in this chapter operative, otherwise hydrodynamic rod bending comes into play. For flexible polymers with a persistence length much smaller than the contour length, $l_p/L \ll 1$, preliminary simulation results suggest that some of the effects found in this chapter survive [90], but it is obvious that the scaling description is modified in a fundamental way.

6. Dynamics of end grafted DNA molecules and possible biosensor applications

Microfluidic devices [8, 9] are becoming indispensable tools in chemistry, biology and medicine. Much effort is put into the development of so called labs-on-a-chip, which promise fast and parallel realization of a large variety of different experiments. The investigation of DNA, attached to solid substrates, has recently attracted a lot of attention. In microarray technology [94, 95], end grafted DNA strands are used for the sequential analysis of DNA probes. Applications for biosensing [96–98] are also possible. From a more fundamental point of view, the complex behavior of polymers at interfaces [84, 85, 99, 100] is not yet fully understood and poses a challenging theoretical and experimental problem.

Since DNA [63, 101] is a highly negatively charged polyelectrolyte , it can be manipulated using electric fields [102–104] when grafted on conducting surfaces. Under physiological conditions, salt ions are present in the solvent, leading to screening of electrostatic potentials. If a voltage is applied at a surface which is in contact with a salt solution, ions will accumulate at the interface to compensate the charge induced on the electrode. The width of this diffuse double layer is typically of the order of a few nanometer, over which the electric field drops down. By the formation of a nanoscopic electric double layer, an applied voltage of 1V gives rise to high electric fields up to 10^7 V/cm. These electric fields are strong enough to manipulate negatively charged DNA. At positive surface potentials, the negatively charged DNA tends to be adsorbed on the interface due to electrostatic effects [105, 106]. By reversing the surface charge, DNA molecules can be forced to stand upright on the surface, which has been detected by fluorescence methods [28, 107]. Deeper insight into the underlying mechanisms of the molecular dynamics of grafted DNA chains is not only important for the development of actively controlled biosensors but also because this DNA system serves as a model for the wide-ranging class of linear polyelectrolytes. In this chapter, we will be mostly concerned with the dynamical response of grafted charged chains under the action of externally applied electric fields.

6.1. Experimental motivation

This theoretical study was motivated by experiments with end grafted DNA chains on a gold surface [28]. In these experiments, a self assembled layer of short single stranded DNA chains with a thiol linker at their $5'$ end was chemisorbed on the surface from aqueous solution. The chains had a contour length of 16 nm in double

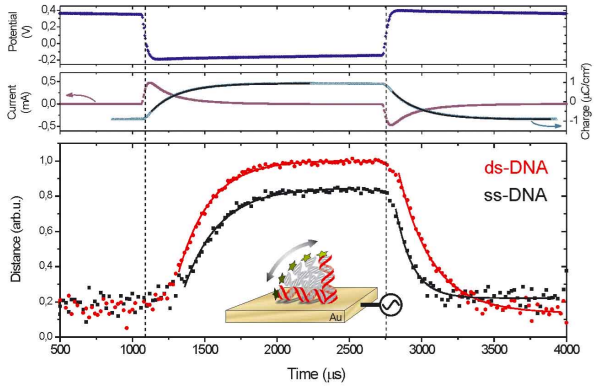

Figure 6.1.: Experimental data for the time resolved measurements of the electrically induced, mechanical switching of a layer of 16 nm long DNA strands. The upper graphs show the electrochemical response of the electrode. The lower graph shows the height of the end points of the DNA above the surface measured by fluorescence methods. The upper red curve corresponds to the data of the ds-DNA, the lower curve to the data of the ss-DNA. The solid lines are exponential fits to the data.

stranded form. The adsorption process was controlled in a way that the surface coverage was low enough, so that steric interactions between the adsorbed chains are negligible. The upper 3′ end was labeled with a dye which was continuously excited by an Argon ion laser. Since the fluorescence intensity is dependent on the height of the dye from the metallic surface due to quenching, the variation of the distance of the chain ends from the gold surface can be measured and therefore the response of the end-tethered DNA strands to the applied surface potential. The applied voltage was repeatedly switched from plus to minus while recording the fluorescence signal. When the measurements were terminated, the layer of the single stranded DNA was hybridized with complementary strands leading to a layer of double stranded DNA. Then the same measurements were performed. Fig. 6.1 shows the result of these measurements.

At positive surface potentials, the negatively charged DNA feels an electrostatic attraction to the surface and tends to be in a flat conformation on the surface. This is seen in the experiments by a decreasing fluorescence signal when switching from negative to positive surface charge. When reversing the applied voltage, the DNA is repelled from the negatively charged surface. This leads to an upright conformation of the chains which is experimentally seen by an increase of the observed fluorescence intensity. Observing the time constants for the up- and down-switching dynamics, a different behavior is found between single stranded (ss) and double stranded (ds) DNA. While the stiff chains show similar time constants, the flexible strands lie down significantly faster than they stand up. As is suggested by our simulations, this is related to different kinetic modes of motion. Due to the rigidity of the ds DNA, the strands have to perform a rotation around their anchoring point whereas the ss

DNA is pulled down segment by segment towards the attractive surface. One part of this chapter will therefore deal with the mechanism of these flexibility dependent switching dynamics. One cautious remark is in order: In the experiments the time scale of charging of the double layer at the gold surface is set by its capacitance and the resistance of the electrolyte solution. This time scale turns out to be of the order of 100 microseconds [28] and is thus much larger than the time scale of DNA diffusion or rotation which is of the order of a few tens of nanoseconds. The different mobilities of double and single stranded DNA thus is only a small modulation of the much larger double layer capacitor charging time.

A possible application of this system are actively controlled biosensors. Molecules which are present in the solution can bind to suitably modified ends of grafted DNA chains. Big adsorbates will increase the friction for the motion of the chains which will lead to a slowing down of the switching dynamics. Also the adsorbate charge will effect the kinetic behavior. By observing the response of the system to the switching of the surface potential one could infer which species are present in the solution.

6.2. Methods

To investigate the dynamics of the system, we use Brownian dynamics simulations. Since the computational effort for molecular dynamics simulations of tethered DNA molecules with explicit solvent [108] is not tractable for longer oligonucleotides at the typical time scales of switching experiments, we use coarse grained methods where the solvent is modeled implicitly and the DNA chain is replaced by beads. Within this method, thermal fluctuations, resulting from the solvent molecules colliding with the polymer, are represented as random forces acting on the chain. The DNA molecules are represented by a bead spring model, where the bending rigidity is explicitly taken into account [91, 109, 110].

The polymer dynamics is described by the Langevin equation, eq. (2.18). Hydrodynamic interactions are taken into account via the wall Greens function, eq. (2.9), obeying the no-slip boundary condition at the position of the interface. The finite particle size is incorporated via a multipole expansion, eq. (2.13). The DNA is modeled as N connected beads with radii a with the intrachain potential given in eq. (3.29).

Two nucleic acid monomers are represented by one simulation bead which leads to a bead radius of 0.34 nm. The simulation of a chain with 24 beads thus corresponds to a 16 nm long, 48 mer DNA strand. Double stranded DNA has a persistence length of 50 nm [63] which is roughly three times the contour length of the used chains. This means that the ds DNA is a rather rigid but still bendable rod. In contrast, the ss DNA has a persistence length of only 2-3 nm [111], leading to a much more flexible behavior. Fig. 6.2 shows the conformational difference between double and single stranded DNA. The parameter for the strength of the harmonic longitudinal potential of neighboring beads is fixed to a value of $\gamma = 400$, ensuring that fluctuations of the contour length of the DNA stay small.

To prevent the beads from overlapping, a truncated, repulsive Lennard Jones po-

Figure 6.2.: Typical conformation of double-stranded (a) and single-stranded (b) DNA at a screening length $\kappa^{-1} = 3.0$ nm. The chains are modeled with 24 beads corresponding to 16 nm long molecules. The persistence lengths used are a) $l_p = 50$ nm and b) $l_p = 2$ nm.

tential, divided by $k_\mathrm{B}T$, with $\epsilon = 3.0$ is included,

$$u_{LJ}(r_i, r_j) = \epsilon \left(\frac{(a_i + a_j)^{12}}{r_{ij}^{12}} - \frac{2 \cdot (a_i + a_j)^7}{r_{ij}^6} + 1 \right) \quad \text{for} \quad r < a_i + a_j \tag{6.1}$$

accounting for the hard-core repulsion between different beads with radii a_i and a_j. The first bead of the DNA is held fixed on the substrate by virtual forces. The solid - solvent interface is modeled as infinitely repulsive, i.e. the single beads are reflected at the boundary.

Electrostatic forces are treated within the Debye Hückel approximation. In the presence of salt ions with a concentration c_s and with valency q, the electrostatic potentials are screened with the inverse Debye length $\kappa = \sqrt{8\pi l_B q^2 c_s}$. This leads to a repulsive potential between the charged beads of the chain ($l_B = e^2/(4\pi\epsilon k_\mathrm{B}T)$ (l_B denotes the Bjerrum length) given by

$$u_\mathrm{mon}(\mathbf{r_i} - \mathbf{r_j}) = q_i q_j \frac{l_B}{|\mathbf{r_i} - \mathbf{r_j}|} e^{-\kappa |\mathbf{r_i} - \mathbf{r_j}|}. \tag{6.2}$$

In the presence of salt ions, the effective charge of the single beads is reduced by counterion condensation [84, 112, 113]. This leads to a renormalized charge of $1e$ per simulation bead, i.e. $q_i = 1$.

Finally, the beads are subject to the externally applied electric field of the surface which leads to an energy

$$u_\mathrm{surf}(\{r_i\}) = \sum_{i=0}^{N-1} \frac{q_i e V_0}{k_\mathrm{B}T} e^{-\kappa z}. \tag{6.3}$$

When switching the surface-DNA interaction by applying an external negative (positive) voltage V_0 at the surface, the strands feel a repulsive (attractive) force, leading to an upright (flat) conformation of the chain at the interface.

In the experiment, the gold surface is covered with a layer of spacer molecules (mercaptohexanol), which modifies the electrostatic DNA - surface interactions [28].

The spacer molecules can be viewed as a layer of low dielectric constant on top of the metal surface. This layer counterbalances the attractive image-charge interaction of a DNA charge due to the metal [105, 106] and leads to a strong repulsive image-charge interaction for small distances, as can be shown theoretically on the Debye-Hückel level [114]. Indeed, in experiments it is seen that physisorbed DNA desorbs when mercaptohexanol molecules are added to the solution and adsorb on the gold surface. The effect of image charges is thus neglected in the theoretical modeling. This is further justified by the fact that the applied surface potentials of the order of 0.125 V are large compared to image charge interactions.

6.3. Simulation results

The dynamical response of one grafted DNA chain, modeled by 24 beads, to an alternating surface potential was simulated by integrating equation (2.18). In the simulations we switched the Debye-Hückel potential instantaneously from a positive value to a negative value, thereby assuming that the double layer charge-reversal is instantaneous. This approximation is justified since the double-layer time constant is proportional to $a\kappa^{-2}$ and thus smaller than the DNA relaxation time which is proportional to L^3. All lengths are expressed in terms of the monomer bead radius a, energies in units of $k_{\mathrm{B}}T$, leading to a rescaled time

$$\tilde{t} = \frac{k_{\mathrm{B}}T}{6\pi\eta a^3}t. \tag{6.4}$$

The integration constant was chosen such that the displacement of the single beads per integration step is in the order of at most five percent of the bead radius. In most cases we choose $\kappa^{-1} = 3.0$ nm, corresponding to 10 mM monovalent buffer solution and $V_0 = \pm\, 0.125$ V. The contour length of the chains was $L = 16$ nm. The ds DNA has a bending rigidity of $l_p = 3.125\ L$ and thus much larger than the contour length, the flexible ss DNA a persistence length of $l_p = 0.15\ L$ and thus smaller than the contour length. The solid - liquid interface is located in the $x - y$ plane at $z = 0$.

6.3.1. Influence of flexibility

The switching behavior of the single stranded DNA is quite different from that of the double stranded DNA if one looks at the single trajectories of the z-component of the end to end vector of the chain. There is a noticeably dispersion for the down-switching trajectories while their slope is almost equal (Fig. 6.3a), whereas the flexible DNA does not show this feature (Fig. 6.3b).

This statistical behavior in the down-switching dynamics for the ds DNA is due to its rigidity. To get to the surface, starting from an upright conformation, the strand has to rotate around its anchoring point and the electrostatic torque due to the surface potential has to overcome thermal fluctuations. Because of the symmetry of the electrostatic torque, this can only happen if the strand is sufficiently tilted by an angle α with respect to the surface (Fig. 6.4). The torque is generated by the

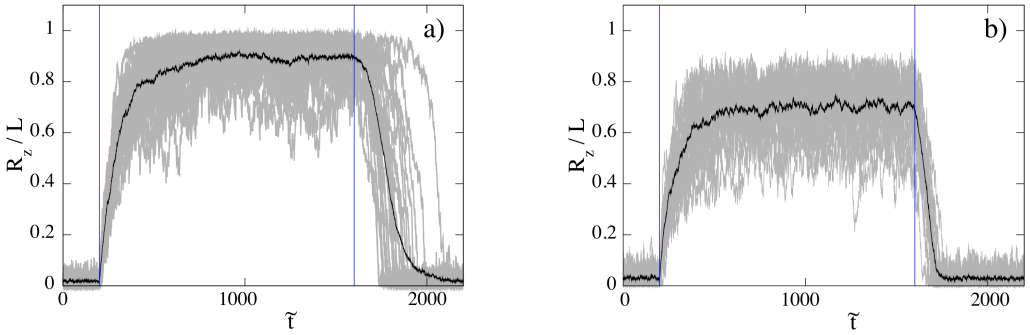

Figure 6.3.: Z-component of the end to end vector of double (a), $l_p = 3.15$ L) and single (b), $l_p = 0.15$ L) stranded DNA ($\kappa^{-1} = 3$ nm, $L = 16$ nm). The starting surface potential is +0.125 V. At $\tilde{t} = 200$ the potential is switched to −0.125 V, at $\tilde{t} = 1600$ it was switched back, denoted by the vertical lines. The gray lines show single trajectories. The average (black line) is taken from 30 simulated trajectories.

potential energy U of the strand in the electric field of the surface.

$$\mathbf{T} = (\mathbf{r} \times \nabla)\, U \tag{6.5}$$

If α denotes the angle between the strand and the surface normal, the only non vanishing component of $\mathbf{T}$ is given by the partial derivative $T_\alpha = -\partial_\alpha U$. For a rod of length L and total charge Q with one end fixed on the surface, and assuming an electrostatic potential as defined in eq. (6.3), the angular-dependent potential energy is given by

$$\begin{aligned} U(\alpha) &= \int_0^L ds\, \frac{Q}{L} V_0 e^{-\kappa \cos(\alpha) s} \\ &= \frac{QV_0}{L\kappa \cos(\alpha)} \left(e^{-\kappa L \cos(\alpha)} - 1 \right) \approx -\frac{QV_0}{L\kappa \cos(\alpha)}. \end{aligned} \tag{6.6}$$

The rod will be rotated deterministically around its fixed end when the generated torque, given by

$$T(\alpha_c) = -\frac{\partial U(\alpha_c)}{\partial \alpha_c} \approx -\frac{QV_0}{\kappa L} \frac{\sin(\alpha_c)}{\cos^2(\alpha_c)} \tag{6.7}$$

becomes bigger than $k_\mathrm{B}T$.

If the angle is too small, the strand shows diffusive rotation. This leads to a random distribution of starting times for the deterministic rotation of the strand around its first bead. This feature gets more pronounced for increasing rigidity of the strand, i.e. going to the rigid rod limit, because chain bending is still possible for the ds DNA.

Since the ss DNA is very flexible, it can be pulled down bead by bead when switching from repulsive to attractive surface potential. The single trajectories in Fig. 6.3 do

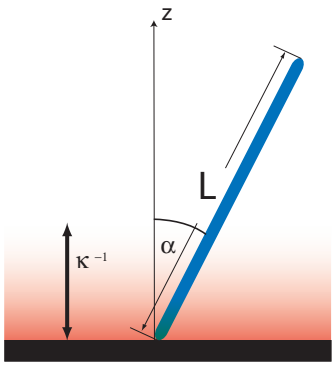

Figure 6.4.: Scheme of the configuration of a rigid strand grafted to the surface. The electrostatic potential of the surface is screened within the screening length κ^{-1} above the surface. The angle α has to be large enough so that the electrostatic torque exceeds the strength of angular thermal fluctuations.

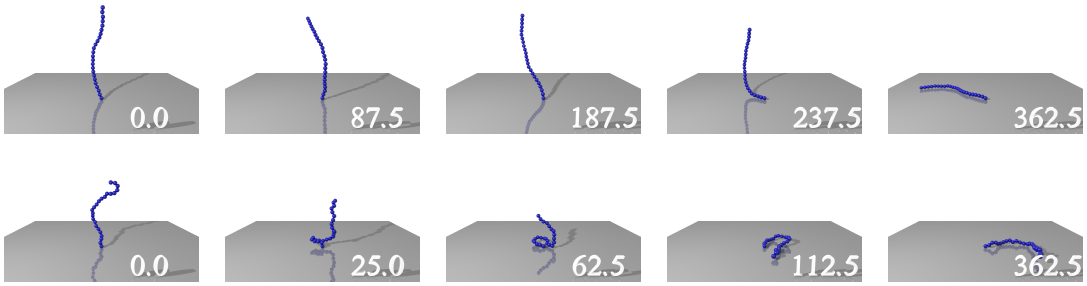

Figure 6.5.: Snapshots of the downswitching dynamics for double (upper row) and single (lower row) stranded DNA at different times $\tilde{t}$ after the surface voltage was reversed. The ss DNA lies down significantly faster than the ds DNA since it is pulled down bead by bead.

not exhibit a broad distribution as it is the case for the ds DNA. In Figs. 6.5 and 6.6, snapshots at different simulation times are shown to elucidate the different behavior of single and double stranded DNA.

When switching from positive to negative surface potential, no dispersion in the single trajectories both for the flexible and rigid strands is observed. Since all the monomers are close to the wall at the beginning, the repulsion acts on all monomers equally, and the strand starts to stand up. Due to the screened surface potential, only the beads close to the wall are feeling a repulsive force. The beads closest to the boundary then pull the others away from the surface, finally reaching an upright conformation (Fig. 6.6). During the switching process, ds DNA is always in a straight configuration whereas the ss DNA shows significant crumpling. Note, that the equilibrium end to end distance for the ds DNA is bigger than that for the more flexible ss DNA (Fig. 6.3). This is due to the more straight conformation of the rigid ds DNA.

The switching behavior also depends on the salt concentration and thus on the value of the Debye screening length κ^{-1}. Fig. 6.7 show the response of single and double stranded DNA to alternating surface potentials. With increasing screening length, the electrostatic forces become more long ranged. Firstly, the single monomers are repelling each other, this leads to a stretching of the DNA strands with decreasing

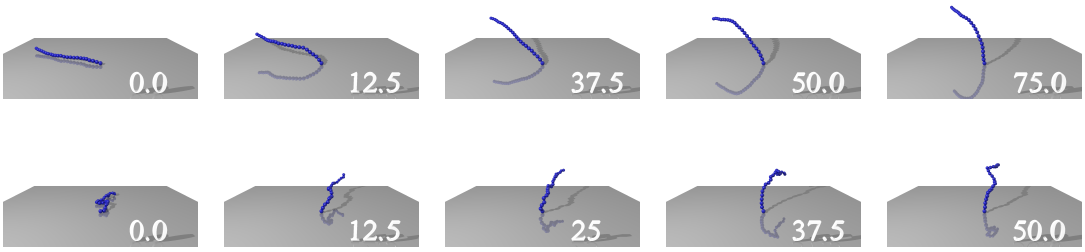

Figure 6.6.: Snapshots of the upswitching dynamics for double (upper row) and single (lower row) stranded DNA at different times $\tilde{t}$ after the surface voltage was reversed.

salt concentration. Secondly, more and more DNA segments are feeling the surface potential with increasing screening length, the down and upward motion of the chain gets faster. On the other hand, since we are working at constant surface potential, the absolute forces exerted on the monomers close to the surface increase with decreasing screening length, since the value of the electric field $\mathbf{E} = \nabla V(z) = \kappa V_0 \exp(\kappa z)\hat{e}_z$ generated by the surface potential also depends on the screening constant. This increase of the electric field leads to a pronounced chain bending of the ds DNA at the beginning of the downward motion making the dynamics more similar to that of the flexible strands. For decreasing κ^{-1} the critical angle for the down-switching of the ds DNA gets bigger, leading to a slowing down of the motion.

The above mentioned effects partly counterbalance each other. For all used parameters κ^{-1}, the ss DNA lays down significantly faster than it stands up while for the ds DNA the time constants for the up and down-switching motion are close to each other (Fig. 6.8). The time constants obtained by fits of the data sets to single exponential functions are listed in table 6.1. Especially for the downward motion, average trajectories are not well reproduced by single exponential functions. Therefore the fitting interval was chosen in a range where the agreement with the graphs was sufficient. Nevertheless, these switching times τ are dependent on the range of that interval.

The absolute time scales for the experimental and the theoretical results differ substantially from each other. As explained before, in the experiments the gold surface is charged over the electrolyte - solution which acts as an electric resistance and thus determines the charging time of the electric double layer in a decisive manner. This charging time turns out to be of the order of hundreds of microseconds [28] and thus much larger than the DNA relaxation times which are in the nano-second range. Therefore, the absolute time constants of the switching process measured in the experiment and in the simulation can not be compared. Rather, the experiments served as a motivation for the present simulation studies. Experimental studies with a much shorter charging time constant are currently under development. Incidentally, the orientational relaxation times we find in the hydrodynamic simulations are of the same order as the ones inferred from all-atomistic MD simulations [108].

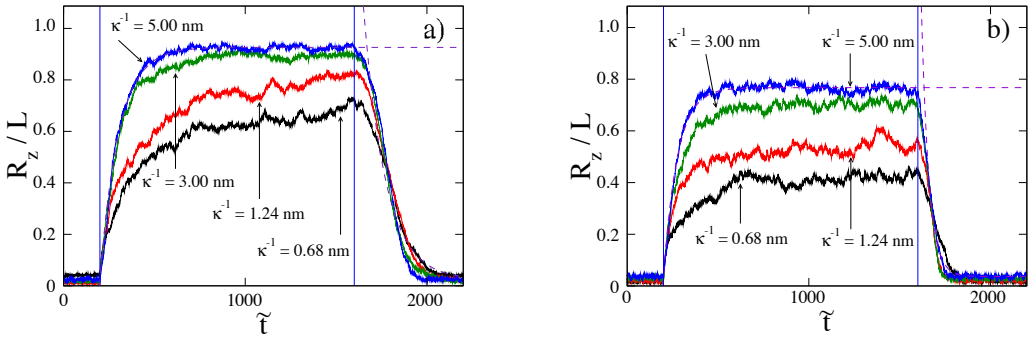

Figure 6.7.: Z-component of the end to end vector of double (a), $l_p = 3.125$ L) and single (b), $l_p = 0.15$ L) stranded DNA with contour length $L = 16$ nm for different values of the screening length κ^{-1}. The starting surface potential was +0.125 V. At $\tilde{t} = 200$ the potential was switched to -0.125 V, at $\tilde{t} = 1600$ it was switched back, denoted by the vertical lines. The graphs were obtained by averaging over 30 single trajectories. The dashed lines are showing the exponential fit function for $\kappa^{-1} = 5.0$ nm to obtain the switching constants $\tilde{\tau}$ from table 6.1.

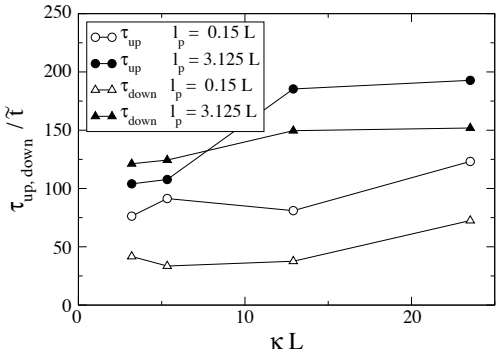

Figure 6.8.: Up - and down - switching time constants for various values of κL. The switching times are obtained from the data shown in Fig. 6.7 by fitting the switching process to exponential functions (upswitching: $f(x) = a_0(1 - \exp(-(\tilde{t} - 200)/\tau_{up}) + C$ for $200 < \tilde{t} < 1600$, down - switching: $f(x) = a_0 \exp(-(\tilde{t} - 1600)/\tau_{down}) + C$, for $1650 < \tilde{t} < 2200$, the constant C was determined by the equilibrium z-component of the end to end vector at positive surface potential).

κ^{-1} (nm)	0.68	1.24	3.0	5.0
single stranded DNA				
τ_{up}	123.2 (24.6 ns)	81.0 (16.2 ns)	91.7 (18.3 ns)	76.3 (15.3 ns)
τ_{down}	72.5 (14.5 ns)	37.6 (7.5 ns)	33.5 (6.7 ns)	41.7 (8.3 ns)
τ_{up}/τ_{down} (sim.)	1.7	2.2	2.7	1.8
τ_{up}/τ_{down} (exp.)	-	-	2.1	-
double stranded DNA				
τ_{up}	192.8 (38.6 ns)	185.3 (37.0 ns)	107.7 (21.5 ns)	104.0 (20.8 ns)
τ_{down}	151.9 (30.4 ns)	149.6 (29.9 ns)	124.4 (24.9 ns)	121.2 (24.2 ns)
τ_{up}/τ_{down} (sim.)	1.3	1.2	0.9	0.9
τ_{up}/τ_{down} (exp.)	-	-	0.9	-

Table 6.1.: Up - and down - switching time constants for single and double stranded DNA in rescaled time units $\tilde{t}$, obtained by fits of the data shown in Fig. 6.7 to single exponential functions. The numbers in brackets correspond to the real time scale evaluated by eq. (6.4), $t/\tilde{t} \approx 0.2$ ns at $\eta_{H_2O} = 10^{-3}$ Pas, $k_{\mathrm{B}}T = 25 \times 10^{-3}$ eV and $a = 0.34$ nm. The experimental data is taken from [28].

6.4. Effect of an end-tethered ligand

A possible application of the electrical switching of DNA strands is a biosensor. Molecules, present in the solvent, are envisioned to be able to bind at the end of the DNA strands via some suitably chosen end groups. This changes the dynamical response of the DNA - chains, which can then be detected. Since different molecules in general have different charge and size, one could determine which molecule is present from the characteristic switching behavior. Experimentally this could be achieved by recording the fluorescence signal of dye labeled DNA strands.

6.4.1. Ligand size

To model an end-adsorbed molecule on the DNA chain, an additional sphere was attached to the strand. The hydrodynamic effect of the different size of the last bead is taken into account by changing the corresponding radius in the multipole expansion (eq. 2.13) for the HI between the beads. The different radius also changes the self-mobility. Big adsorbate sizes give rise to enhanced friction which slows down the switching dynamics of the strands. Fig. 6.9 middle shows a snapshot of an end grafted DNA with an adsorbed molecule with a radius ten times the DNA monomer size. The right part of the figure shows the stream lines and demonstrates that although the stream lines do not perfectly superimpose with the surface of the large bead at the end, some of the hydrodynamic effect due to the terminal bead is captured by the Rotne-Prager Green's function.

The radius of the last bead was varied from the DNA monomer radius up to ten times the DNA bead radius. The charge of the adsorbed molecule was set to zero.

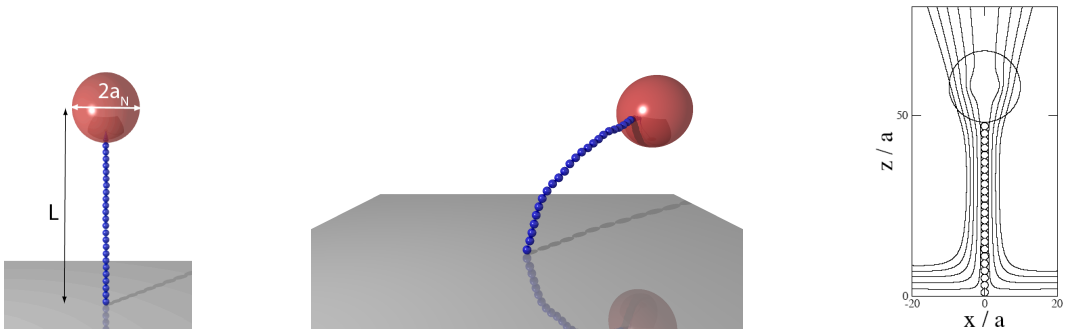

Figure 6.9.: The left picture shows a schematic view of an end grafted double stranded DNA, consisting of 24 beads, with an adsorbed molecule of radius $a_N = 10a$ on top. The middle picture is a simulation snapshot at repulsive surface potential. The generated streamlines when dragging this chain along the surface normal are shown to the right.

The results are shown both for ds and ss DNA (Fig. 6.10).

For slightly higher radii of the adsorbate, almost no difference is seen in the switching dynamics. With increasing size of the last bead, a down-slowing of the motion is observed due to the larger friction. Since the beads can not penetrate into the surface, the minimal height for the chain at attractive surface potentials becomes larger. Because of the screened surface potential, the effective repulsion when switching to negative surface charge is not as strong as for small adsorbates. This also decreases the starting slope for the up-switching dynamics of the strands.

For the rigid ds DNA, a second effect additional to the increased friction, should slow down the dynamics of the switching. Since the starting times for the downward motion are diffusion limited, one expects an effect due to the lower diffusion constant of the last bead. To observe this feature, the strands have to be in equilibrium at repulsive surface potentials when reversing the surface charge. This is not the case in the simulation which can be seen in Fig. 6.10a) where the z-component of the end to end vector of the chain with an adsorbed molecule of radius 10a is not equilibrated when changing to positive surface charge. Since a bead with radius R has almost the same friction as a rod of length 2R, the situation should be approximatively the same when adsorbing a neutral chain with length 2R on top of an end tethered chain.

6.4.2. Ligand charge

The effect of the ligand charge can also be probed. Fig. 6.11 shows the dynamical response of ds and ss DNA with an additional charged bead on top. The radius of the adsorbate was set to the same value as the radius of the DNA monomers.

For negatively charged adsorbates, a stiffening of the strands can be seen. The equilibrium end to end distance in the upright position increases for increasing negative charge. This is due to repulsion of the negative DNA monomers from the negative adsorbate. This effect is bigger for the ss DNA, since it is less stretched than the ds DNA due to its smaller persistence length.

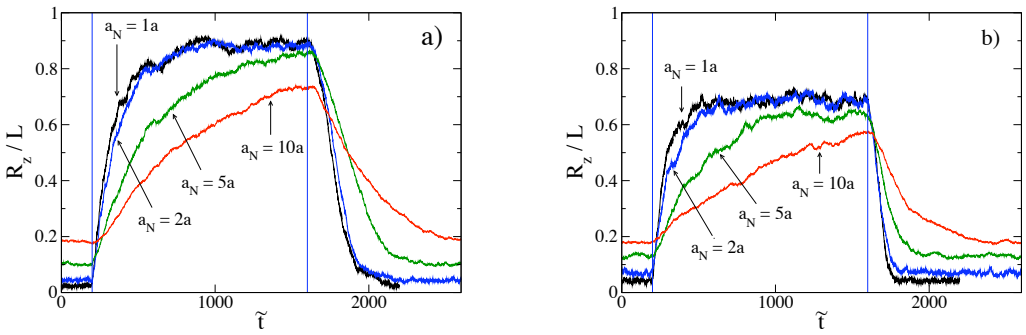

Figure 6.10.: Z-component of the end to end vector of double (a), $l_p = 3.125\ L_0$) and single (b), $l_p = 0.15\ L_0$) stranded DNA ($\kappa^{-1} = 3.0$ nm). An additional neutral bead with different radius a_N was adsorbed at the end of the chains. R_z is scaled with the total contour length $L = L_0 + a + a_N$, with $L_0 = 16$ nm being the length of the bare DNA. The simulations started with positive surface charge, the switching times are marked with the vertical lines. The graphs were obtained by averaging over 30 single trajectories.

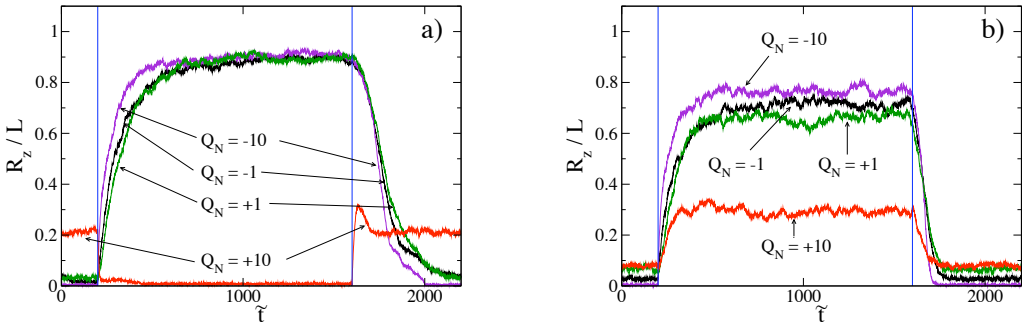

Figure 6.11.: Z-component of the end to end vector of double (Fig. a), $l_p = 3.125 L_0$) and single (Fig. b) $l_p = 0.15 L_0$) stranded DNA ($\kappa^{-1} = 3.0$ nm). An additional charged bead (the charge is given in units of the DNA monomer charge) with the same radius as the DNA monomers was adsorbed at the end of the chains. R_z is scaled with the total contour length $L = L_0 + 2a$, with $L_0 = 16$ nm being the contour length of the bare DNA. The simulations started with positive surface charge, the switching times are marked with the vertical lines. The graphs were obtained by averaging over 30 single trajectories.

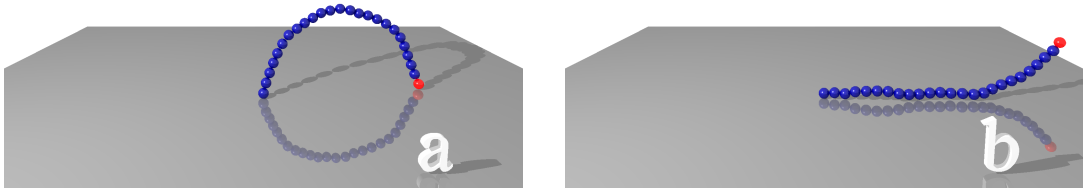

Figure 6.12.: Snapshots of double stranded DNA with an adsorbed molecule of charge +10 e at negative surface potential a) and at positive surface potential b)

The dynamics of the switching process is also changed. At positive surface potentials, the negatively charged adsorbate is attracted to the surface, accelerating the downward motion. For positively charged adsorbates, the motion is slowed down, and vice versa for the upward process. This effect only applies when the last bead is close to the surface, due to the screening of the surface potential.

For strongly positively charged ligands, the dynamics changes drastically, as can be seen from the simulations of a DNA chain with an adsorbed molecule with ten times the positive charge as one DNA monomer. The last bead on top of the double stranded DNA is very close to the surface for negative surface charge. The DNA is approximatively bent to a semicircle (Fig. 6.12a). The bending energy is too low to overcome the attractive potential between the surface and the molecule. If the surface potential is reversed, the DNA lies partly down on the surface, but the last part is repelled from the wall due to the large repulsion between the molecule and the surface (Fig. 6.12b).

The more flexible ss DNA shows a different behavior. Since the energy cost due to bending is quite low, the strand wraps around the strongly positively charged molecule to minimize its electrostatic energy (Fig. 6.13). The positive adsorbate charge is screened by the negative DNA. The strand shows qualitatively the same switching behavior as the bare ss DNA, since the overall charge still is negative, but the extent of the up and down motion is significantly reduced.

6.4.3. Switching of two - component chains

Instead of attaching one single molecule to the end of a DNA strand, one could also think about adsorbing another strand on top of the other. By this mechanism one could probe the presence of other DNA strands in solution and detect adsorbing events or hybridization with chains of varying length.

In the simulation, ds DNA is attached to a single stranded chain while the link between the two chains is fully flexible and freely rotating. The simulations were performed for an anchored ss DNA with a ds DNA on top, both with equal length,

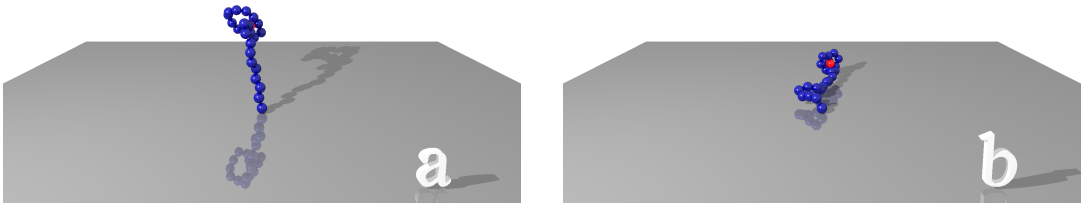

Figure 6.13.: Snapshots of single stranded DNA with an adsorbed molecule of charge $+10e$ at negative surface potential a) and at positive surface potential b)

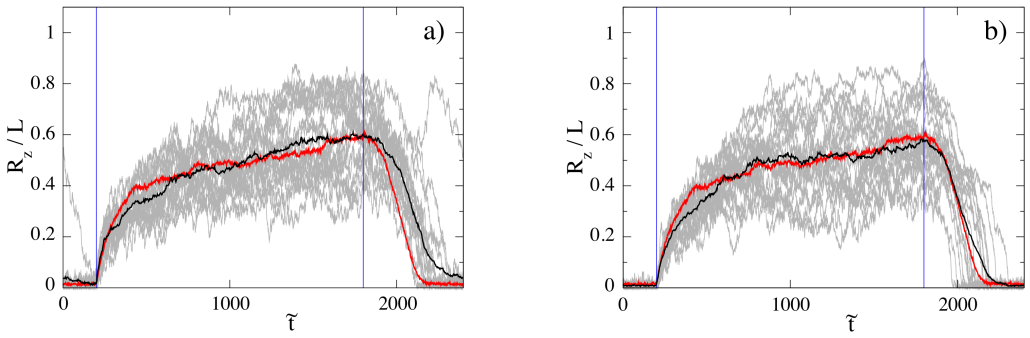

Figure 6.14.: Height of the end point of the two-component chain ($L = 32$ nm) above the surface. The gray lines show the single trajectories, the black line denotes the average. The chain consists of an anchored ds DNA with a flexibly connected ss DNA on top (a) and the other way round for (b). For comparison, the results of a $L = 32$ nm long single stranded DNA are shown as the red line. At the beginning, the surface potential is +0.125 V. It is reversed at the position of the vertical lines. The average was taken over 30 trajectories.

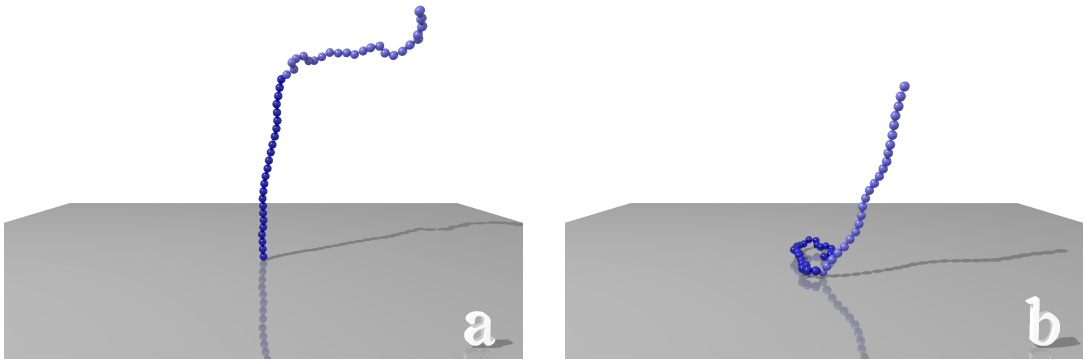

Figure 6.15.: Snapshots of the conformation of the two-chain system. (a) shows a surface-anchored ds DNA with a terminally attached ss DNA chain at negative surface potential, (b) shows a surface-anchored ss DNA with a terminally attached ds chain during the downswitching process, i.e. after switching the surface potential from negative to positive.

and vice versa. If one compares the height of the chain end from the surface, no big difference in the switching dynamics is found between the two conformations (Fig. 6.14). Both show a dispersion of the single trajectories. For the grafted double stranded DNA (Fig. 6.14a and 6.15a), the random distribution is due to the effect discussed in section 6.3.1. A similar behavior is observed for the system where the flexible DNA is fixed to the surface. When switching the surface potential from negative to positive potential, the ss DNA is pulled down, dragging the second strand along with it. Since the second strand is pulled only at its end, it tends to align perpendicular to the wall. If the ss DNA is adsorbed on the surface, the ds DNA is still in an upright position, so that the same effect as before leads to the random distribution of the trajectories. Fig. 6.15b shows a snapshot of the simulation at positive surface potential.

6.4.4. Collective effects

In experiments, one typically deals with a whole layer of grafted chains. The question arises, if hydrodynamic interactions between different chains would significantly change the dynamical behavior. One can show, that the solvent flow field due to a point-force near a no slip boundary pointing parallel to the surface normal decays as r^{-3} [115]. For grafting densities at which the chains do not overlap, collective effects should be small. When including minimal image boundary conditions in the simulation, the dynamics shows almost no difference in the switching behavior. As long as the strands do not overlap, which will lead to steric interactions, it is a good approximation to neglect collective effects.

6.5. Conclusion

In this study, the electrical switching of an end grafted DNA chain was investigated using Brownian dynamics simulations. Due to its higher bending rigidity, ds DNA shows a different dynamical response to the external electric field than the more flexible single stranded DNA. The stiff chain shows a broad distribution of trajectories in the down-switching process since it has to perform rotational diffusion until it is tilted enough, with respect to the surface, so that the torque, exerted through the surface potential, exceeds thermal fluctuations. The ss DNA shows no such dispersion, because it can be pulled down bead by bead since the energy associated with chain bending is small. These findings are in qualitative agreement with recent experimental results [28].

The opportunity to use this system for biosensing purposes is also discussed. It is possible to modify the system by attaching an additional bead on top of the chain with varying radius and charge. This influences the dynamical response of the system which can be detected and evaluated to identify the adsorbed molecule. Also, end attached single stranded DNA can be partially hybridized by DNA chains present in the solvent, making it possible to be sensitive for the binding of DNA chains, since this also leads to a characteristic signature in the switching dynamics.

Part II.

Atomistic description of interfacial water dynamics

7. Interfacial water

In contrast to the first part of the thesis, in which the solvent molecules are described in a coarse grained fashion, the solvent molecules are modeled on an atomistic level in the following chapters. Due to the neglect of the solvent degrees of freedom, continuum models fail to correctly describe water specific effects since water is a polar molecule and interacts strongly via directional hydrogen bonds. Although hydrodynamic theory holds surprisingly well even down to Angström scales, the material equations have to be obtained from atomistic simulations. The hydrodynamic boundary condition and the viscosity profile of water at surfaces is of particular interest and will be discussed in the following chapters.

Water is by far the most important liquid, not only in biology but also in many industrial and technological applications and every day's life. Its properties such as its potency as a solvent or its crystallization behavior are remarkable. For many applications like in microfluidics or biology, the behavior of interfacial water is of prime importance. The geometric constraint of a solid surface as well as the interactions of the water with the substrate lead to structural changes of the liquid compared to its bulk properties. Surfaces can be divided into two classes according to their affinity to water: hydrophilic, water attracting and hydrophobic, water repellent surfaces. At charged or partially charged surfaces, the polar water molecules can increase their internal energy from Coulomb interactions. Consequently, surfaces which bear electric charges belong to the class of hydrophilic surfaces. In contrast, non polar surfaces are mostly hydrophobic since the water molecules experience a loss of hydrogen bonding at the interface. These hydrophobic and hydrophilic effects have implications on the solubility of particles or for protein folding problems.

We want to analyze the structure and dynamics of interfacial water via molecular dynamic (MD) simulations. Firstly, we concentrate on the equilibrium properties of water in contact with a hydrophobic diamond surface. Our main focus is on the calculation of the contact angle, the angle a liquid droplet forms on the surface. By a variation of the simulation parameters, the hydrophobicity of the surface is modified and quantified by the contact angle. The following chapter 8 then analyzes the hydrodynamic boundary condition at these surfaces in non-equilibrium shear flow simulations. The slip length at the hydrophobic diamond surface is only 2 nm. From simulations with different surface hydrophobicities, we find a quasi-universal dependence of the slip length on the contact angle. We also show that the presence of surface adsorbed gas only moderately increases the slippage. Chapter 9 then extends the analysis of hydrophobic surfaces to polar, hydrophilic surfaces. From the velocity profile in the interfacial region and the diffusion of the water molecules we do not find evidence for a layer of frozen water or for an increase in the interfacial viscosity of several orders of magnitude at hydrophilic surfaces, as was often reported in the

literature [33–37].

7.1. Molecular Dynamics simulations

In MD simulations, the system is modeled on an atomistic scale. The trajectories of the constituents are calculated using Newton's equations. Particles interact via bonding interactions, often modeled with harmonic springs and cosine series for torsional potentials [116], and non-bonded Coulomb and Dispersion interactions. Dispersion interactions between particle species A and B with distance r are described by a 6-12 Lennard Jones potential,

$$u(r) = 4\epsilon_{\mathrm{AB}} \left[\left(\frac{\sigma_{\mathrm{AB}}}{r} \right)^{12} - \left(\frac{\sigma_{\mathrm{AB}}}{r} \right)^{6} \right]. \tag{7.1}$$

In the simulations, the Lennard Jones interactions are truncated at a radius $R_0 = 0.8$ nm to speed up the computer simulations. The same cutoff radius is used for the short ranged electrostatic interactions. A variation in the cutoff radius R_0 leads to a noticeable change in the simulation results. The effect of the cutoff radius on the contact angle of the diamond surface is discussed in detail in section 7.3.2. Long ranged electrostatic interactions are calculated with the Particle-Mesh Ewald (PME) method [117, 118]. For all simulations, we use the SPC/E [119] water model. In this three site model the water molecule bears partial charges $q_{\mathrm{O}} = -0.8476\ e$ and $q_{\mathrm{H}} = 0.4238\ e$ at the position of the oxygen and hydrogen nuclei. The OH bond length is 0.1 nm with a tetrahedral bond angle of $\theta = 109.5°$ at the oxygen position. The Lennard Jones potential is centered at the oxygen position with the parameters given in Tab. 7.1. Periodic boundary conditions are applied in all three spacial directions. The simulations are performed in the NAP_zT ensemble, i.e. at fixed particle number N, surface area A, temperature T and vertical pressure P_z. This means that the height of the box is free to fluctuate. The whole system is coupled to a heat bath at 300 K and to a pressure of 1 bar via the Berendsen algorithm [120] with coupling constants $\tau_T = 0.4$ ps (temperature) and $\tau_p = 1.0$ ps (pressure). All bonds including hydrogen atoms are constraint via the LINCS [121] algorithm. The simulations are carried out with the `GROMACS` [122] package.

7.2. Surfaces

We consider a hydrophobic, hydrogen terminated diamond surface. The diamond slab is modeled with 2323 carbon atoms, arranged in the well known double face-centered-cubic lattice with lattice constant $a = 3.567$ Å. The surface normal of the (100) plane points in the $\hat{e}_z$ direction. The lateral extension of the slab is 3.0×3.0 nm^2, its thickness is 1.5 nm. The atoms of the diamonds are connected by harmonic bond and angle potentials. Also, torsional degrees of freedom are considered with the force constants of the GROMOS96 version 53A6 force field [123]. The surface layer of the diamond is reconstructed and terminated by H atoms, which leads to an ideal hydrophobic surface. Carbon atoms and water molecules interact via the Lennard Jones potential

atom types	σ [nm]	ϵ [kJ/mol]
C-C	0.3581	0.2774
O-O	0.3166	0.6502
C-O	0.3367	0.4247

Table 7.1.: Forcefield parameters of the GROMOS forcefield for carbon and the SPC/E water model for the Lennard Jones potential given in eq. (7.1).

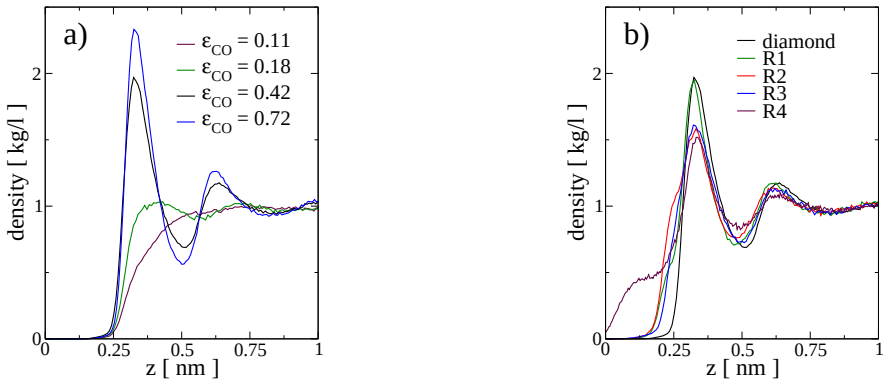

Figure 7.1.: Water density profiles for different liquid/solid interaction energies and surface structures. The center of the topmost surface atoms is located at $z = 0$. Fig. (a) shows the water density profiles of the diamond surface for different liquid/solid interaction energies ϵ_{CO} given in kJ/mol. In (b), the density profiles for the different surface structures shown in Fig. 7.2 are plotted for the standard GROMOS value $\epsilon_{CO} = 0.42$ kJ/mol.

in eq. (7.1) with interaction parameters given in Tab. 7.1. For tuning the hydrophobicity of the surface, the liquid/solid interaction energy ϵ_{CO} between surface atoms and water molecules is varied in the range between 0.11 kJ/mol - 0.72 kJ/mol, while the interaction range σ_{CO} is held constant. Decreasing the liquid/solid interaction energy leads to increasing hydrophobicity since the water molecules are less attracted by the solid.

A variation in the interaction energy leads to changes in the water density close to the interface, Fig. 7.1a). The density profiles are obtained in simulations of the diamond surface in contact with 1850 water molecules in a $3.0 \times 3.0 \times 8.0$ nm^3 simulation box in the NAP_zT ensemble. For not too low values of ϵ_{CO}, a layering of the water molecules is clearly visible from the peaked structure of the density profile. For the standard GROMOS value $\epsilon_{CO} = 0.42$ kJ/mol, the water density in the first layer is roughly twice the bulk density. Lowering the interaction energy results in a decrease of the height of these peaks and even makes them vanish for the lowest interaction energy. The density profile for the lowest interaction energy is similar to an air/liquid interface. Therefore, by tuning the interaction energy, a smooth transition from a

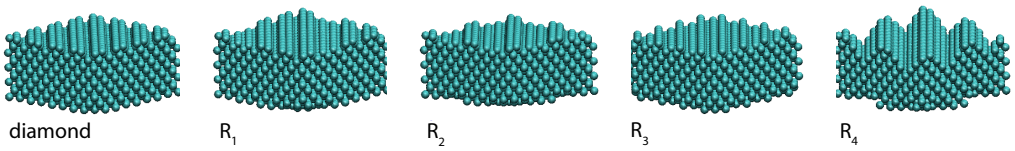

Figure 7.2.: Hydrophobic diamond surfaces. The rough surfaces are constructed by deleting some of the surface atoms.

liquid/solid to a liquid/air interface is obtained.

Apart from the smooth diamond surface, we also use surfaces with different degrees of nano-roughness. These surfaces are constructed by setting the interaction between selected surface atoms and all water molecules to zero. The different surface structures are shown in Fig. 7.2. Surface R_1 is constructed by erasing every third pair of rows of surface atoms, and surface R_2 is obtained by the deletion of every second pair of rows. For the construction of R_3, every second single row of carbon atoms is deleted. The roughest surface, R_4, is generated by removing carbon atoms down to the fourth surface layer of carbon atoms. Again, deletion of a surface atom merely means that ϵ_{CO} is set to zero for this distinct atom. Note, that these surfaces are not superhydrophobic surfaces for which the length scale of the surface structuring is much larger. Rather, these surfaces are used in chapter 8 to examine the influence of surface structure on the hydrodynamic boundary condition. From the density profiles in Fig. 7.1b), it can be seen that the water molecules fill the gaps, left by the deleted surface atoms.

7.3. Contact angle

One important and experimentally easily accessible parameter is the contact angle. This contact angle is in the range from 180° (air) up to 0° for very hydrophilic surface. On smooth surfaces, contact angles up to 130° are observed [125]. For higher contact angles a patterned surface is required. In MD simulations, this angle can either be determined via the simulation of a nanodroplet on the surface or via the calculation of the surface tension. In this study, the latter method is used to compute the contact angle.

7.3.1. Calculation of the contact angle

Via Young's law [126], the contact angle is given by

$$\cos\theta = -\frac{\gamma_{\mathrm{ls}} - \gamma_{\mathrm{sv}}}{\gamma_{\mathrm{lv}}}, \tag{7.2}$$

with the surface tensions of the liquid/solid (ls), solid/vapor (sv) and liquid/vapor (lv) interfaces. In the simulations, the surface tension is obtained from the diagonal

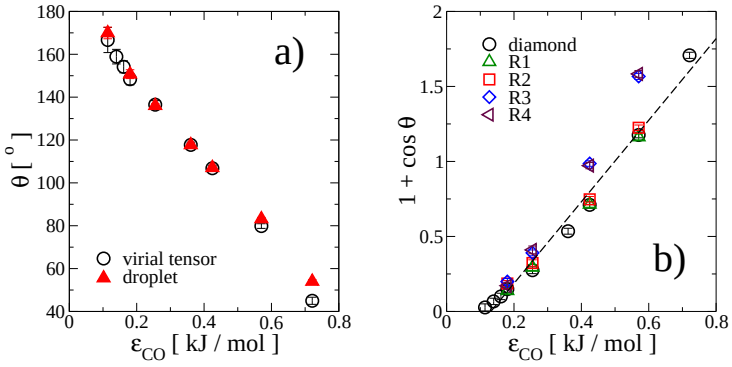

Figure 7.3.: Contact angles for water in contact with the diamond surface determined via the virial tensor in dependence of the interaction energy ϵ_{CO}. a) shows also data for the simulation of a nano droplet in contact with the diamond surface [124]. In b), also data for the rough surfaces are shown.

components of the virial tensor [127],

$$\gamma = \frac{1}{2A}[2\Pi_{zz} - (\Pi_{xx} + \Pi_{yy})]. \tag{7.3}$$

with surface area A and the virial tensor

$$\Pi_{\mu\nu} = \langle \sum_{i=1}^{N} r_i^{\nu} F_i^{\mu} \rangle \tag{7.4}$$

with the positions $\mathbf{r}_i$ and forces $\mathbf{F}_i$ of the single particles. For the calculation of the virial tensor, one diamond slab in contact with 1850 water molecules in a $3.0 \times 3.0 \times 8.0$ nm^3 box is simulated. The surface atoms are frozen and all interactions between the surface atoms are switched of. This procedure yields the difference $\gamma_{\mathrm{ls}} - \gamma_{\mathrm{sv}}$ of the surface tensions. To calculate the surface tension of the air-water interface, a water film consistent of 751 molecules is simulated in a $3.0 \times 3.0 \times 12.0$ nm^3 box in the NVT-ensemble which yields a surface tension of $\gamma_{\mathrm{lv}} = 0.0527$ N/m. The systems first were equilibrated for at least 200 ps with subsequent production runs of 5 ns.

Fig. 7.3a) shows the results for the evaluation of the contact angle for the diamond surface, compared to the results obtained from the simulation of a nanodroplet on the surface [128]. The data for the droplet method are taken from Ref. [124] and are in excellent agreement with the method used in this work. The contact angle at the diamond surface with the standard GROMOS forcefield, see Tab. 7.1, is 106°. In Fig. 7.3b), we plot the results as $1+\cos(\theta)$ as a function of the liquid/solid interaction energy ϵ_{CO}. We obtain a nearly linear dependence of $1 + \cos(\theta)$ as a function of ϵ_{CO}. This observation can be rationalized as follows: the surface tension of the liquid/solid interface can be calculated from the work H_{12} per surface area, which is necessary to separate a slab of liquid from a slab of solid. This work is given as the sum of

the surface energies of the two created interfaces, i.e. solid/vapor and liquid/vapor, minus the energy of the destroyed liquid/solid interface [126],

$$H_{12} = \gamma_{\mathrm{sv}} + \gamma_{\mathrm{lv}} - \gamma_{\mathrm{ls}}. \tag{7.5}$$

The work H_{12} is given by the negative liquid/solid interaction energy of a solid slab in contact with the liquid and can be calculated approximately, assuming homogeneous solid and liquid densities ρ_{s} and ρ_{l}. In this simple calculation, electrostatic contributions, the inhomogeneous water density close to the surface as well as interfacial entropy are neglected.

The interaction energy of one single liquid molecule with the solid phase is given by

$$\begin{aligned} v_{\mathrm{ls}}(z_0) &= \rho_{\mathrm{s}} \int_{z_0}^{\infty} dr \int_0^{2\pi} d\phi \int_{z_0/r}^{1} d\cos\theta \; r^2 u(r) \\ &= 2\pi\rho_{\mathrm{s}} \int_{z_0}^{\infty} dr \; (r^2 - z_0 r) u(r), \end{aligned} \tag{7.6}$$

with the intermolecular liquid/solid interaction potential $u(r)$ and the coordinate system shown in Fig. 7.4. If the intermolecular potential consists of a short ranged repulsive and a long ranged attractive part, the water will occupy the region where the potential energy is negative to minimize its internal energy. With $v_{\mathrm{ls}}(z) < 0$ for $\sigma' < z < \infty$, H_{12} is obtained by the integration over all liquid molecules. An integration by parts then leads to

$$H_{12} = -\rho_{\mathrm{l}} \int_{\sigma'}^{\infty} dz \; v_{\mathrm{ls}}(z) \tag{7.7}$$

$$= -\pi\rho_{\mathrm{l}}\rho_{\mathrm{s}} \left[\int_{\sigma'}^{\infty} dz \; z^3 u(z) - \sigma'^2 \int_{\sigma'}^{\infty} dz \; z u(z) \right]. \tag{7.8}$$

If the Lennard Jones potential in eq. (7.1) is used for the intermolecular potential, H_{12} is a linear function of the interaction energy between the water molecules and the surface atoms ϵ_{CO}. From Young's equation, eq. (7.2), it follows, that the cosine of the contact angle is linearly dependent on the interaction energy,

$$1 + \cos\theta = \frac{\gamma_{\mathrm{sv}} + \gamma_{\mathrm{lv}} - \gamma_{\mathrm{ls}}}{\gamma_{\mathrm{lv}}} = \frac{H_{12}}{\gamma_{\mathrm{lv}}} \propto \epsilon_{\mathrm{CO}}. \tag{7.9}$$

As can be seen in Fig. 7.3b), the linear dependence of $1 + \cos\theta$ is a good fit to the data points. For smaller values of ϵ_{CO} the water density at the interface decreases and entropic effects connected to interfacial shape and density fluctuations become important, invalidating the simple arguments that lead to eq. (7.9). In principle, one would expect complete drying, i.e., $\theta \to 180°$, as $\varepsilon_{\mathrm{CO}} \to 0$. In Fig. 7.3a), θ versus ϵ_{CO} is plotted, which is more compatible with a drying transition as $\epsilon_{\mathrm{CO}} \to 0$.

7.3.2. Cutoff dependence

In MD simulations, the Lennard Jones interactions are usually truncated at some distance R_0 for computer time reasons. In the above simulations, the cut off radius was

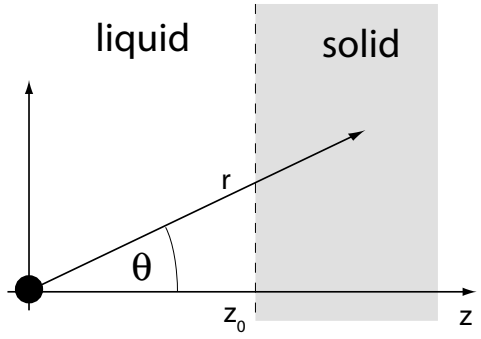

Figure 7.4.: Coordinate system for the calculation of the liquid/solid interaction energy in eq. (7.6).

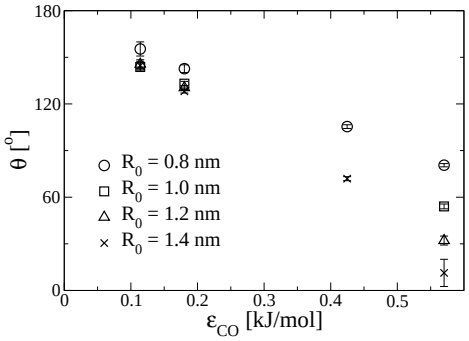

Figure 7.5.: Contact angles at the diamond surface for different liquid/solid interaction energies ϵ_{CO} and different cutoff radii R_0.

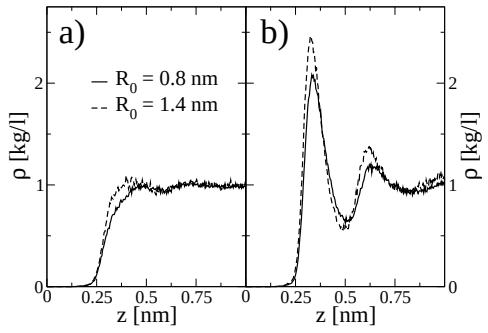

Figure 7.6.: Water density profiles at the diamond surface with $\epsilon_{\mathrm{CO}} = 0.11$ kJ/mol (a) and $\epsilon_{\mathrm{CO}} = 0.57$ kJ/mol (b) for two different cutoff radii R_0.

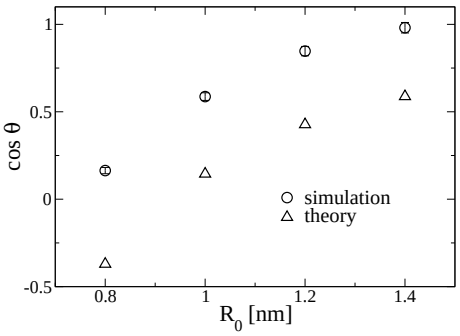

Figure 7.7.: Contact angles for one diamond surface with $\epsilon_{\mathrm{CO}} = 0.57$ kJ/mol with different cutoff radii. The plot shows the contact angles obtained from simulations (○) and from the calculation of H_{12} in eq. (7.11) (△). The surface tension of the liquid/vapor interface is obtained from simulations for both cases.

always $R_0 = 0.8$ nm. It turns out that this commonly used procedure largely influences the value for the contact angles. In Fig. 7.5, the contact angles at the diamond surface are shown for different liquid/solid interaction energies ϵ_{CO} and for different values of R_0. The liquid/vapor surface tension was also calculated for different cutoff radii by the simulation of a water film of 1807 water molecules in the NVT ensemble which yields a surface tension of 0.0543 N/m at $R_0 = 0.8$ nm. For the very hydrophobic surfaces, i.e. large contact angles, a variation in the cutoff radius does only lead to minor changes. In contrast, for the more hydrophilic surfaces, a change in the cutoff radius leads to substantial changes for the contact angles. Increasing the cutoff radius leads to smaller contact angles, i.e. less hydrophobic surfaces. A variation in R_0 also leads to changes in the density profiles, see Fig. 7.6. For lower cutoff radii, the water density at the surface decreases.

The dependence of the contact angle on the cutoff radius R_0 can be explained by the calculation of the liquid/solid surface tension. Therefore, a finite cutoff radius is included in the calculation for H_{12} in eq. (7.7). For a finite cutoff radius, the interaction energy of one single liquid molecule with the solid phase in eq. (7.6) now reads

$$v_{\mathrm{ls}}(z_0) = \begin{cases} 2\pi\rho_{\mathrm{s}} \int_{z_0}^{R_0} dr\ (r^2 - z_0 r) u(r) & \text{for} \quad 0 < z_0 < R_0 \\ 0 & \text{for} \quad z_0 > R_0. \end{cases} \tag{7.10}$$

The necessary work per surface area to separate the solid from the liquid is then given by

$$H_{12} = -\rho_{\mathrm{l}} \int_{\sigma'}^{R_0} dz_0\ v_{\mathrm{ls}}(z_0) = 2\pi\epsilon_{\mathrm{CO}}\rho_{\mathrm{s}}\rho_{\mathrm{l}} \left[\frac{1}{8} \left(\frac{15}{2} \right)^{1/3} - \left(\frac{\sigma}{R_0} \right)^2 + \mathcal{O}\left(\frac{\sigma}{R_0} \right)^8 \right] \tag{7.11}$$

for the intermolecular potential given in eq. (7.1). For the Lennard Jones potential, the lower integration boundary is given by $(\sigma'/\sigma) = (2/15)^{1/6}$ to leading order in σ/R_0. Compared to the result in the limit $R_0 \to \infty$, H_{12} decreases by 40 % if a cutoff value of $\sigma/R_0 = 0.3$ is used. Fig. 7.7 shows contact angles dependent on the cutoff radius for one diamond surface with $\epsilon_{\mathrm{CO}} = 0.57$ kJ/mol from simulations and from the evaluation of eq. (7.11). In the calculation, the bulk water and diamond densities are used for $\rho_{\mathrm{s,l}}$. Due to approximations made for the calculation of the surface tensions in eq. (7.11), the data do not coincide with those of the simulations. However, the qualitative dependence on the cutoff radius is similar for both data sets. An increase in the Lennard Jones cutoff leads to decreasing contact angles since the liquid/solid interaction energy increases due to the larger integration volume for large cutoff radii.

This strong dependence of the contact angle on R_0 leads to consequences for the parameters used in MD simulations. To correctly characterize and model surfaces in MD simulations, it is not sufficient to choose the Lennard Jones parameters σ and ϵ. For a consistent treatment of the liquid/solid interface, also the value for the cutoff radius has to be specified. For all subsequent simulations, a cutoff radius of $R_0 = 0.8$ nm is used.

8. Water slippage at hydrophobic surfaces

In the preceding chapter, the equilibrium properties of liquid/solid interfaces are discussed. In contrast, this chapter presents results for non-equilibrium flow situations. On the nanoscale, the hydrodynamic boundary condition at the liquid/solid interface is of particular importance for microfluidic applications [8, 9] or biological systems, such as the transport through membrane channels [25]. Due to the increasing surface to volume ratio, interfacial effects become crucial for small volumes. Applications are also found in the automobile industry. Mechanical components which are coated with hydrophobic, diamond like carbon exhibit very low friction properties [129, 130], which will lead to increased efficiencies.

Over the past years it has become clear, that the no-slip boundary condition, i.e. zero interfacial fluid velocity, does not necessarily hold at nanoscopic length scales [24, 131]. At hydrophobic surfaces, partial slip occurs which can be quantified by the slip length b. This length is defined via the gradient of the fluid velocity field $\mathbf{v}(z)$ parallel to the surface normal at the surface [131],

$$\left(|\mathbf{v}_0| - |\mathbf{v}|\right)_{z=z_0} \equiv b|(\partial\mathbf{v}/\partial z)_{z=z_0}|, \tag{8.1}$$

with the velocity $\mathbf{v}_0$ and position z_0 of the surface, see Fig. 8.1. Large slippage will amplify the flow rate for pressure driven flow, which enhances fluid transport in narrow channels. However, a considerable increase is only obtained if the slip length is comparable to the channel dimension. For electrically driven flow, even small slip lengths in the nanometer range lead to a considerable increase in flow [132]. Therefore, a profound understanding of the flow boundary condition at surfaces is necessary.

We use non-equilibrium Molecular Dynamics (NEMD) simulations to investigate the hydrodynamic boundary condition at a hydrophobic diamond surface. These simulations reveal slip lengths of only two nanometers on a hydrophobic diamond surface. The dependence of the slippage on surface hydrophobicity and surface roughness is examined and we find a quasi-universal relation between the slip length and the contact angle of the surface. Experiments yield slip lengths ranging from nanometers [133–136] up to micrometers [137, 138]. A collection of experimental and theoretical results can be found in [139]. A possible explanation of large slip measurements is the presence of a thin gas layer at the surface [29, 31]. In simulations of a Lennard-Jones liquid it was found that the slip length is only moderately increased under the presence of dissolved gas [140]. Using a realistic water model and gas parameters, we also observe only modest enhancement of the slippage. However, the presence of large gas nanobubbles on the surface [141–145] could significantly increase the slip length and could explain the measurement of large slip lengths.

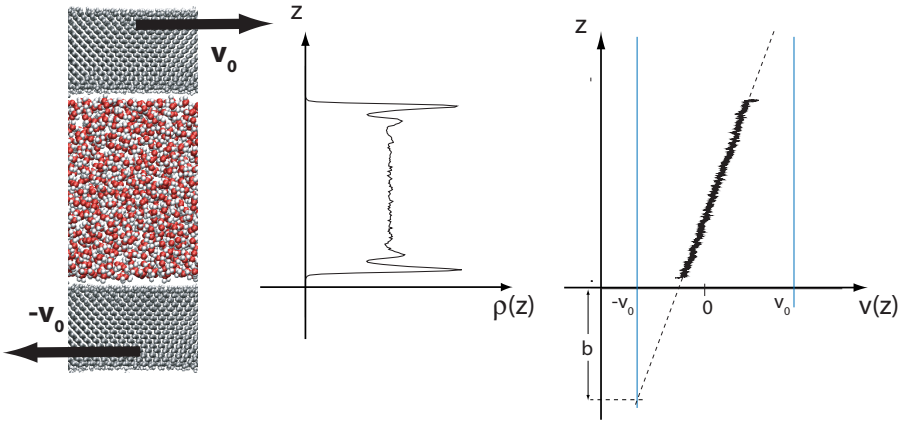

Figure 8.1.: Snapshot of the system with 4 nm gap size (left). Not shown is the second water film. The diamond slab is 1.5 nm thick and has 3.0×3.0 nm^2 lateral extension. In the middle, the water density profile is shown. The right figure shows the solvent velocity profile for $v_0 = 0.02$ nm/ps and the definition of the slip length b. The vertical lines denote the surface velocity $\pm v_0$.

8.1. Shear flow simulations

We use NEMD simulations to examine sheared water layers confined between hydrophobic, hydrogen-terminated diamond slabs. The system consists of two diamond blocks, described in section 7.2, which are separated by two SPC/E water slabs of thickness $Z \approx 4$ nm. This corresponds to roughly 1000 water molecules in each water film. In Fig. 8.1a), we show a snapshot of the simulation system, where only one of the water slabs is shown.

A Couette shear flow is induced by attaching harmonic springs with spring constants $k = 1000$ kJ mol^{-1} nm^{-2} to the upper and lower surface. The upper spring is pulled with a velocity of $v_{\text{surf}} = v_0$ in the x-direction and the lower spring with $v_{\text{surf}} = -v_0$ such that the net momentum vanishes. The movement of the diamond surfaces creates a linear velocity profile for the solvent flow, see Fig. 8.1b). Using the definition of a partial slip boundary condition at the position of the surface in eq. (8.1), the slip length b is obtained by extrapolating the velocity profile. For that purpose, the velocity profile is fitted to a linear function. The location of the surface at which the slip boundary condition is applied is defined by the center of the topmost layer of surface atoms. In the simulation cell, there are four identical liquid/solid interfaces, leading to four slip lengths. Error bars are given in terms of their standard deviation.

The systems are equilibrated for 200 ps and then subsequent production runs of up to 30 ns are performed. Several simulations with the same parameters are performed and all trajectories are used for the further analysis.

The used Berendsen weak-coupling thermostat is in principle critical for shear simulations and it needs to be demonstrated that it does not influence the resulting slip

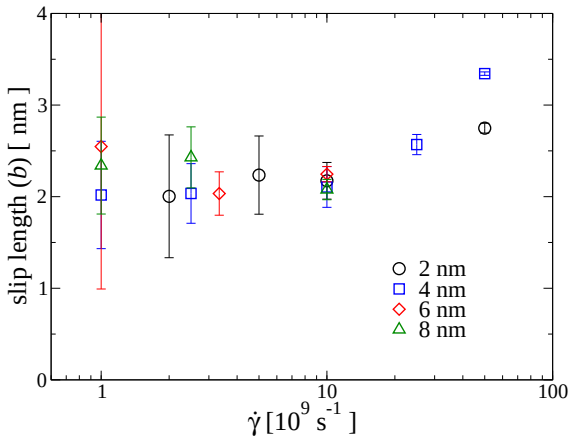

Figure 8.2.: Slip length b versus shear rate for different water film thicknesses at the diamond surface. The liquid/solid interaction energy is $\epsilon_{CO} = 0.4247$ kJ/mol, the standard value of the GROMOS forcefield.

lengths from shear flow simulations. This issue has been checked by performing two benchmark simulations, where a Berendsen thermostat with velocity scaling in all Cartesian directions and a Nose-Hoover thermostat with velocity scaling only in the y–direction are applied, during otherwise identical simulations [146]. We found no difference between these different simulation protocols.

8.2. Shear rate dependence

Since experimental shear rates are substantially lower than the rates used in MD simulations, a careful examination of the applied pulling velocities is necessary. Therefore, shear flow simulations for the diamond surface at different shear rates are performed, to rule out nonlinear artifacts. Fig. 8.2 shows slip lengths for different shear rates ranging from 10^9 up to $5 \cdot 10^{10}$ s^{-1}. Up to shear rates of 10^{10} s^{-1}, b is almost independent of the shear rate. To obtain reliable data at acceptable computational cost the value $\dot{\gamma} = 10^{10}$ s^{-1} is utilized for all subsequent shear simulations. The slip length for the diamond surface is only 2 nm. Fig. 8.2 also shows data for different water film thicknesses. The slip length is not sensitive to the width of the water film. Even for the thinnest water film of 2 nm, which corresponds to roughly five water layers, bulk like behavior for the flow is observed. For all other shear flow simulations, the water film thickness is 4 nm.

8.3. Slippage at different surfaces

The surface structure could be crucial for the amount of slippage. Therefore, 'nanorough' surfaces described in section 7.2 are used in the shear flow simulations. Besides the surface structure, also the liquid/solid interaction energy is varied to examine

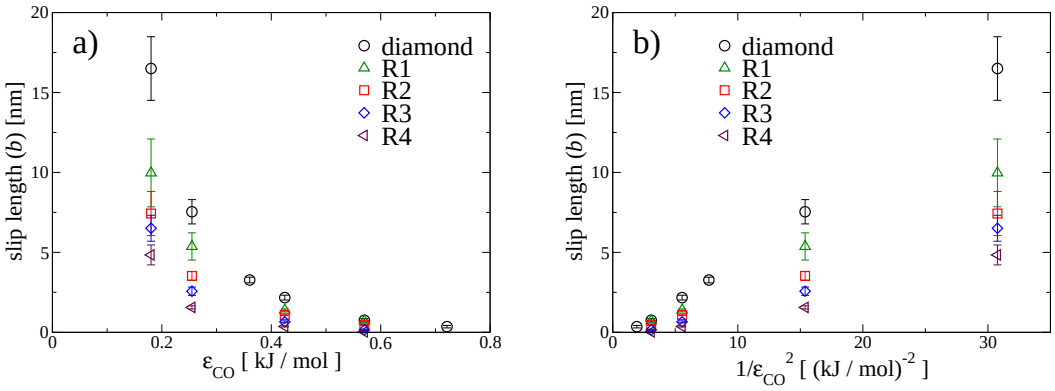

Figure 8.3.: Slip length b plotted versus the liquid/solid interaction energy ϵ_{CO} (a) and versus $1/\epsilon_{\mathrm{CO}}^{-2}$ (b). The graphs show data for the diamond and for the rough surfaces.

the slippage in dependence of the hydrophobicity of the surface. For decreasing interaction energies, i.e. more hydrophobic surfaces, the slip length is increasing, see Fig. 8.3a). Even for the lowest interaction energy, the slip length is below 20 nm. The slip length on the rough surfaces is always smaller than at the smooth diamond surface. At the roughest surface R_4, the slip length is smallest. Increasing surface roughness leads to smaller values for b, since the friction at the liquid/solid interface is enhanced by the stronger corrugation of the liquid/solid interaction potential. This can be understood in the limit of a perfectly smooth liquid/solid interaction potential. In this limit, the system is invariant under lateral translation, which would lead to an infinite slip length.

8.4. Slip length and contact angle

To rationalize the dependence of slippage in terms of the surface properties, especially on the interaction energy ϵ_{CO}, we follow an argument of Bocquet and Barrat [147, 148]. There, the slip length is determined via the friction at the liquid/solid interface. The friction, i.e. viscous force F per surface area A, exerted by the wall on the fluid is given by its viscosity η times its velocity gradient at the position of the surface,

$$\frac{F_x}{A} = \eta \left[\partial_z v_x(z = z_0)\right]. \tag{8.2}$$

Using eq. (8.1) an expression for the friction force per surface area is obtained (for simplicity, $v_0 \equiv 0$),

$$\frac{F_x}{A} = \frac{\eta}{b} v_x(z = z_0). \tag{8.3}$$

As for any dissipative mechanism, a Green-Kubo formula can be derived, leading to

$$\langle F_x \rangle_{\mathrm{NE}} = -\frac{v_x(z = z_0)}{k_{\mathrm{B}}T} \int_0^\infty dt\, \langle F_x(t) F_x(0) \rangle \tag{8.4}$$

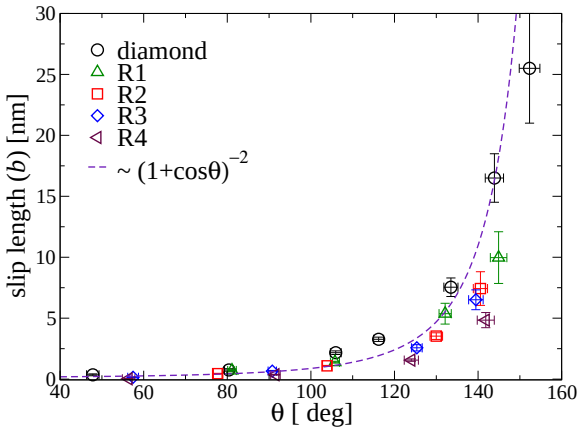

Figure 8.4.: Slip length versus contact angle for all considered surfaces and interaction parameters.

in the linear response regime. The subscript NE denotes the non equilibrium average for the situation of the sheared liquid. The autocorrelation function can be approximated by

$$\int_0^\infty dt\ \langle F_x(t)F_x(0)\rangle \approx \langle F_x^2\rangle \cdot \tau. \tag{8.5}$$

The diffusive timescale $\tau = \sigma^2/D$ is given by the diffusion constant D and the lateral length scale of the surface, σ. From dimensional arguments, $\langle F_x^2\rangle \propto (\epsilon_{\mathrm{CO}}/\sigma)^2$. Therefore, the slip length depends inverse quadratically on the interaction strength, $b \propto \epsilon_{\mathrm{CO}}^{-2}$. In Fig. 8.3b), we replot the slip length as a function of the inverse square of the interaction energy. Since the data points fall on a straight line for the different surfaces, the validity of the scaling considerations is confirmed. Making use of eq. (7.9), a simple relationship between the slip length and contact angle is obtained,

$$b \propto (1+\cos\theta)^{-2}. \tag{8.6}$$

Fig. 8.4 shows the data for the slip length, plotted versus the contact angle for all considered surfaces. The effects of roughness on b on the one hand and on θ on the other hand partially cancels out. Increasing roughness leads to decreasing slip lengths due to the enhanced friction. Since the liquid/solid contact area is increased on a rough surface, the liquid/solid interaction energy becomes larger which leads to decreasing contact angles. Despite the rough estimates leading to eq. (8.6), the simulation results follow nicely the predicted scaling. The dependence of the slip on the contact angle shows the same dependence also for different surface structures such as fcc(100) Lennard Jones surfaces or alkane chains [146]. This quasi-universal relation between contact angle and slippage is of particular interest, since the contact angle is an experimentally easily accessible quantity.

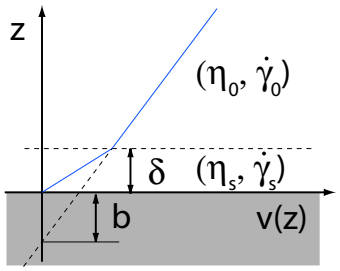

Figure 8.5.: A thin gas layer of viscosity η_s with thickness δ between the bulk liquid of viscosity η_0 and the solid (gray area) leads to an apparent slip length b. The slope $\partial_z v(z) = \dot{\gamma}(z)$ of the velocity profile (blue line) for the interfacial and bulk region is determined by the viscosities in the bulk and interfacial region, eq. (8.7).

8.5. Slippage and depletion length

An alternative theory for the slip length at the liquid/solid interface is based on the existence of a thin vapor layer with thickness δ between the solid and the liquid phase. The viscosity η_s of this layer is substantially lower than the bulk water viscosity η_0 which will lead to an apparent slip length b, see Fig. 8.5. Since the viscous stress $F/A = \eta(z)\partial_z v_x(z) = \eta(z)\dot{\gamma}(z)$ is constant in the system, the ratio of the viscosities is given by those of the velocity gradients in the two different regions,

$$\frac{\dot{\gamma}_0}{\dot{\gamma}_s} = \frac{\eta_s}{\eta_0}. \tag{8.7}$$

With the definition of the slip length in eq. (8.1), the fluid velocity at the gas/liquid boundary reads

$$v(z = \delta) = (\delta + b)\dot{\gamma}_0 = \delta\dot{\gamma}_s. \tag{8.8}$$

With eq. (8.7), this leads to an expression for the apparent slip length which is linearly dependent on the width of the vapor layer [29]

$$b = \delta(\eta_0/\eta_s - 1). \tag{8.9}$$

To test this prediction, we used two different definitions of the vapor layer width δ: (i) the position where the water density is half its bulk value and (ii) as an excess quantity for the density profile [127]

$$\delta = \int_0^\infty dz \left[1 - \rho_s(z)/\rho_s^b - \rho_l(z)/\rho_l^b\right]. \tag{8.10}$$

$\rho_{l,s}^b$ are the bulk densities of the liquid and solid phase. The depletion length can be directly calculated from the density profiles of the simulations. Since for the rough surfaces, the determination of the depletion length is difficult due to the ambiguity in the definition of the position of the liquid/solid interface, only data for the diamond and the two smoothest R_1 and R_2 surfaces are shown. For both definitions, we do not find a linear dependence of the slip length on the depletion width, see Fig. 8.6. Therefore we can not support this two-viscosity picture. Furthermore, the depletion length is less than a molecular diameter which makes the definition of an effective viscosity for such a thin layer difficult. Fig. 8.7 shows a snapshot of the liquid/solid interface together with the width of the depletion layer, defined by eq. (8.10).

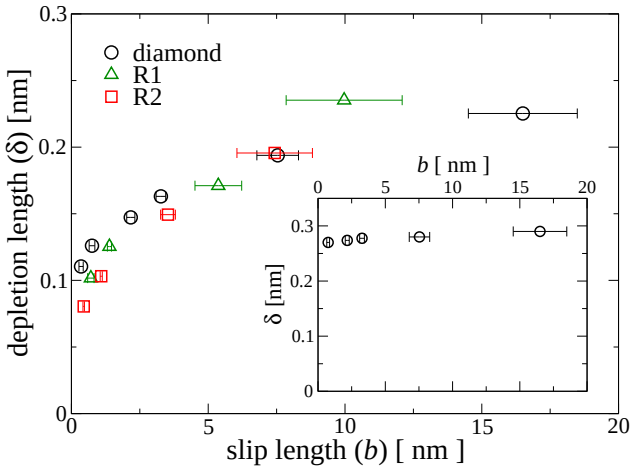

Figure 8.6.: Depletion length δ versus the slip length. The depletion width was determined using the definition (ii) given in eq. (8.10) and the criterion (i) where the water density is half its bulk value (inset).

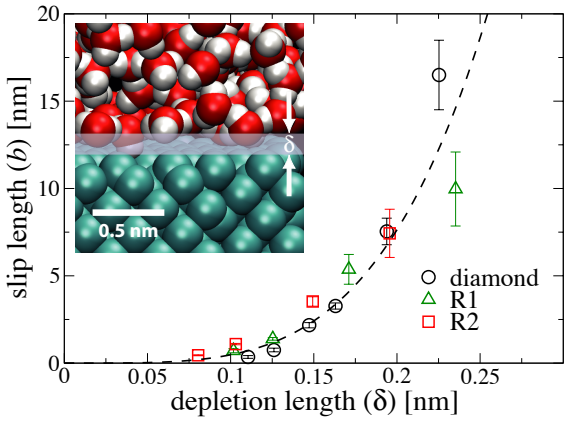

Figure 8.7.: Slip length in dependence of the depletion length for the diamond and rough surfaces. The depletion length is defined as an excess quantity of the density profile, given in eq. (8.10). The dashed line shows a fit for the diamond surface to $b \propto \delta^4$.

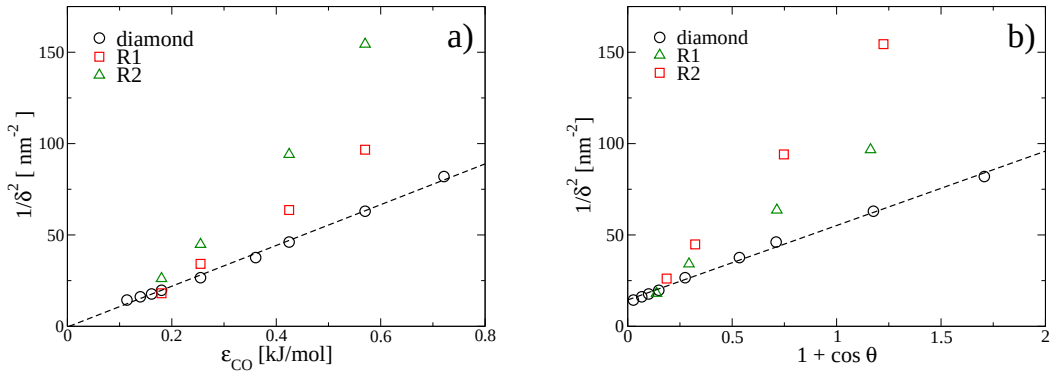

Figure 8.8.: Plot of the inverse square of the depletion length versus the liquid/solid interaction energy ϵ_{CO} (a) and versus the cosine of the contact angle (b). The depletion length is defined in eq. (8.10). The broken lines show a linear fit for the diamond data.

The dependence of the slip length on the depletion length in Fig. 8.7 is well described by the scaling relation $b \propto \delta^4$. In Fig. 8.8a), the depletion length in dependence of the liquid/solid interaction energy is plotted which suggests the scaling $\delta^{-2} \propto \epsilon_{\mathrm{CO}}$. Using eq. (7.9), the scaling of the depletion length with contact angle is obtained,

$$\delta^{-2} \propto 1 + \cos\theta \tag{8.11}$$

which is confirmed by the simulation data shown in Fig. 8.8b). With eq. (8.6), the quartic dependence of the slip length on the contact angle is obtained.

However, under the assumption of a vacuum layer of width δ between the solid and the liquid phase, the lower integration boundary in eq. (7.7) is given by δ which would lead to $H_{12} \propto \epsilon_{\mathrm{CO}}/\delta^2$. From Young's equation eq. (7.2) and from eq. (7.5) the scaling $1+\cos\theta \propto \epsilon_{CO}/\delta^2$ is obtained, in contradiction to the above considerations which led to eq. (8.11).

δ is rather a measure of the density depletion of the liquid from the surface than the width of a vacuum layer at the surface. Since eq. (7.8) was derived under the assumption of constant liquid density and neglecting interfacial entropy, this simple theory can not explain the dependence of the slippage on the depletion length. Thus, a full statistical treatment of the interface is necessary.

Even for contact angles of 140°, the slip is less than 20 nm, see Fig. 8.4, whereas recent experiments yield still larger slip lengths, for example 20 nm at a contact angle of 105° [136]. This disagreement could be explained by the strong dependence of the slip length on the depletion length. Compared to experiments for silanized surfaces, the simulations underestimate the depletion length typically by a few Angströms [29]. Furthermore, the depletion length increases if dissolved gas is present in the water film.

A	B	ϵ_{AB} [kJ/mol]	σ_{AB} [nm]
Ne	Ne	0.6398	0.3136
Ne	O_l	0.4951	0.3293
Ne	C	0.4213	0.3351
Ar	Ar	0.9964	0.3410
Ar	O_l	0.8049	0.3285
Ar	C	0.5257	0.3494
O_g	O_g	0.4016	0.3030
O_g	O_l	0.5110	0.3098
O_g	C	0.3338	0.3306

Table 8.1.: Lennard Jones parameters for the simulation of a water film with dissolved gas. The parameters for the noble gases are taken from the GROMOS forcefield, those for the oxygen gas from [149]. O_l denotes the oxygen of the water molecules, O_g that of the oxygen gas.

8.6. Dissolved gas

To examine the effect of dissolved gas particles in water, the same shear flow simulations with added gas particles in the water film for the diamond surface are performed. In each gap between the solid slabs, 10 gas particles are inserted. We examine different types of gas particles. Species X ($m_x = 12.01\ u$) interacts equally with all other atoms present in the system via a purely repulsive potential,

$$V_X(r) = 4\epsilon_X \left(\frac{\sigma_X}{r}\right)^{12} \tag{8.12}$$

with the $\sigma_X = 0.3581$ nm and $\epsilon_X = 0.2774$ kJ/mol, the Lennard Jones parameter of carbon.

Also, parameters from the GROMOS force field are used to model the noble gases Ne ($m_{Ne} = 20.18\ u$) and Ar ($m_{Ar} = 39.95\ u$). For the diatomic oxygen gas O_2 ($m_O = 16.00\ u$), the Lennard Jones parameters are the same as those used in Ref. [149]. The bond length between the two oxygen atoms is constraint to 1.21 Å. These gas particles interact via the Lennard-Jones potential in eq. (7.1) with the surface atoms and water molecules. The interaction parameters for all considered gas types are summarized in Tab. 8.1.

For the simulations with dissolved Argon gas and gas type X, the surface hydrophobicity is varied. Therefore, the Lennard Jones interaction energy of the surface atoms ϵ_{CC} is varied while the Lennard Jones diameter σ_{CC} is held fixed. For the simulations with Argon, all interaction energies involving the surface atoms are then recalculated by

$$\epsilon_{CAr} = \sqrt{\epsilon_{CC}\epsilon_{ArAr}} \qquad \text{and} \qquad \epsilon_{CO} = \sqrt{\epsilon_{CC}\epsilon_{OO}}. \tag{8.13}$$

For the simulations with gas type X, only the liquid/solid interaction energy ϵ_{CO} is varied, while the gas/solid interaction is unchanged. For the oxygen molecules and

neon atoms, only the diamond surface with the standard parameters for the carbon atoms are used. The simulation procedure and other parameters are identical to those described in section 8.1.

8.6.1. Gas adsorption

Fig. 8.9 shows the density profiles from the shear simulations. No difference in the density profiles is observed for equilibrium simulations. The densities are averaged over the four interfaces of the simulation cell. The gas atoms accumulate at the hydrophobic interface. A gas accumulation at hydrophobic surfaces was previously observed in MD simulations of Lennard Jones fluids [140] and in grand canonical Monte Carlo simulations with the SPC water model [149]. The density of neon, argon and oxygen gas at the interface is increased by a factor of roughly 20 - 60 compared to the density inside the water slab. The gas adsorption is restricted to one monolayer of gas particles, since there is only one narrow peak present in the density profiles shown in Fig. 8.9a). The density of the purely hydrophobic gas type X at the interface is increased by a factor of more than 150. All X atoms are mostly present on one surface and the formation of a big cluster of gas atoms can be seen in the simulations, see Fig. 8.10. This strong clustering is reflected in the shoulder of the X-density profile in Fig. 8.9a). The other gases do not exhibit such a clustering. Their densities are more or less equally distributed on the two slabs and no big cluster is observed in the simulations. A representative snapshot of one simulation with dissolved argon atoms is shown in Fig. 8.11.

A variation of the surface hydrophobicity does not lead to qualitative changes in the density profiles. The accumulation of Argon atoms is strongest at the most hydrophobic surface ($\epsilon_{CO} = 0.26$ kJ/mol). This effect is also observed for gas type X. This strong gas accumulation is not seen in simulations of dissolved gas between polar, hydrophilic surfaces. In Fig. 8.9 also the density profile of dissolved argon gas between two polar, hydrophilic surfaces is shown. The gas density at this surface is only twice the bulk value. The hydrophilic surface is covered with polar OH groups ($x_{OH} = 1/4$) and will be described in chapter 9. Although the gas particles Ne, Ar and O_2 are predominantly close to the interface, they are still free to desorb from the interface as can be seen in the snapshot shown in Fig. 8.11. The gas accumulation at the interface is not due to the Lennard Jones interaction between the surface and the gas atoms, since also the gas type X with the purely repulsive potential has an increased density at the surface. Rather, the water structure with its hydrogen bonding network is less perturbed if the gas particles are present at the interface than in the bulk liquid. Therefore, gas adsorption at a hydrophobic surface is energetically favorable.

As soon as the gas particle agglomerate, the question arises if the amount of gas is still solvable in water. For example, experimentally, a mole fraction of 0.25×10^{-4} Ar-Molecules (0.23×10^{-4} for O_2) is soluble in water at a partial gas pressure of 1 atm and $T = 298.15$ K [150]. In the simulations, the total pressure is fixed at 1 bar $\approx$ 1 atm. Since the partial pressure of water vapor at room temperature is roughly 0.02 atm, the partial gas pressure in the simulation is comparable to the experimental

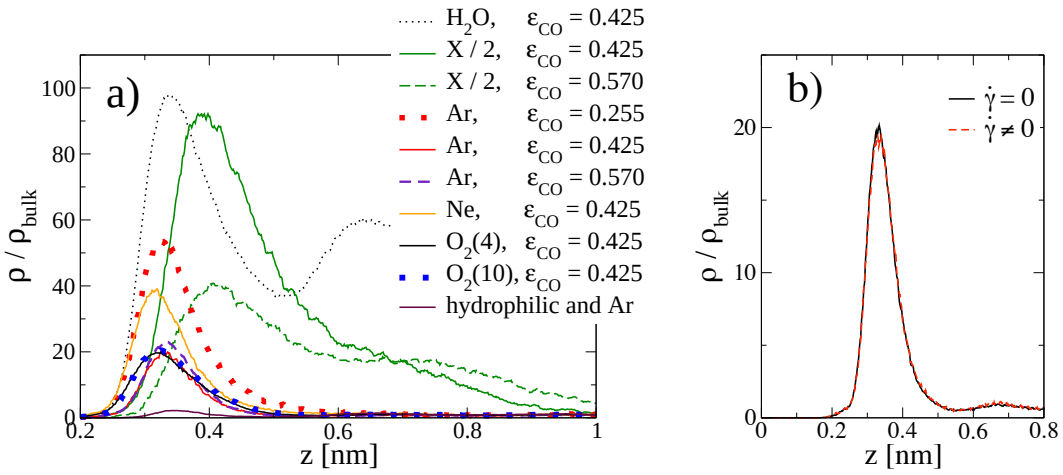

Figure 8.9.: a) Density profiles for different gas types at the diamond surface. The gas densities are scaled by their bulk concentrations. The center of the topmost carbon surface atoms is located at $z = 0$. The total amount of dissolved gas is ten gas particles per water slab, except for one simulation for O_2 with only four oxygen molecules per water slab. For Ar and X, also data for different surface hydrophobicities are shown. The density of the most hydrophobic gas type X is scaled by $\rho/2\rho_{\text{bulk}}$. For comparison, the water density profile (not normalized) without dissolved gas for the standard GROMOS parameter $\epsilon_{\text{CO}} = 0.425$ kJ/mol is also shown. Additionally, data for the simulation of dissolved argon gas between two hydrophilic surfaces is shown. The hydrophilic surface ($x_{\text{OH}} = 1/4$) bears polar OH groups and is described in chapter 9. In b), the density profiles from equilibrium ($\dot{\gamma} = 0$) and non-equilibrium ($\dot{\gamma} \neq 0$) simulations are shown for argon gas and $\epsilon_{\text{CO}} = 0.4247$ kJ/mol. The concentrations are scaled by the bulk concentration for ($\dot{\gamma} \neq 0$). The density profiles are not sensitive to shear flow.

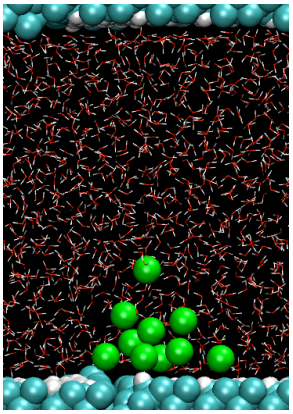

Figure 8.10.: Snapshot of a simulation for gas type X (green atoms) at the diamond surface ($\epsilon_{CO} = 0.57$ kJ/mol). The gas molecules form one big cluster

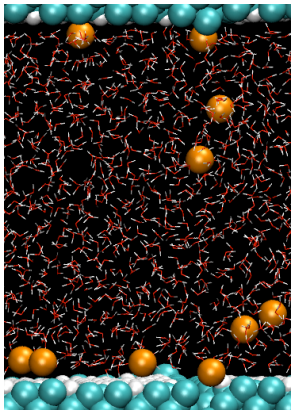

Figure 8.11.: Snapshot for the simulation of the diamond surface ($\epsilon_{CO} = 0.4247$ kJ/mol) with Argon gas (orange atoms).

situation, $p_{gas} \approx (1 - 0.02)$ atm ≈ 1 atm. From the density profiles, it is obtained, that the value of the mole fraction of dissolved argon gas in the bulk liquid is much higher than the experimental solubility with a value of about 5×10^{-3}, similar to the mole fraction of 4×10^{-3} of the oxygen gas. However, no phase separation is observed in the simulations. At room temperature and an ambient pressure of 1 bar, the distance between particles in the gas phase is roughly 3 nm, thus comparable to the overall size of the simulation box. Since the particle number is held constant in the simulations, phase separation would lead to a huge increase in the liquid/gas interface in the simulations which is prevented by the high surface tension of liquid water. Nevertheless, reducing the amount of gas particles in the computer simulations does not lead to qualitative changes. This issue has been checked by one simulation run with only four oxygen molecules per water gap. In the normalized density profiles in Fig. 8.9a), no difference is seen between the two different oxygen concentrations.

8.6.2. Stability of gas clusters

For gas type X which has a purely repulsive interaction potential, large clusters of gas atoms are observed, Fig. 8.10. The question arises how these cluster can be stable, since their gas pressure is significantly higher than the outer pressure of $p_0 = 1$ bar. For hard spheres with diameter σ and for semi spherical cluster shape, the gas pressure is given by

$$p_g \approx k_B T \frac{N}{V} \left[1 + N \left(\frac{\sigma}{R} \right)^3 \right] \tag{8.14}$$

with the volume $V = 2\pi R^3/3$ and the particle number N of the cluster. From the snapshot in Fig. 8.10, the radius of the bubble is $R \sim 0.7$ nm. With the particle diameter $\sigma_X = 0.36$ nm, this leads to a pressure of 1.3×10^8 Pa $\approx 10^3\ p_0$. This

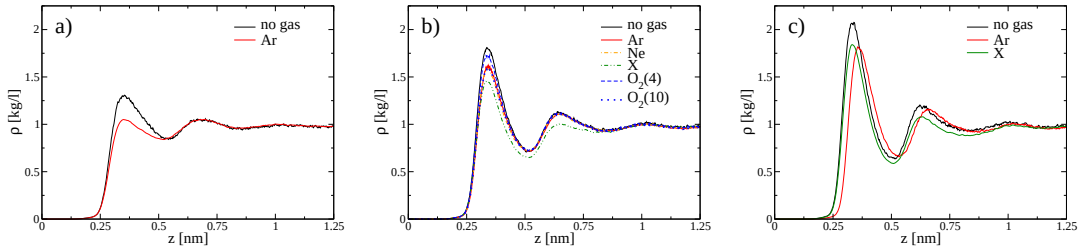

Figure 8.12.: Water density profiles with and without dissolved gas at the diamond surface. The topmost layer of the surface atoms is located at $z = 0$. The water/solid interaction energy is varied, $\epsilon_{CO} = 0.255$ kJ/mol, 0.425 kJ/mol and 0.570 kJ/mol, from a)-c). The contact angles for these interaction energies correspond to $\theta = 136°,\ 106°$, and 80°.

pressure has to be counterbalanced by the Laplace pressure $p_L = 2\gamma_{lv}/R$, which is due to the liquid/vapor surface tension,

$$p_L + p_0 = p_G. \tag{8.15}$$

With the liquid/vapor surface tension from the simulations of $\gamma_{lv} \sim 0.05$ N/m, the Laplace pressure $p_L \sim 1.5 \times 10^8$ Pa is similar to the gas pressure inside the bubble. The bubble will only be stable, if it experiences a restoring force for small fluctuations in R around its equilibrium value R_e. This criterion yields

$$\begin{aligned} 0 &< \left[\frac{d(p_L + p_0 - p_G)}{dR}\right]_{R=R_e} \\ &= -\frac{2\gamma_{lv}}{R_e^2} + \frac{3}{R_e} k_B T \frac{N}{V}\left[1 + N\left(\frac{\sigma}{R_e}\right)^3\right] + 3k_B T \frac{N^2}{V R_e}\left(\frac{\sigma}{R_e}\right)^3 \\ &= \frac{2p_G}{R_e} + 3k_B T \frac{N^2}{V R_e}\left(\frac{\sigma}{R_e}\right)^3 \end{aligned} \tag{8.16}$$

where eq. (8.14) and $p_L(R = R_e) \approx p_G(R = R_e)$ have been used. Since the gas pressure for particles with a purely repulsive interaction potential is always positive, the inequality shown above is always fulfilled. Thus the clusters observed in the simulations are mechanically stable.

Experimentally observed nanobubbles does not have a semi spherical shape but have much larger diameters than bubble heights [141]. This leads to a smaller curvature and therefore significantly reduces the Laplace pressure which leads to an decrease of the gas density inside the bubble. Despite the mechanical stability of these bubbles, their thermodynamic stability is still under debate [30] and deserves a thorough examination.

8.6.3. Dissolved gas and slip length

Due to the accumulation of gas particles at the surface, the interfacial water density decreases, see Fig. 8.12. This decrease in water density is small and comparable for

gas	ϵ_{CO} [kJ/mol]	b_{gas} [nm]	b_0 [nm]
Ar	0.255	8.92 ± 2.12	7.54 ± 0.76
X	0.425	2.69 ± 0.18	2.17 ± 0.15
Ne	0.425	2.53 ± 0.10	2.17 ± 0.15
Ar	0.425	2.77 ± 0.55	2.17 ± 0.15
$O_2(10)$	0.425	2.61 ± 0.10	2.17 ± 0.15
$O_2(4)$	0.425	2.57 ± 0.24	2.17 ± 0.15
X	0.570	1.19 ± 0.19	0.75 ± 0.10
Ar	0.570	1.42 ± 0.04	0.75 ± 0.10

Table 8.2.: Slip lengths for shear flow simulations with dissolved gas (b_{gas}) for the hydrophobic diamond surface. The standard GROMOS parameter for the carbon water interaction energy corresponds to $\epsilon_{CO} = 0.425$ kJ/mol. For comparison, also the results for the simulations without gas are shown (b_0).

all considered gases. The purely repulsive gas X leads to slightly bigger changes in the water density. On the diamond surface, the adsorption of the gas particles always enhances the slip length only slightly. The largest relative change in slip length b with and without gas is seen for the highest liquid/solid interaction energy. There, the slip length roughly doubles when Ar atoms are present.

Dissolved gas only moderately amplifies the slip length which is still in the range of a few nanometer in our simulations. Thus, large slip measurements are not caused by surface adsorbed gas layers. However, experimental measurements suggest the formation of gas-nanobubbles at the liquid/solid interface [141–145]. The lateral dimension of these bubbles is in the order of 100 nm, with a height of several nanometers which could significantly enlarge the slip length. These gas cavities are much larger than the used simulation box and can not be observed in our simulations. The presence of such nanobubbles could lead to much larger values for the slip length than found in this study.

9. Water at hydrophilic surfaces

In the previous chapters, the dynamics and structure of liquid water at non polar, hydrophobic interfaces is discussed for equilibrium and non-equilibrium situations. Compared to hydrophobic substrates, hydrophilic surfaces are much more abundant in nature, with examples ranging from biological membranes to metallic surfaces, which attract the polar water molecules via induced image charges. In the following sections, water properties at hydrophilic, polar interfaces are examined.

At hydrophobic surfaces, the water molecules experience a loss of hydrogen bonding compared to the bulk configuration, which leads to a decrease in internal energy. At polar, hydrophilic surfaces, interfacial water molecules can form hydrogen bonds with polar surface groups, which can lead to even stronger liquid/solid interactions compared to the bulk liquid interaction. Some hydrophilic surfaces show complete wetting, which means that the contact angle can be as low as zero degrees.

Computer simulation studies show, that although the water density profiles for hydrophilic and hydrophobic surfaces are comparable, the diffusion of single water molecules is decelerated at hydrophilic interfaces [151]. However, in these studies it was found that the residence time of water molecules at these surfaces is only weakly sensitive to the surface hydrophilicity. In our study, we can not confirm this counterintuitive result. The residence time at hydrophilic, polar surfaces of the water molecules is found to be roughly twice as large as at a hydrophobic surface. The diffusion of the water molecules in the interfacial layer is slowed down compared to the diffusion in bulk water. At the hydrophilic surfaces, this effect is stronger compared to the non polar surface. Due to the polar surface groups, the water molecules are stronger attracted to the hydrophilic surface.

This strong liquid/solid interaction also influences the viscosity of the interfacial region. Experiments report on viscosities for strong confined water between mica surfaces, which are comparable to the bulk viscosity [152, 153]. These findings are also confirmed by computer simulations for thin water films. Only sub-nanometer confinement leads to an increase in viscosity of approximately 80 times the bulk viscosity [154]. Other experiments and simulation studies report on a strong increase in viscosity of several orders of magnitude for highly confined water films [36, 37, 155]. Also, the structure of water at hydrophilic surfaces is under debate. Spectroscopy experiments and computer simulations find an ice-like structure of thin water films [33–35, 156–158]. These crystal like structures are identified via a sharp drop in the diffusion constant and via a substantially increased shear viscosity. Also, these crystal-like phases can sustain shear stresses. At hydrophobic interfaces, this ice like water structure is not observed.

To clarify the structure and properties of water at hydrophilic surfaces, we perform MD simulations of water at polar, hydrophilic surfaces. In non equilibrium shear

flow simulations, the shear viscosity profile of interfacial water is obtained from the fluid velocity profiles. By this method we are able to locally probe the shear viscosity of water close to interfaces without effects stemming from a strong confinement of the water film. In contrast to hydrophobic surfaces, we find an increase in the viscosity of interfacial water at hydrophilic surfaces. This increase is stronger at more hydrophilic surfaces with an interfacial viscosity which is roughly four times the bulk value. Therefore, we do not observe a drastic increase in viscosity at hydrophilic surfaces. Also, the diffusion at hydrophilic interfaces is only moderately slower compared to the hydrophobic surfaces. These results do not support a solid-like structure or tightly bound layer of interfacial water at hydrophilic interfaces.

9.1. Static properties

In the MD simulations, we use two different hydrophilic surfaces with polar surface groups. The surfaces are constructed out of the H-terminated diamond surface, described in section 7.2. Every forth ($x_{\mathrm{OH}} = 1/4$) or eighth ($x_{\mathrm{OH}} = 1/8$) surface carbon atom is substituted by an C-O-H group with angular and torsional force potentials. The bond angle at the oxygen atom is 108°. The partial charges are set to $q_O = -0.674\ e$, $q_H = 0.408\ e$ and $q_C = 0.266\ e$. These parameters are taken from the GROMOS96 forcefield for serine. Fig. 9.1 shows the top view of the two hydrophilic surfaces. As in the two preceding chapters, we use the SPC/E water model and the GROMOS forcefield. The Lennard Jones parameters of the atoms are given in Tab. 7.1 and the simulation parameters are the same as in section 7.1.

Compared to the hydrophobic diamond, the water molecules are attracted more strongly to the surface. As can be seen in the density profiles in Fig. 9.2, the liquid is closer to the surface compared to the hydrophobic interface. Also, the first water peak is more pronounced and has a smaller width for the hydrophilic surfaces. Only minor differences are seen between the two different hydrophilic surfaces. For the larger OH density, the first water peak is slightly higher and closer to the the interface. The hydrophilic surfaces exhibit complete wetting, meaning that the contact angle is 0°.

9.2. Interfacial shear viscosity

To examine the shear viscosity of interfacial water at hydrophilic interfaces, non-equilibrium molecular dynamic simulations are performed. The simulation system consists of two solid slabs with distance $Z \approx 4$ nm. The gap is filled with water and the two surfaces are pulled with velocities $v_0 = 0.02$ nm/ps in opposite directions in the same way as described in section 8.1.

The velocity profiles, Fig. 9.3, differ qualitatively from those obtained for the hydrophobic surfaces: close to the surface, the gradient of the velocity profile is smaller than in the middle of the water gap. In contrast, the gradient of the velocity profiles at the hydrophobic surfaces is constant, even close to the interface, see Fig. 8.1. At the hydrophilic surface, the water molecules at the interface are dragged along with the surface. The region over which this sticking of water molecules occurs is roughly the

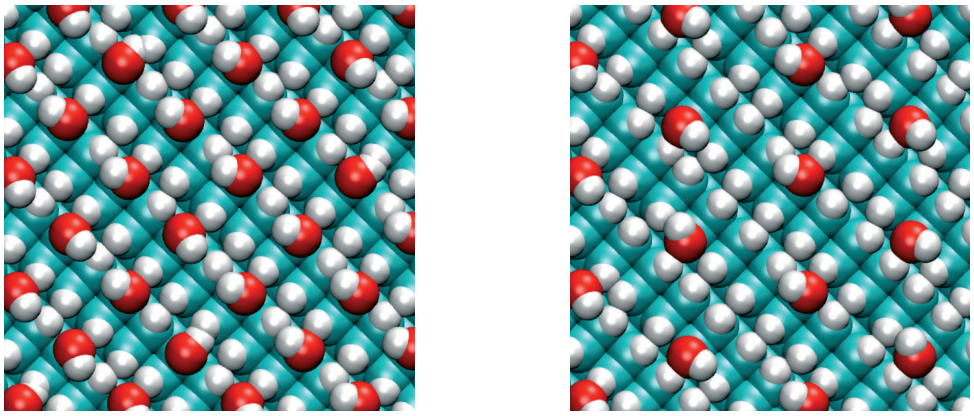

Figure 9.1.: Top view of the hydrophilic diamond surface surface with $x_{\mathrm{OH}} = 1/4$ (left) and $x_{\mathrm{OH}} = 1/8$ (right).

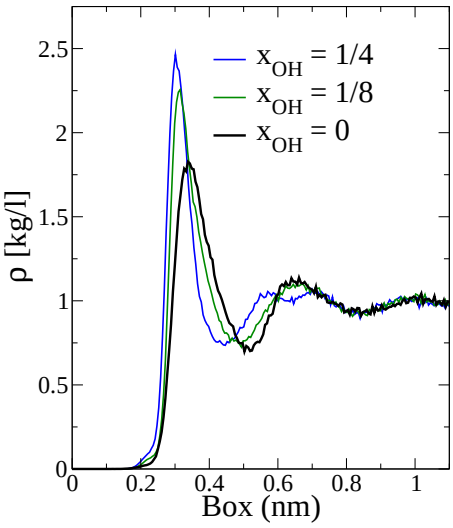

Figure 9.2.: Density profiles for the two hydrophilic surfaces with $x_{OH} = 1/4$ and $x_{OH} = 1/8$. For comparison, the density profile of the hydrophobic diamond is also shown. The top layer of carbon atoms is located at $z = 0$.

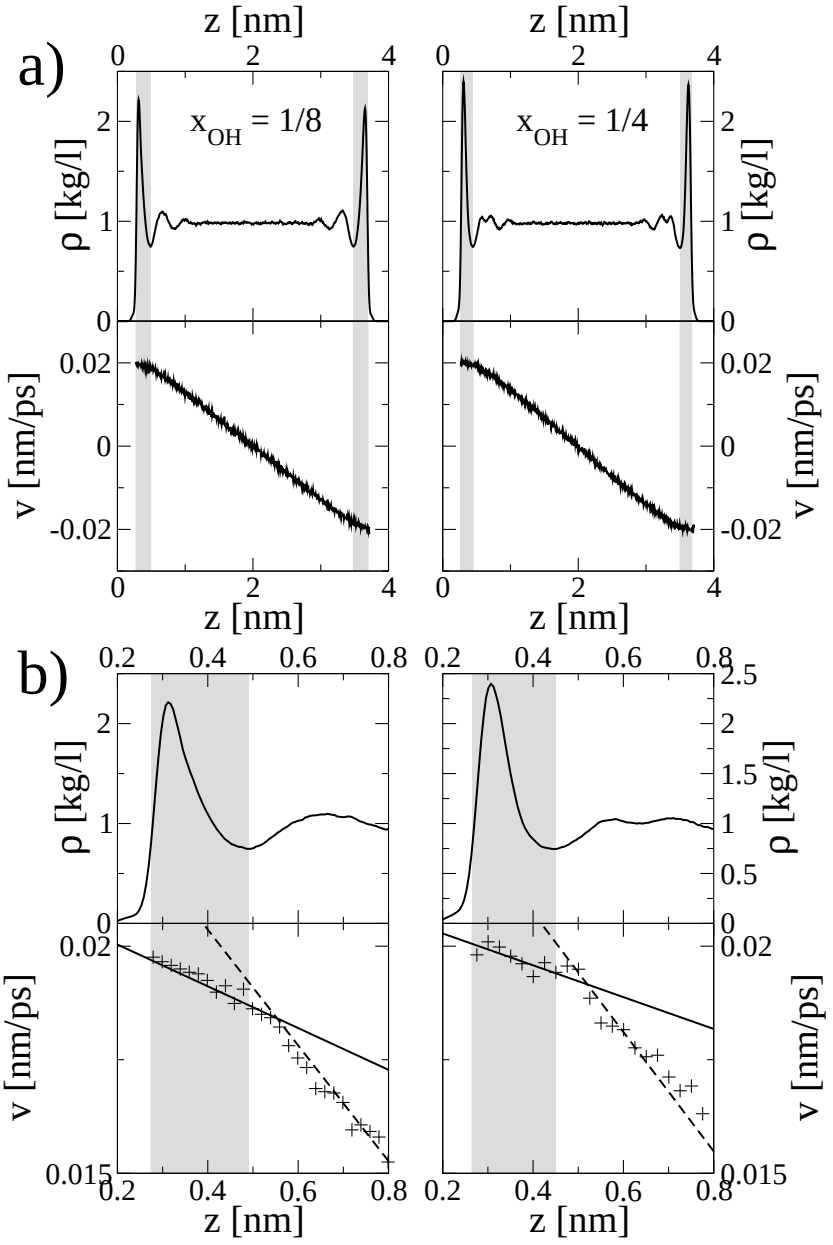

Figure 9.3.: Water density profiles (top row) and velocity profiles (bottom row) for the the hydrophilic surfaces with $x_{OH} = 1/8$ (left) and $x_{OH} = 1/4$ (right). Fig. b) shows the density profiles and more averaged velocity profiles (+) close to the surface. The fit functions for the velocity profile in the peak region and in the bulk region are shown as solid and broken lines. The gray shaded areas give the extent of the peak region.

x_{OH}	$\dot{\gamma}_0$ [1/ns]	$\dot{\gamma}_s$ [1/ns]	η_s/η_0	slip length [nm]
1/4	13.4	3.6 ± 0.8	3.7 ± 0.9	-0.32 ± 0.01
1/8	12.8	5.9 ± 1.0	2.2 ± 0.4	-0.29 ± 0.01

Table 9.1.: Shear rate and viscosities for the mid- and interfacial region and the corresponding slip length, obtained from the velocity profiles of the non-equilibrium MD simulations.

extent of the first water layer. This feature is due to the strong interaction between the hydroxyl surface groups and the water molecules. These findings are in agreement with velocity profiles obtained from simulations of sheared water films between mica surfaces [159].

Since the shear viscosity is linearly dependent on the inverse of the velocity gradient, it is possible to define two different viscosities in the system. One in the surface region (η_s) and the other one in the bulk region (η_0), see also Fig. 8.5. To obtain the shear rates in the two regions, the velocity profile is fitted to a linear function in the region of the first water peak and in between. The fit region for the velocity profile of the interfacial layer starts at the position where the water density is for the first time equal to the density at the first density minimum and ends at the position of the first water density minimum, shown as the gray shaded areas in Fig. 9.3. This definition is used since the velocity profile shows big fluctuations close to the surface. Due to the small amount of water molecules in the very proximity of the solid surface, the statistics are not sufficient to obtain a smooth velocity profile. The ratio of the two viscosities is then determined by the ratio of the velocity gradients in the interfacial ($\dot{\gamma}_s$) and bulk ($\dot{\gamma}_0$) region, eq. (8.7).

In Tab. 9.1, the numerical values of the interfacial viscosities are shown. For the more hydrophilic surface ($x_{OH} = 1/4$), the interfacial viscosity is larger by a factor of four compared to the bulk viscosity. The less hydrophilic surface exhibits a similar interfacial viscosity, roughly twice the bulk value. For both surfaces, the change in viscosity is moderate and does not support an ice-like interfacial water structure.

As for the hydrophobic surfaces, eq. (8.1) can be used to define a slip length b. Therefore, the velocity profile is fitted in the bulk region to a linear function and extrapolated. By definition, the bulk region is ranging from the first to the last minimum of the water density profile, which is depicted as the white region in between the gray shaded areas in Fig. 9.3a). The location of the slip boundary is defined as the center of the oxygen atoms of the OH surface groups. This procedure leads to a negative slip length of roughly 0.3 nm, see Tab. 9.1. This would correspond to the situation of a velocity profile which is linear in the mid region and constant over a length of 0.3 nm from the surfaces. For constant viscosities in the bulk and interfacial region, eqs. (8.7, 8.8) can be used to determine the ratio of the two viscosities. However, since the viscosity will be a continuous function of the distance from the surface and the definition of the exact width δ of the surface layer is difficult, this procedure is not useful for the determination of the interfacial viscosity.

From the velocity profiles, only the ratio between the interfacial and the bulk viscosity can be calculated. For the explicit determination of the viscosities, the force acting on the diamond slabs is needed. In the simulation, the two solid slabs are attached to harmonic springs which are pulled with constant velocities $\pm v_0$. From the average displacement of the slabs from the minimum of the spring potential, the average force on the slabs can be directly read of. The shear viscosity is given by

$$\sigma_{xz} = \frac{F}{A} = \eta \partial_z v_x = \eta \dot{\gamma} \tag{9.1}$$

and relates the stress tensor σ_{xz} to the gradient of the velocity profile with the associated shear rate $\dot{\gamma} = \partial_z v_x$. F denotes the viscous force from the liquid, acting on the slabs with surface area A. Since in the simulation cell two water films are present, the viscosity is given by

$$\eta_0 = \frac{F_i/2}{A\dot{\gamma}_0} \qquad \text{and} \qquad \eta_s = \frac{F_i/2}{A\dot{\gamma}_s} \tag{9.2}$$

with the average forces F_i, $(i = 1, 2)$ on the two slabs. From the shear rate, obtained from the velocity profiles, and the average force measured in the simulations, the viscosities given in Tab. 9.2 are obtained from the above equations.

The viscosity η_0 in the inner region of the water film is similar for the hydrophilic and hydrophobic surfaces. The moderate confinement of 4 nm is not large enough to lead to strong deviations from the bulk viscosities, since the values for the bulk viscosity of the water film are in good agreement to the literature value $\eta = 0.642$ cp [160] for the SPC/E water model, obtained in non equilibrium simulations. The SPC/E water model still underestimates the viscosity of real water, $\eta = 0.851$ cp [161].

Since the used shear rates $\dot{\gamma} \sim 10^{10}$ s^{-1} are much larger than those typically used in experiments, it is crucial to check if the linear response regime is reached. We account for this issue by performing two benchmark simulations with double and half of the diamond pulling speed. Since neither the measured bulk viscosities nor the slip length changed with different pulling speed, see Tab. 9.2, we infer that the system is still in the linear response regime.

9.3. Diffusion

The viscosity of a liquid directly affects the diffusion constant for a particle with radius a, which is given by the Stokes-Einstein relation $D = k_\mathrm{B}T/6\pi\eta a$. Diffusion constants are calculated measuring the mean square displacement or from the velocity autocorrelation function. This leads to difficulties for the determination of a local diffusion constant inside a small layer, since the particles will rapidly diffuse out of the considered slab. Another route to estimate diffusion constants perpendicular to a certain liquid layer is the examination of the correlation for a function $f(z)$ which is unity if the particle is inside the layer and zero otherwise.

$$f(z) = \begin{cases} 1 & \text{if } z_0 < z < z_0 + \Delta z \\ 0 & \text{else} \end{cases} \tag{9.3}$$

x_{OH}	v_0 [ps/nm]	η_0 [10^{-3} N s /m^2]	η_s [10^{-3} N s /m^2]
1/4	0.02	0.73 ± 0.03	2.7 ± 0.7
1/8	0.02	0.71 ± 0.01	1.5 ± 0.3
0	0.02	0.66 ± 0.06	-
x_{OH}	v_0 [ps/nm]	η_0 [10^{-3} N s /m^2]	b [nm]
1/4	0.01	0.71 ± 0.03	-0.31 ± 0.01
1/4	0.04	0.722 ± 0.005	-0.317 ± 0.004

Table 9.2.: Simulation results for the viscosities calculated by means of eq. (9.2). The errors of the viscosities are calculated from the uncertainties of the measured spring force and of the shear rate. Also the results of two benchmark simulations at half and double pulling speed are shown. The interfacial viscosity is not calculated for these simulation runs. Due to the shorter simulation run, the velocity profile can not be determined with the necessary accuracy.

The autocorrelation function (ACF) of $f(z)$ is then given by

$$C(t) \equiv \mathcal{N}^{-1} \int dz \int dz'\, p(z,z',t) f(z) f(z') \rho_0(z'), \tag{9.4}$$

with the probability $p(z,z',t)$ that a particle is at z at time t, given that it was at z' at $t=0$. The normalization constant $\mathcal{N}$ assures that $C(0)=1$. $p(z,z',t)$ is the solution of the well known one dimensional diffusion equation for a particle in an external potential $W(z)$,

$$\partial_t p(z,z',t) = \partial_z \left\{ D(z) \left[\frac{1}{k_{\mathrm{B}}T} (\partial_z W(z)) + \partial_z \right] p(z,z',t) \right\} \tag{9.5}$$

$$p(z,z',0) = \delta(z-z'). \tag{9.6}$$

For bulk water with zero external potential and position independent diffusion constant D, the solution is given by

$$p(z,z',t) = (4\pi D t)^{-1/2} \exp\left(-\frac{(z-z')^2}{4Dt} \right) \tag{9.7}$$

with the boundary condition $p(z,z',t) \to 0$ for $|z-z'| \to \infty$. Since for bulk water, the density $\rho_0(z)$ is constant, the autocorrelation function in eq. (9.4) is given by

$$C(t) \approx \int_{z_0}^{z_0+\Delta z} dz \int_{z_0}^{z_0+\Delta z} dz' \left[4\pi D t (\Delta z)^2 \right]^{-1/2} \left(1 - \frac{(z-z')^2}{4Dt} \right) \approx \frac{\Delta z}{\sqrt{4\pi D t}}. \tag{9.8}$$

for long times $t \gg (\Delta z)^2/D$. The above equation is compared to simulation results for an NP_zT ensemble of 6000 water molecules in a $3 \times 3 \times 20.6$ nm^3 box. As for the other simulations, the system is coupled to a pressure of 1 bar and to a temperature of 300 K. The obtained autocorrelation functions in Fig. 9.4 are then fitted to $C(t) =$

Δz	D [nm^2/ns]
0.1	2.65
0.2	2.75
0.4	2.84
1.0	2.87

Table 9.3.: Diffusion constants for bulk water, obtained from a fit of the ACF to $C(t) = a_0 + a_1 t^{-1/2}$. The ACF is fitted in the region where the function shows power law behavior.

$a_0 + a_1 t^{-1/2}$. The diffusion constant is then determined to be $D = (\Delta z)^2/(4\pi a_1^2)$. This procedure yield diffusion constants for bulk water of $2.65 - 2.87$ nm^2/ns, see Tab. 9.3. These values are in good agreement with other publications: for the SPC/E water model, the diffusion constant was determined to be $D = 2.70 - 2.79$ nm^2/ns [162]. Experiments on the self diffusion of real water yield a value of 2.30 nm^2/ns at 298 K [163, 164]. Although the obtained diffusion constants are reasonable, one has to be concerned about a few issues, when estimating the diffusion constant by means of eq. (9.8).

Since the height Z of the simulation box is finite, $C(t)$ does not decay to zero but $C(t) \to (\Delta z)/Z$ for $t \to \infty$. For long times, the probability density is homogeneous across the box, $p(z, z', t) \to 1/Z$ for $t \to \infty$. Then

$$C(t \to \infty) = \frac{\int_{z_0}^{z_0+\Delta z} dz \int_{z_0}^{z_0+\Delta z} dz' \; (1/Z_{Box})}{\int_{z_0}^{z_0+\Delta z} dz \int_{z_0}^{z_0+\Delta z} dz' \; \delta(z - z')} = \frac{\Delta z}{Z_{Box}}. \tag{9.9}$$

The timescale on which equilibrium is reached inside the box is given by $\tau_D \sim Z^2/D$. For a 20 nm long box, this time is about 100 ns, thus much longer than the simulation duration. Also, eq. (9.7) is only an approximation for the real solution, since periodic boundary conditions are used in the simulation. Nevertheless, as long as the considered layer is small compared to the overall box size, these effects are only small corrections.

For water molecules close to the solid/liquid interface, the solution of the diffusion equation, eq. (9.5), is much more complicated. Generally, the liquid particles will experience a non zero surface potential $W(z)$ and the mobility of a single water molecule will depend on its distance from the surface. Due to the symmetry breaking of the interface, the diffusion tensor is anisotropic with different components for the lateral and the perpendicular direction with respect to the interface. Simulations have shown that the water molecules are more mobile along the lateral direction [151]. More sophisticated models are necessary to calculate the diffusion constant in the interfacial layer under the presence of a surface potential [165]. As a crude approximation, the solution of the diffusion equation in front of an interface for a position independent diffusion constant and zero external potential is considered. Since there is no flux of particles across the interface, the first derivative of the probability distribution must be zero at the location of the surface, $z = 0$. Then, the solution of eq. (9.5) is given

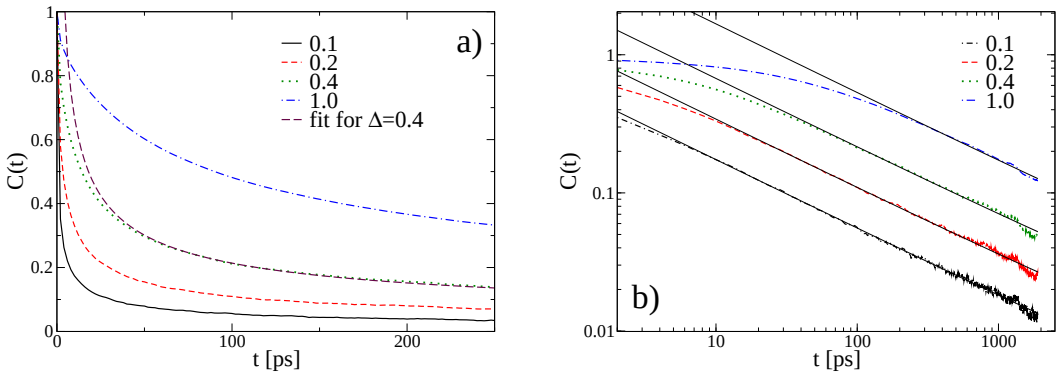

Figure 9.4.: Autocorrelation functions for bulk water for different layer thicknesses Δz with linear (a) and logarithmic scale (b). The legends give the width of the considered layer in nanometer. In the linear plot, also one fit function for $\Delta z = 0.4$ nm is shown, in the right plot, all fit functions are shown. The depicted fit functions are obtained from fitting the ACF in a region where the power law behavior is best. The fits lead to the data shown in Tab. 9.3.

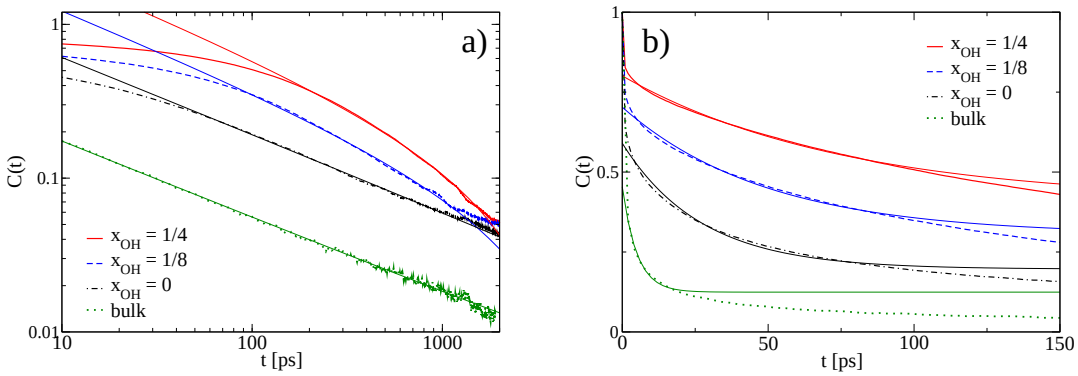

Figure 9.5.: ACFs for water at the hydrophilic and hydrophobic surfaces inside a $\Delta z = 0.1$ nm wide region, centered at the first water peak. Also, the ACF for bulk water with a slab thickness of $\Delta z = 0.1$ nm is shown. Fig. a) shows the ACFs together with the fitfunctions $C(t) = a_0 + a_1/\sqrt{t}$. In Fig. b) the ACFs and the exponential fitfunctions $C(t) = \exp(-t/\tau) + a_0$ are shown. The fits lead to the data shown in Tab. 9.4.

x_{OH}	Δz [nm]	D [nm^2/ns]	τ [ps]
1/4	0.18	0.19	65
1/8	0.22	0.55	50
0	0.24	1.66	36
1/4	0.10	0.06	75
1/8	0.10	0.20	50
0	0.10	0.85	27
bulk	0.10	2.65	5.0

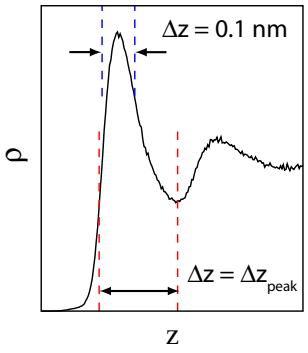

Table 9.4.: Diffusion constants obtained from fitting the ACF to $y = a_0 + a_1/\sqrt{t}$ in the region of the first water peak (upper part) and in a 0.1 nm region centered at the position of first water peak (lower part). The region of the first water peak is ranging from the position where the water density is for the first time equal to that of the first water density minimum up to the position of the first water density minimum. The two different slab regions are indicated in the figure on the right hand side. D is obtained from fitting the ACF to the functional form $C(t) = a_0 + a_1/\sqrt{t}$ in that time interval where the agreement with a power law is best. The time constant τ results from fitting the functions to $C(t) = a_0 \exp(-t/\tau) + a_1$ for $0 < t \leq 100$ ps. The ACFs in the first water peak together with the fits are shown in Fig. 9.5. Also, the results for bulk water are shown. For the determination of τ, the autocorrelation function is fitted to $C(t) = a_0 \exp(-t/\tau) + a_1$ in the interval $0 < t \leq 20$ ps.

by

$$p(z,z',t) = (4\pi Dt)^{-1/2}\left[\exp\left(-\frac{(z-z')^2}{4Dt}\right) + \exp\left(-\frac{(z+z')^2}{4Dt}\right)\right]. \tag{9.10}$$

The solution for two parallel walls with absorbing boundary conditions can be constructed from the infinite superposition of eigenfunctions of the diffusion equation [165]. Assuming a constant density ρ inside the layer, the autocorrelation function eq. (9.4) decays with the inverse square root of time for long times ($t \gg (\Delta z)^2/Dt$). In contrast to the bulk solution in eq. (9.8), the prefactor is larger by a factor of two.

$$\begin{aligned} C(t) &= \mathcal{N}^{-1}\int_{z_0}^{z_0+\Delta z} dz \int_{z_0}^{z_0+\Delta z} dz'\; p(z,z',t)\rho_0(z) \\ &= \frac{1}{\sqrt{4\pi Dt(\Delta z)^2}}\int_{z_0}^{z_0+\Delta z} dz \int_{z_0}^{z_0+\Delta z} dz'\; \left[2 + O\left(\frac{(\Delta z)^2}{4Dt}\right)\right] \\ &\approx \frac{\Delta z}{\sqrt{\pi Dt}} \end{aligned} \tag{9.11}$$

Fitting of the ACFs obtained from the simulation data to a function $y = a_0 + a_1 x^{-1/2}$ leads to the diffusion constant $D = (\Delta z)^2/(\pi a_1^2)$ for the diffusion perpendicular to the considered layer. The autocorrelation functions, shown in Fig. 9.5, are obtained from the simulation of one solid surface in contact with water in a $3.0 \times 3.0 \times 8.0$ nm box in the NP_zT ensemble. Two different regions of the water slab are considered for the estimation of the diffusion constant, depicted in Tab. 9.4. The first one extends over the entire first water peak in the density profile. By definition, it starts at the position where the water density is for the first time equal to water density at the first minimum and it ends at the position of the first water density minimum. The second corresponds to a 0.1 nm wide layer, centered at the maximum density of the first water peak. The diffusion constant decreases for the more hydrophilic surfaces, see Tab. 9.4. Compared to the bulk value, the diffusion constant is only moderately reduced at the hydrophobic surface, whereas it is reduced by a factor of more than ten at the most hydrophilic one in the peak region. For the smaller water slab in which the water molecules are on average closer to the surface, the difference between the hydrophilic and the hydrophobic surface is even more pronounced. This is due to the fact that the surface potential which is experienced by the water molecule decreases with increasing distance from the surface. However, care has to be taken with the interpretation of the obtained diffusion constant due to the crude assumptions. The neglect of the surface potential, of the position dependent mobility[1] and the assumption of a constant density in the peak region will certainly lead to changes in the calculation of the real diffusion constant. However, a simple solution of the diffusion equation without these assumptions is not possible any more.

Another property of interest is the timescale τ on which a water molecule stays in the first water layer. This timescale is estimated from the initial decay of the

[1] From hydrodynamic theory, the mobility of a single sphere approaching a no slip boundary is decreasing, which was shown in chapter 2.

autocorrelation functions in Fig. 9.5. For the hydrophilic surfaces, this decay constant is between 50 and 65 ps, thus roughly twice as long as for the hydrophobic surface ($\tau =$ 36 ps), see Tab. 9.4. This decay time is indeed sensitive on the surface hydrophilicity, in contrast to the results in Ref. [151], where the residence time is insensitive to the surface hydrophilicity. The longer residence time at the hydrophilic surface is due to the fact that the water molecules are more strongly attracted to the polar surfaces. Even for the hydrophobic surface, the residence time is much longer than for bulk water. In bulk water, this time constant for the same slab thickness is only 5 ns, see Tab. 9.4, thus comparable to the lifetime of a single hydrogen bond $\tau_{\mathrm{H}} \sim 1$ ps [19].

10. Summary and outlook

This work presents theoretical results on interfacial polymer and water dynamics. In the first chapter, the importance of polymer and water dynamics in science and in technological applications is discussed and a general overview of the main issues is provided. Coarse-grained and all-atomistic simulations as well as analytic non-equilibrium Fokker-Planck techniques are employed.

The first part of the thesis is concerned with non-equilibrium polymer dynamics. The effect of solvent molecules are implemented within a continuum hydrodynamic theory which is explained in chapter 2. Chapter 3 provides a general survey on polymer dynamics in unbounded shear flow and different polymer models are introduced. In Brownian Dynamic simulations, we find that after an initial stretching of the polymer with increasing shear strength, the polymer extension decreases at higher shear rates. This effect is caused by the configurational constraints arising from the constant contour length of the polymer and has not been observed in single molecule experiments.

Chapter 4 then analyzes the effect of a no-slip boundary on the the polymer dynamics in shear flow. Due to the orientation of a polymer in shear flow together with the hydrodynamic interactions at the interface, a repulsion of the polymer from the boundary is observed. We quantify this repulsion in terms of shear rate, polymer length and temperature. The analytic calculations are validated by the results of hydrodynamic simulations. Chapter 5 discusses the repulsion of polymers at interfaces in external, constant fields. Again, the coupling between thermal fluctuations and hydrodynamic interactions drives the polymer away from the interface. Hydrodynamic simulations confirm the predicted dependence of this lift force on parameters like polymer length, external field strength and distance from the wall. The electrical manipulation of end grafted DNA is discussed in chapter 6 of the first part. Effects, arising from the different bending stiffness of single and double stranded DNA are examined. Possible biosensing applications of this system are discussed by the adsorption of ligands at the free end of the DNA.

In contrast to the first part where the solvent molecules are incorporated in a coarse grained fashion, the second part analyzes the equilibrium and non-equilibrium structure of interfacial water on an atomistic level. Via Molecular Dynamics simulations, the equilibrium water structure at a hydrophobic diamond surface is studied in chapter 7. Contact angles are determined for different degrees of the surface hydrophobicity. In the subsequent chapter 8, these surfaces are used in non-equilibrium shear flow simulations to examine the hydrodynamic boundary condition. We find a quasi-universal relationship between the contact angle and the slip length. In shear flow simulations with dissolved gas, we only find mild effects of a surface adsorbed gas layer on the slip length. The last chapter of the second part extends the preceding

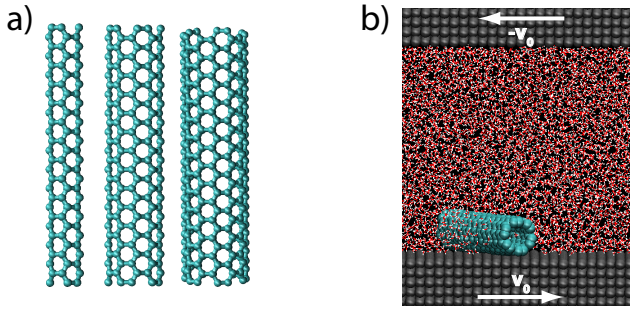

Figure 10.1.: In Fig. a), carbon nanotubes of 3.3 nm length with diameters ranging from 0.4 nm to 0.8 nm are depicted. Fig. b) shows a simulation setup to analyze the nanotube dynamics in shear flow. The nanotube is immersed in a water film between two surfaces. The two surfaces are then pulled in opposite directions which leads to a shear flow profile inside the water film, in the same way as presented in chapter 8. Preliminary simulation results suggest that the nanotubes are adsorbed at the interface.

studies of non-polar, hydrophobic surfaces to polar, hydrophilic surfaces. The shear viscosity in the interfacial water layer at the polar surfaces is moderately increased by a factor of four, compared to bulk water. The diffusion of single water molecules is found to be slower at the hydrophilic surfaces than at the hydrophobic interfaces. However, we do not observe an increase in viscosity of several orders of magnitude or a solid like water structure at hydrophilic surfaces.

A natural extension of the MD simulations would be to apply this technique to large objects in interfacial flow. Preliminary results on the adsorption of carbon nanotubes at hydrophobic interfaces indicate that the nanotubes are adsorbed on the surface, see Fig. 10.1. Using the setup described in chapter 8, the effect of shear flow on the adsorption and orientation dynamics of the carbon nanotube can be analyzed. First results suggest that the adsorbed tube rather glides than rolls on the surface in shear flow. The knowledge of the hydrodynamic boundary conditions at the liquid/solid interface and at the nanotube surface and of the effective surface potential obtained from these simulations will be crucial for the explanation of the dynamics.

However, the MD simulation technique is computationally very demanding and is therefore restricted to small systems with dimensions of a few tens of nanometer. Nevertheless, the results obtained in the all-atomistic simulations for the interfacial energies, slip lengths and depletion thickness can be fed into coarse-grained simulation models. Our approach thus constitutes an example of multi-scale modeling of complex matter at interfaces.

Parts of this thesis have been published in or submitted to peer-reviewed journals, or manuscripts for such contributions are in preparation. These contributions include:

- C. Sendner, Y. W. Kim, U. Rant, K. Arinaga, M. Tornow and R. R. Netz, Dynamics of end grafted DNA molecules and possible biosensor applications, *Phys. Status Solidi (a)* **2006**, *203 (14)*, 3476
- C. Sendner and R. R. Netz, Hydrodynamic lift of a moving nano-rod at a wall, *Europhys. Lett.* **2007**, *79*, 58004
- C. Sendner and R. R. Netz, Shear-induced repulsion of a semiflexible polymer from a wall, *Europhys. Lett.* **2008**, *81*, 54006
- F. Sedlmeier, J. Janecek, C. Sendner, L. Bocquet, R. R. Netz and D. Horinek, Water at polar and non-polar solid walls, *Biointerphases* **2008**, *3*, FC23
- D. M. Huang, C. Sendner, D. Horinek, R. R. Netz and L. Bocquet, Water slippage versus contact angle: a quasi-universal relationship, *Phys. Rev. Lett.*, in press **2008**
- C. Sendner and R. R. Netz, Polymer compression at high shear rates, *in preparation* **2008**
- C. Sendner and R. R. Netz, Shear flow simulations at hydrophobic and hydrophilic interfaces and the effect of dissolved gas, *in preparation* **2008**

A. Appendix

In this appendix, calculations and details of the computer simulations are shown. In section A.1, computational details of the coarse-grained polymer simulations are described which lead to a speedup in computer time. As a test of the polymer simulations, scaling relations from polymer theory are compared to the simulation results in section A.2. Section A.3 explains the details for the calculation of the tumbling frequency of polymers in shear flow. Lastly, section A.4 is concerned with the calculation of the contact angle in the MD simulations.

A.1. Updating the mobility matrix

The inclusion of hydrodynamic interactions in Brownian Dynamics simulations leads to increasing computational effort, especially for large systems, i.e. long polymers. The calculation of the mobility matrix for N particles requires $O(N^2)$ computational steps. To implement the fluctuation dissipation theorem, eq. (2.19), a Cholesky decomposition of the mobility matrix is performed which is a $O(N^3)$ process. Although the use of optimized LAPACK [46] routines leads to a considerable increase in computational speed, most of the computer time is spent on the evaluation of the mobility matrix and on its Cholesky decomposition. The hydrodynamic simulations are sped up considerably by updating the mobility matrix only every *nth* step. In Fig. A.1, the performance of the simulations on a AMD opteron CPU for different values of n is shown. The accuracy of this procedure is checked by analyzing the radius of gyration of a $N = 100$ polymer at $\dot{\tilde{\gamma}} = 1$, see Fig. A.2. Within error bars, the data are not affected by the update frequency, since the mobility matrix is a slowly varying function of the particle distance ($\propto 1/r$). Also, we use relatively small timesteps of $\tilde{\mu}_0 = 10^{-4}$. To account for sufficient accuracy at moderate computational cost, we choose $n = 5$ for $N \leq 100$, for longer polymers, the mobility matrix is updated every 20th step.

A.2. Equilibrium properties of polymers

In this section, simulation results of equilibrium properties for flexible polymers are compared to predictions of polymer theory. The polymer beads are connected by the potential given in eq. (3.28). The spring constant is stiff enough such that the bond length between neighboring beads can be considered as constant. In all simulations, excluded volume and hydrodynamic interactions are included.

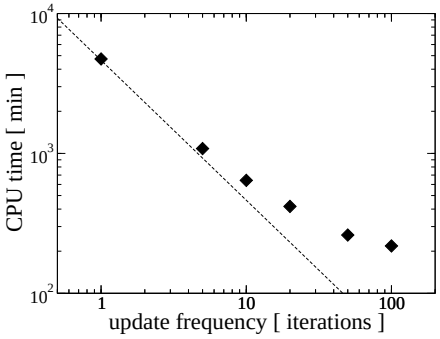

Figure A.1.: CPU time, dependent on the update frequency of the mobility matrix for a $N = 100$ polymer for $5 \cdot 10^7$ iteration steps. The broken line is a guide for the eye and denotes the scaling $\propto n^{-1}$.

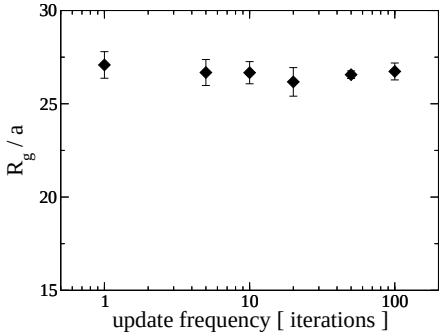

Figure A.2.: Radius of gyration of a $N = 100$ polymer at $\dot{\tilde{\gamma}} = 1$ for different update frequencies of the mobility matrix.

A.2.1. Radius of gyration

One important test of the simulation procedure is the scaling of the radius of gyration,

$$R_g^{\mu\nu} = \frac{1}{2N^2} \sum_{i,j=1}^{N} \langle (r_i - r_j)^\mu (r_i - r_j)^\nu \rangle \tag{A.1}$$

with polymer segment number N. For a self-avoiding, flexible polymer, the scaling of the radius of gyration is given by $R_g \equiv (R_g^{xx} + R_g^{yy} + R_g^{zz})^{1/2} \sim N^\nu$ with $\nu \approx 3/5$ [5]. Simulation results for polymers of different length $L_0 = 2Na$ with hydrodynamic interactions and excluded volume interactions are shown in Fig. A.3. The simulation data nicely obey the scaling given in eq. (A.1).

A.2.2. Relaxation time

The timescale of polymer dynamics in equilibrium is given by its longest relaxation time τ. Several methods exist for its estimation from the simulations. From the decay of the trajectory of the end to end vector of an initially fully stretched polymer, the relaxation time can be estimated with an exponential fit function. Nevertheless, the obtained relaxation times depend on the fit region. We use the decay of the autocorrelation function of the end to end vector or the radius of gyration of a polymer in equilibrium, to determine the relaxation times. Therefore, the autocorrelation function is fitted to an exponential function $C(t) = \exp(-t/\tau)$. Within the Zimm model in good solvent [5], i.e. with HI and excluded volume interactions, $\tau \propto N^{3\nu}$ with $\nu \approx 3/5$. Our results for the relaxation time follow nicely the predicted scaling, see Fig. A.4.

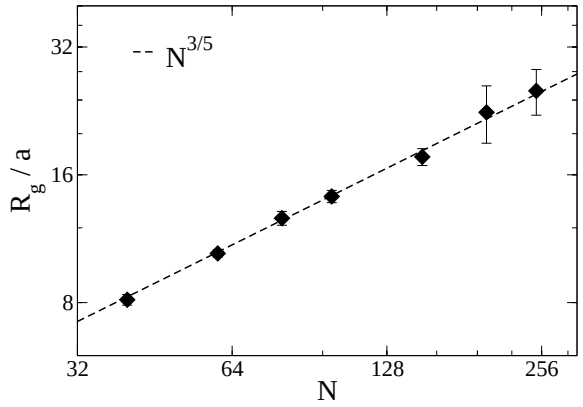

Figure A.3.: Equilibrium radius of gyration R_g for polymers of different length $L_0 = 2Na$. The broken line shows the predicted scaling $R_g \propto N^{3/5}$.

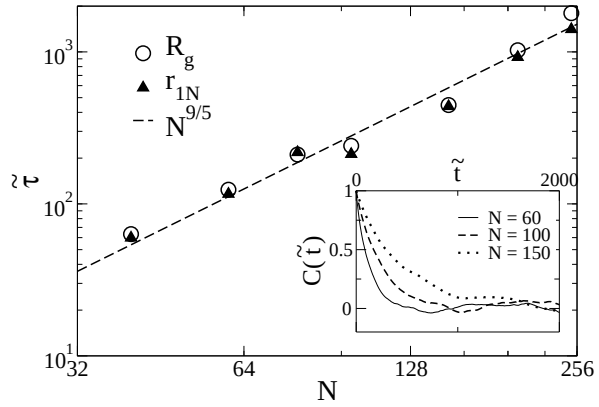

Figure A.4.: Relaxation times obtained from the decay of the autocorrelation function of the radius of gyration (○) and of the end to end vector (▲). The predicted scaling for polymer chains with hydrodynamic interactions and excluded volume interactions is shown by the broken line. The inset shows the autocorrelation functions of polymers with different length.

A.3. Tumbling frequency of polymers

Since the polymer shape in external shear flow is not constant, a well suited definition of the tumbling frequency is necessary. In our approach, the tumbling frequency $\boldsymbol{\omega}$ of a polymer with N beads is defined via the angular momentum

$$\mathbf{L} = \sum_{i=1}^{N} \mathbf{r}_i \times \mathbf{v}_i, \tag{A.2}$$

with the positions r_i and the velocities

$$\mathbf{v}_i(t) = \frac{\mathbf{r}_i(t+\Delta) - \mathbf{r}_i(t)}{\Delta}. \tag{A.3}$$

of the polymer beads. The angular momentum of the polymer is given by $\mathbf{L}(t) = \hat{\mathbf{I}}(t) \cdot \boldsymbol{\omega}(t)$ with the inertia tensor

$$I_{\alpha\beta} = \sum_{i=1}^{N} \delta_{\alpha\beta}\, \mathbf{r}_i^2 - r_i^\alpha r_i^\beta, \tag{A.4}$$

which depends on the polymer conformation. The tumbling frequency is obtained from the inverse of the inertia tensor,

$$\boldsymbol{\omega}(t) = \hat{\mathbf{I}}^{-1}(t) \cdot \mathbf{L}(t). \tag{A.5}$$

The average rotation frequency is then calculated by a time average over the simulation trajectory.

A.4. Contact angle from MD simulations

In this section, the calculation of the surface tension for the liquid/solid interface is described in more detail. We consider a solid slab with the surface normal in the $\hat{z}$-direction in contact with a liquid. From the simulations, the surface tension can be calculated either via eq. (7.3) or via the integration of the difference between the normal and tangential pressure

$$\gamma = \int_{-\infty}^{\infty} dz\, [p_n(z) - p_t(z)], \tag{A.6}$$

which are equivalent [166]. From mechanical stability, the normal component of the pressure tensor $p_n(z) \equiv p_{zz}(z)$ is constant, whereas the tangential component $p_t(z) \equiv (p_{xx} + p_{yy})/2$ depends strongly on position close to the interface due to the interaction between the solid and the liquid phase. Clearly, in bulk, the two components are equal. The pressure tensor consists of a kinetic term from the momentum of the molecules and of a potential term from the intermolecular forces, given in eq. (7.4),

$$V p_{\mu\nu} = \sum_i m_i v_i^\mu v_i^\nu + \Pi_{\mu\nu} \tag{A.7}$$

with particle index $i = 1..N$.

In the simulations for the surface tension of the solid/liquid interface, we switched off all interactions between the atoms of the solid. Then, these atoms must be held fixed artificially. This directly provides $\gamma_{\mathrm{ls}} - \gamma_{\mathrm{sv}}$ in eq. (7.3). For these simulations, the calculation of the surface tension by the pressure tensor does not give the correct result, since the kinetic energy is included in the pressure tensor, while the atoms of the solid slab are frozen in the simulation. Since the routine `g_energy` of the GROMACS [122] package uses the pressure tensor to calculate the surface tension, this leads to erroneous results if some atoms in the system are held fixed artificially. Therefore, from eqs. (7.2, 7.3), the contact angles are calculated by the components of the virial tensor of the liquid/solid (ls) system with the frozen surface atoms and by the virial tensor of the liquid/vapor (lv) system by

$$\cos\theta = -\frac{2\Pi_{zz}^{\mathrm{ls}} - \Pi_{xx}^{\mathrm{ls}} - \Pi_{yy}^{\mathrm{ls}}}{2\Pi_{zz}^{\mathrm{lv}} - \Pi_{xx}^{\mathrm{lv}} - \Pi_{yy}^{\mathrm{lv}}} \cdot \frac{A^{\mathrm{lv}}}{A^{\mathrm{ls}}} \tag{A.8}$$

with the surface areas A^{ls} and A^{lv} of the two systems.

Bibliography

[1] C. N. Likos, Phys. Rep. **348**, 267 (2001).

[2] A. Göthlich, S. Koltzenburg, and G. Schornick, Chem. Unserer Zeit **39**, 262 (2005).

[3] A. R. Bausch and K. Kroy, Nat. Phys. **2**, 231 (2006).

[4] P. G. de Gennes, *Scaling Concepts in Polymer Physics*, Cornell University Press, 1979.

[5] M. Doi and S. F. Edwards, *The theory of polymer dynamics*, Oxford University Press, New York, 1986.

[6] A. Y. Grosberg and A. R. Khokhlov, *Statistical Physics of Macromolecules*, American Institute of Physics, 1994.

[7] J. Wang, Nucleic Acids Res. **28**, 3011 (2000).

[8] T. M. Squires and S. R. Quake, Rev. Mod. Phys. **77**, 977 (2005).

[9] H. A. Stone, A. D. Stroock, and A. Ajdari, Annu. Rev. Fluid Mech **36**, 381 (2004).

[10] A. Link and J. Springer, Macromolecules **26**, 464 (1993).

[11] M. J. Menasveta and D. A. Hoagland, Macromolecules **24**, 3427 (1991).

[12] A. Keller and J. A. Odell, Colloid. Polym. Sci. **263**, 181 (1985).

[13] D. E. Smith, H. P. Babcock, and S. Chu, Science **283**, 1724 (1999).

[14] T. T. Perkins, D. E. Smith, and S. Chu, Science **276**, 2016 (1997).

[15] D. L. Ermak and J. A. McCammon, J. Chem. Phys. **69**, 1352 (1978).

[16] M. Fixman, J. Chem. Phys. **69**, 1527 (1978).

[17] J. Hur, E. S. G. Shaqfeh, and R. G. Larson, J. Rheol. **44**, 713 (2000).

[18] L. Feng et al., Angew. Chem. Int. Ed. **41**, 1221 (2002).

[19] P. Ball, Chem. Rev. **108**, 74 (2008).

[20] P. Atkins, *Physical Chemistry*, Oxford University Press, 1998.

[21] L. Feng et al., Adv. Mater. **14**, 1857 (2002).

[22] R. Wang et al., Nature **388**, 431 (1997).

[23] K. A. Dill, Protein Sci. **5**, 1166 (1999).

[24] E. Lauga, M. P. Brenner, and H. A. Stone, *Handbook of Experimental Fluid Dynamics*, volume Chapter 19, Springer, New York, 2007.

[25] B. L. de Groot and H. Grubmuller, Science **294**, 2353 (2001).

[26] R. M. Jendrejack, J. J. de Pablo, and M. D. Graham, J. Chem. Phys. **116**, 7752 (2002).

[27] U. Rant et al., PNAS **104**, 17364 (2007).

[28] U. Rant et al., Biophys. J. **90**, 3666 (2006).

[29] D. A. Doshi, E. B. Watkins, J. N. Israelachvili, and J. Majewski, PNAS **102**, 9458 (2005).

[30] P. Attard, Advances in Colloid and Interface Science **104**, 75 (2003).

[31] P. de Gennes, Langmuir **18**, 3413 (2002).

[32] S. Granick, Y. X. Zhu, and H. Lee, Nature Materials **2**, 221 (2003).

[33] M. Odelius, M. Bernasconi, and M. Parrinello, Phys. Rev. Lett. **78**, 2855 (1997).

[34] R. Zangi and A. E. Mark, Phys. Rev. Lett. **91** (2003).

[35] W. C. Cantrell and G. E. Ewing, J. Phys. Chem. B **105**, 5434 (2001).

[36] Y. Zhu and S. Granick, Phys. Rev. Lett. **87** (2001).

[37] T. D. Li, J. P. Gao, R. Szoszkiewicz, U. Landman, and E. Riedo, Phys. Rev. B **75**, 115415 (2007).

[38] J. Happel and H. Brenner, *Low Reynolds Number Hydrodynamics*, Noordhoff, Leyden, 1973.

[39] J. R. Blake, Proc. Camb. Phil. Soc. **70**, 303 (1971).

[40] S. Kim and S. J. Karrila, *Microhydrodynamics: Principles and Selected Applications*, Butterworth-Heinemann, Stoneham, MA, 1991.

[41] Y. W. Kim and R. R. Netz, J. Chem. Phys. **124**, 114709 (2006).

[42] J. Rotne and S. Prager, J. Chem. Phys. **50**, 4831 (1969).

[43] R. Zwanzig, Adv. Chem. Phys. **15**, 325 (1969).

[44] M. Lax, Rev. Mod. Phys. **38**, 541 (1966).

[45] L. Durlofsky, J. F. Brady, and G. Bossis, J. Fl. Mech. **180**, 21 (1987).

[46] E. Anderson et al., *LAPACK Users's Guide*, SIAM, Philadelphia, 3rd edition, 1999.

[47] W. H. Press, S. A. Teukolsky, and W. T. Vetterling, *Numerical Recipes in C*, Cambridge University Press, 2nd edition, 1992.

[48] R. G. Larson, J. Rheol. **49**, 1 (2005).

[49] P. G. de Gennes, J. Chem. Phys. **60**, 5030 (1974).

[50] M. Chertkov, I. Kolokolov, V. Lebedev, and K. Turitsyn, J. Fl. Mech. **531**, 251 (2005).

[51] A. Puliafito and K. Turitsyn, Physica D **211**, 9 (2005).

[52] A. Celani, A. Puliafito, and K. Turitsyn, Europhys. Lett. **70**, 464 (2005).

[53] M. Herrchen and H. C. Öttinger, J. Non-Newtonian Fluid Mech. **68**, 17 (1997).

[54] J. S. Lee, E. S. G. Shaqfeh, and S. J. Muller, Phys. Rev. E **75**, 040802 (2007).

[55] C. M. Schroeder, R. E. Teixeira, E. S. G. Shaqfeh, and S. Chu, Phys. Rev. Lett. **95**, 018301 (2005).

[56] P. S. Doyle, E. S. G. Shaqfeh, and A. P. Gast, J. Fl. Mech. **334**, 251 (1997).

[57] C. C. Hsieh and R. G. Larson, J. Rheol. **48**, 995 (2004).

[58] C. M. Schroeder, R. E. Teixeira, E. S. G. Shaqfeh, and S. Chu, Macromolecules **38**, 1967 (2005).

[59] D. E. Dunstan, E. K. Hill, and Y. L. Wei, Polymer **45**, 1261 (2004).

[60] D. E. Dunstan and Y. Wei, Eur. Phys. J. Appl. Phys. **38**, 93 (2007).

[61] D. Petera and M. Muthukumar, J. Chem. Phys. **111**, 7614 (1999).

[62] T. Liu, J. Chem. Phys. **90**, 5826 (1989).

[63] S. B. Smith, L. Finzi, and C. Bustamante, Science **258**, 1122 (1992).

[64] H. Clausen-Schaumann, M. Seitz, R. Krautbauer, and H. E. Gaub, Curr. Opin. Chem. Biol. **4**, 524 (2000).

[65] M. Rief, F. Oesterhelt, B. Heymann, and H. E. Gaub, Science **275**, 1295 (1997).

[66] W. Bruns and W. Carl, Macromolecules **26**, 557 (1993).

[67] S. R. Keller and R. Skalak, J. Fl. Mech **120**, 27 (1982).

[68] S. Sukumaran and U. Seifert, Phys. Rev. E **64**, 011916 (2001).

[69] S. Gerashchenko and V. Steinberg, Phys. Rev. Lett. **96**, 038304 (2006).

[70] R. E. Teixeira, H. P. Babcock, E. S. G. Shaqfeh, and S. Chu, Macromolecules **38**, 581 (2005).

[71] P. J. Hagerman, Annu. Rev. Biophys. Bio. **17**, 265 (1988).

[72] G. P. Krishnan and D. T. Leighton, Phys. Fl. **7**, 2538 (1995).

[73] D. Saintillan, E. S. G. Shaqfeh, and E. Darve, J. Fl. Mech. **557**, 297 (2006).

[74] Y. L. Chen, M. D. Graham, J. J. de Pablo, K. Jo, and D. C. Schwartz, Macromolecules **38**, 6680 (2005).

[75] O. B. Usta, J. E. Butler, and A. J. C. Ladd, Phys. Rev. Lett. **98**, 098301 (2007).

[76] H. B. Ma and M. D. Graham, Phys. Fl. **17**, 083103 (2005).

[77] P. Olla, J. Phys. II **7**, 1533 (1997).

[78] B. Lorz, R. Simson, J. Nardi, and E. Sackmann, Europhys. Lett. **51**, 468 (2000).

[79] J. R. Smart and D. T. Leighton, Phys. Fl. A **3**, 21 (1991).

[80] E. J. Hinch and L. G. Leal, J. Fl. Mech. **52**, 683 (1972).

[81] R. G. Winkler, Phys. Rev. Lett. **97**, 128301 (2006).

[82] H. Risken, *The Fokker-Planck Equation, Methods of Solution and Applications*, Springer, New York, Berlin, Heidelberg, 1989.

[83] R. Lipowsky, R. and T. M. Nieuwenhuizen, J. Phys. A **21**, L89 (1988).

[84] R. R. Netz and D. Andelman, Phys. Rep. **380**, 1 (2003).

[85] N. Pernodet et al., Phys. Rev. Lett. **85**, 5651 (2000).

[86] L. E. Becker, G. H. McKinley, and H. A. Stone, J. Non-Newtonian Fluid Mech. **63**, 201 (1996).

[87] N. J. De Mestre and W. B. Russel, J. Eng. Math **9**, 81 (1975).

[88] W. B. Russel, E. J. Hinch, L. G. Leal, and G. Tieffenbruck, J. Fl. Mech. **83**, 273 (1977).

[89] T. N. Swaminathan, K. Mukundakrishnan, and H. H. Hu, J. Fl. Mech. **551**, 357 (2006).

[90] A. Serr, *Dynamics of single polymers at surfaces*, PhD thesis, TU München, 2007.

[91] X. Schlagberger and R. R. Netz, Europhys. Lett. **70**, 129 (2005).

[92] T. Hugel et al., Macromolecules **34**, 1039 (2001).

[93] C. Friedsam, H. E. Gaub, and R. R. Netz, Europhys. Lett. **72**, 844 (2005).

[94] M. J. Heller, Annu. Rev. Biomed. Eng. **4**, 129 (2002).

[95] T. G. Drummond, M. G. Hill, and J. K. Barton, Nat. Biotechnol. **21**, 1192 (2003).

[96] M. J. Tarlov and A. B. Steel, *Biomolecular Films*, volume 111, Marcel Dekker Inc, New York, 2003.

[97] E. M. Boon, J. E. Salas, and J. K. Barton, Nat. Biotechnol. **20**, 282 (2002).

[98] J. Fritz et al., Science **288**, 316 (2000).

[99] L. Li, H. Hu, and R. G. Larson, Rheol. Acta **44**, 38 (2004).

[100] C. Gutsche, M. Salomo, Y. W. Kim, R. R. Netz, and F. Kremer, Microfluid. Nanofluid. **2**, 381 (2006).

[101] P. Cluzel et al., Science **271**, 792 (1996).

[102] J. L. Viovy, Rev. Mod. Phys. **72**, 813 (2000).

[103] D. Long, J. L. Viovy, and A. Ajdari, Phys. Rev. Lett. **76**, 3858 (1996).

[104] O. B. Bakajin et al., Phys. Rev. Lett. **80**, 2737 (1998).

[105] R. R. Netz and J. F. Joanny, Macromolecules **32**, 9013 (1999).

[106] A. Vainrub and B. M. Pettitt, Chem. Phys. Lett. **323**, 160 (2000).

[107] U. Rant et al., Nano Lett. **4**, 2441 (2004).

[108] K. Wong and B. M. Pettitt, Biopolymers **73**, 570 (2004).

[109] M. Manghi, X. Schlagberger, and R. R. Netz, Phys. Rev. Lett. **96**, 068101 (2006).

[110] Y. W. Kim and R. R. Netz, Phys. Rev. Lett. **96**, 158101 (2006).

[111] B. Tinland, A. Pluen, J. Sturm, and G. Weill, Macromolecules **30**, 5763 (1997).

[112] G. S. Manning, Ber. Bunsen Ges.-Phys. Chem. Chem. Phys. **100**, 909 (1996).

[113] A. Naji and R. R. Netz, Phys. Rev. Lett. **95**, 185703 (2005).

[114] R. R. Netz, Eur. Phys. J. E **3**, 131 (2000).

[115] C. Pozrikidis, *Boundary integral and singularity methods for linearized viscous flow*, Cambridge Texts in applied mathematics, Cambridge University Press, 1992.

[116] C. Oostenbrink, A. Villa, A. E. Mark, and W. F. Van Gunsteren, J. Comp. Chem **25**, 1656 (2004).

[117] T. Darden, D. York, and L. Pedersen, J. Chem. Phys. **98**, 10089 (1993).

[118] U. Essmann et al., J. Chem. Phys. **103**, 8577 (1995).

[119] H. J. C. Berendsen, J. R. Grigera, and T. P. Straatsma, J. Phys. Chem. **91**, 6269 (1987).

[120] H. J. C. Berendsen, J. P. M. Postma, W. F. van Gunsteren, A. DiNola, and J. R. Haak, J. Chem. Phys. **81**, 3684 (1984).

[121] B. Hess, H. Bekker, H. J. C. Berendsen, and J. G. E. M. Fraaije, J. Comp. Chem **18**, 1463 (1997).

[122] E. Lindahl, B. Hess, and D. van der Spoel, J. Mol. Modeling **7**, 306 (2001).

[123] W. R. P. Scott et al., J. Phys. Chem. A. **103**, 3596 (1999).

[124] F. Sedlmeier et al., Biointerphases **3**, FC23 (2008).

[125] J. Genzer and K. Efimenko, Science **290**, 2130 (2000).

[126] J. Rowlinson and B. Widom, *Molecular theory of capillarity*, Oxford University Press, Oxford, 1982.

[127] J. Janecek and R. R. Netz, Langmuir **23**, 8417 (2007).

[128] T. Werder, J. Walther, R. Jaffe, T. Halicioglu, and K. P., J. Phys. Chem. **107**, 1345 (2003).

[129] M. De Barros Bouchet et al., Tribol. Mater. Surf. Interfaces **1**, 28 (March 2007).

[130] M. Kano, Tribol. Int. **39**, 1682 (2006).

[131] L. Bocquet and J. L. Barrat, Soft Matter **3**, 685 (2007).

[132] L. Joly, C. Ybert, E. Trizac, and L. Bocquet, Phys. Rev. Lett. **93**, 257805 (2004).

[133] O. I. Vinogradova and G. E. Yakubov, Langmuir **19**, 1227 (2003).

[134] P. Joseph and P. Tabeling, Phys. Rev. E **71**, 035303 (2005).

[135] A. Maali, T. Cohen-Bouhacina, and H. Kellay, Appl. Phys. Lett. **92**, 053101 (2008).

[136] C. Cottin-Bizonne, B. Cross, A. Steinberger, and E. Charlaix, Phys. Rev. Lett. **94**, 056102 (2005).

[137] Y. Zhu and S. Granick, Phys. Rev. Lett. **87** (2001).

[138] D. C. Tretheway and C. D. Meinhart, Phys. Fl. **14**, L9 (2002).

[139] E. Lauga, M. P. Brenner, and H. A. Stone, arXiv:cond-mat/0501557v3 (2005).

[140] S. M. Dammer and D. Lohse, Phys. Rev. Lett. **96**, 206101 (2006).

[141] A. C. Simonsen, P. L. Hansen, and B. Klosgen, J. Colloid Interface Sci. **273**, 291 (2004).

[142] J. W. G. Tyrrell and P. Attard, Phys. Rev. Lett. **87** (2001).

[143] D. Schwendel et al., Langmuir **19**, 2284 (2003).

[144] M. Switkes and J. W. Ruberti, Appl. Phys. Lett. **84**, 4759 (2004).

[145] M. Holmberg, A. Kuhle, J. Garnas, K. A. Morch, and A. Boisen, Langmuir **19**, 10510 (2003).

[146] D. M. Huang, C. Sendner, D. Horinek, R. R. Netz, and L. Bocquet, Water slippage versus contact angle: a quasi-universal relationship, in press Phys. Rev. Lett., 2008.

[147] L. Bocquet and J.-L. Barrat, Phys. Rev. E **49**, 3079 (1994).

[148] J. L. Barrat and L. Bocquet, Faraday Discuss. **112**, 119 (1999).

[149] D. Bratko and A. Luzar, Langmuir **24**, 1247 (2008).

[150] E. Wilhelm, R. Battino, and R. J. Wilcock, Chem. Rev. **77**, 219 (1977).

[151] S. H. Lee and P. J. Rossky, J. Chem. Phys. **100**, 3334 (1994).

[152] U. Raviv and J. Klein, Science **297**, 1540 (2002).

[153] U. Raviv, P. Laurat, and J. Klein, Nature **413**, 51 (2001).

[154] Y. Leng and P. T. Cummings, Phys. Rev. Lett. **94**, 026101 (2005).

[155] H. Sakuma, K. Otsuki, and K. Kurihara, Phys. Rev. Lett. **96**, 046104 (2006).

[156] Y. Leng and P. T. Cummings, J. Chem. Phys. **124**, 074711 (2006).

[157] A. Pertsin and M. Grunze, Langmuir **24**, 135 (2008).

[158] A. Pertsin and M. Grunze, Langmuir **24**, 4750 (2008).

[159] Y. Leng and P. T. Cummings, J. Chem. Phys. **125**, 104701 (2006).

[160] B. Hess, J. Chem. Phys. **116**, 209 (2002).

[161] R. C. Weast, *CRC Handbook of Chemistry and Physics*, CRC Press, Boca Raton, 1986.

[162] P. Mark and L. Nilsson, J. Phys. Chem. **105**, 9954 (2001).

[163] R. Mills, J. Phys. Chem. **77**, 685 (1973).

[164] W. S. Price, H. Ide, and Y. Arata, J. Phys. Chem. A **103**, 448 (1999).

[165] P. Liu, E. Harder, and B. J. Berne, J. Phys. Chem. B **108**, 6595 (2004).

[166] V. P. Sokhan and D. J. Tildesley, Mol. Phys. **92**, 625 (1997).